APPLICATIONS AND ANALYSIS STRATEGIES OF MAGNETOENCEPHALOGRAPHY IMAGING

by

Teresa Cheung

BSc., Simon Fraser University, 2007

THESIS SUBMITTED IN PARTIAL FULFILLMENT

OF THE REQUIREMENTS FOR THE DEGREE OF

DOCTOR OF PHILOSOPHY

IN THE

DEPARTMENT OF PHYSICS

FACULTY OF SCIENCE

SIMON FRASER UNIVERSITY

Spring 2012

APPROVAL

Name:	Teresa Cheung
Degree:	Doctor of Philosophy
Title of Thesis:	Applications and Analysis Strategies of Magnetoencephalography Imaging
Examining Committee:	Dr. Paul Haljan, Associate Professor (Chair)

Dr. Karen Kavanagh, Senior Supervisor
Professor

Dr. Ash Parameswaran, Supervisor
Professor, School of Engineering

Dr. Urs Ribary, Supervisor
Professor, Department of Psychology

Dr. Faisal Beg, Internal Examiner
Associate Professor, School of Engineering

Dr. Bernhard Ross, External Examiner
Associate Professor, Department of Medical Biophysics
University of Toronto

Date Approved: April 16, 2012

Abstract

Magnetoencephalography (MEG) is a method used to measure temporal changes in magnetic fields with a sensitivity range of femto-Tesla to nano-Tesla. It is well suited for measuring the very small magnetic fields generated by neuronal brain activity as well as any small varying magnetic fields. MEG is a versatile tool with untapped potential. This thesis explores three aspects of MEG: instrumentation, application, and new directions. Magnetic source phantoms were developed as ground truths to help with instrument standardization as well as model testing. A portable magnetic dipole phantom with a constant current generator was developed that can be independently driven without reliance on system specific hardware. Extending the phantom design to a multi-dipole model, a potential ground truth for MEG source imaging was developed.

Inverse analysis of MEG data for dipole and beamformer strategies were studied and applied specifically to the properties and neural generators for facial processing. Event-related activity between the perception of face and non-face object stimuli appears as an increase in amplitude for the face condition peaking around 170 ms over the posterior regions of MEG sensor recordings (M170). The anatomic origins of this face-selective 170 ms peak remains unresolved. A new model for the M170 neural generators was developed through the analysis of four different MEG studies. The M170 response was linked to simultaneous activity in the fusiform face area, occipital face area and superior temporal sulcus rather than any one individual location.

Finally, a novel technique was developed to extend the usage of MEG for magnetic nanoparticle imaging. There is potential to utilize the magnetic properties of these particles for internal imaging of living organisms using MEG. Stationary samples of magnetic nanoparticles in liquid suspensions were measured within the MEG helmet. The magnetic field of the particles appeared as a distinct increase in baseline noise in the frequency do-

main - highest in the low frequencies and decaying to below the noise floor above 500 Hz. A method using beamformers to localize these particles using this rise in frequency provided a robust technique for the potential localization of magnetic nanoparticles in vivo.

For Katharine and Sixtus

In loving memory of my grandmother

Fung, Po Kuen (1912 - 2012)

Acknowledgements

With gratitude I thank my supervisors, Karen Kavanagh, Ash Parameswaran and Urs Ribary for their inspiration and leadership.

Thank you also to the chair, Paul Haljan. Special thank you to internal examiner Faisal Beg and external examiner Bernhard Ross for their participation. I am grateful to Alexander Moiseev with proofreading. I would like to also thank The Down Syndrome Research Foundation, Michael Smith Foundation for Health Research, NSERC and the BC Leading Edge Endowment Chair's Rix Student Award for their financial support. Thanks also to Mario Liotti, Jason Barton, Naznin Vrji-Babul, Jiri Vrba, Al Fife, Doug Cheyne, Larry Roberts, and Ruth Grunau for their mentorship. Thank you also to Dawn McKenna, Julie Unterman, Arif Babul, Joseph Wong, Jeff Lui, Brent Taylor, the employees at MISL, Jennifer Barry and Sarmita Majumder. Thank you Sylvain Baillet, Montreal Neurological Institute, Paul Furlong, Aston University and Caroline Witton, Aston University for their help with the phantom collections and MEG lab access.

In memory of Max Burbank, President and Co-founder of CTF Systems.

Contents

List of Tables

List of Figures

Chapter 1

Introduction

Over the last two decades, multi-channel SQUID based biomagnetic detectors have been developed and adopted in many research and clinical settings. The measurement of biomagnetic fields by these devices is called magnetoencephalography and commonly known by the abbreviation MEG.

A complex set of hardware and software components goes into measuring MEG data. Each MEG manufacturer has developed their own set of hardware and software to acquire MEG data. Each device, even from the same manufacturer is essentially handmade and may undergo site-specific customization. How do we know that each machine is measuring the same field and that we can reliably compare results of timing, amplitude and frequency from data collections at different MEG sites? As MEG evolves from a research tool of scientific interest to a tool of clinical relevance, the need to standardize and report cross-site comparability becomes an important question to answer.

Even if we assumed that each device is measuring and reporting the same field, the source imaging that occurs to convert the surface magnetic field data to the 3-D images within the human head is a result of complex inversion algorithms, each with strengths and weaknesses. How do we reliably know if the inversion, particularly with a new technique is yielding reasonable results? Simulations are utilized as a first pass to test new algorithms but often these simulations utilizes the same assumptions in the forward model, as does the inverse algorithm so it does not fully test the algorithm. Real brain data can also be used but we are limited in our ability to ensure same subject reproducibility as many conditions may change a subject's response even under the most basic evoked protocols.

Both cases allude to the need for a ground truth for MEG. The former, that of cross-site comparability, can be well answered by the use of a single dipole phantom. The latter, however is more complex and I argue that a multi-dipole phantom could be a potential ground truth for certain aspects of the inverse problem. A phantom is a hardware device that simulates an aspect of the brain that is used to confirm machine function. In MRI, phantoms are used to confirm spatial accuracy of an image. In MEG, phantoms are used to confirm model accuracy of field patterns. MEG phantoms contain sources that simulate neuronal magnetic field activity. Chapter 3 addresses these needs with the construction of two phantoms. A single dipole phantom is developed as a ground truth for cross-site comparability. A multi-dipole phantom is developed as a potential ground truth for source modelling.

There are many MEG measurements of human brain activity with unresolved research questions. The neural generators for face processing are one such problem. On the sensor level, a peak occurs over the posterior channels at approximately 170 ms. This peak has larger amplitude for faces compared to objects and is commonly known as the M170. While the sensor space activity is bilateral but usually larger on the right hemisphere compared to left, descriptions of the neural generators are mixed depending on the technique used to create the inverse model of the data. The M170 is commonly measured in many labs but proper localization using MEG has been elusive because the right and left neural generators for the M170 appear to be highly correlated. Thus beamforming techniques fail to capture the whole picture. In addition, more than one bilateral source appears to be simultaneously active and therefore the standard two-dipole model for the M170 fails to describe the neural generators at 170 ms fully.

Chapter 4 examines the role of the M170 in the processing of face versus non-face object stimuli. Through a series of studies, the M170 is examined in sensor and source space for children, children with Down syndrome, adults and adults with brain damage in one of the core face processing areas. The studies illustrate an evolution of M170 analysis first looking mainly at the fusiform facial area (FFA) only and then extending the model to include the occipital face area (OFA) and superior temporal sulcus (STS).

First dynamic movies of faces are compared to static faces in a small study involving children. Next the latency of the M170 in children with Down syndrome is compared to typically developing children. An important contribution on how faces are processed on

the neural level is described in the final section in this chapter where a dipole analysis is described for a multiple source model of the M170. The source localization results suggest the M170 originates at multiple source locations. For the first time equivalent dipole localization is performed with a best fit solution that includes all three of the core facial processing network areas found in fMRI studies, namely the FFA, the OFA and the STS.

The use of contrast agents in other imaging modalities is not uncommon. However, this concept has only been investigated peripherally for MEG. Magnetic nanoparticles may be a candidate contrast agent for MEG. Magnetic nanoparticles are objects with nanometer dimensions with an inorganic magnetic core. In tissue, the magnetic field of these particles may be detectable. Using MEG devices to measure these particles in tissue may serve as a new application for internal medical imaging. These particles have been used in vivo as magnetic tracers in the blood stream ([13],[60]). A study investigating the effects of a ferrofluid injected in rats was performed by Saligram, Moran and Tepley in 1996 [69]. They observed changes in the magnetic cardiogram of the rats but not in the blood stream. More recent work has focused on pre-magnetization [68] of the particles in tissue as well as the use of rigid movements to cause a detectable signal [41].

The work in chapter 5 focuses on the idea that the magnetic particles may be better detected in the frequency domain rather than time and that by using this fact, methods can be developed that can help successfully introduce this technique for potential in vivo applications. The first section in the chapter introduces the concepts of frequency detection and describes some of the properties of the ferrofluid. The second section extends the findings and continues to characterize the frequency profile of the nanoparticles. The final section describes a technique using beamformers to localize the particles as well as the use of a driving frequency, within the tolerance range of MEG, to enhance the signals above brain noise.

This thesis describes the development of phantoms for both device and model testing, examined analysis strategies to localize the sources of the face selective M170 and explored a potential new application using magnetic nanoparticles. Through the study of magnetic fields from human, artificial and natural sources, it is hoped that I have gained a better understanding of MEG measurements and the subtle problems in MEG source modelling.

1.1 Summary of Thesis Contributions

Chapter 2: Background on MEG
This chapter briefly introduces the reader to neural basis of MEG, the forward problem and inverse problem. It serves as background material relevant to the proceeding chapters.

Chapter 3: Phantom
This chapter describes the construction of two phantoms: a device ground truth containing a single dipole source and a prototype hardware brain phantom. My contribution in this chapter to this thesis was in the overall design, testing protocols and studies involving the collection of data from these phantoms. The electronics and firmware was designed and constructed by Jeff Liu [50]. A dry phantom was constructed to facilitate ease of use. The prototype utilized magnetic dipoles. The ultimate goal of the phantom was to provide a ground truth for MEG. I developed the testing protocol for the single dipole phantom and collected or organized the collection of the data at the different MEG laboratories. I analyzed the data collected. I developed the testing protocol for the multiple dipole phantom and analyzed the data collected.

The first section of chapter 3 has been submitted to Biomag 2012 (authors: Cheung, T, Lui, J, Furlong, P, Wilton, C, Braeutigam, S, Parameswaran) [11].

The second section of chapter 3 is a reprint of material as it appears in Kakigi R, Yokosawa K, Kuriki S, (Eds.), Biomagnetism: Interdisiplinary Research and Exploration (pp. 89-91). Hokkaido: Hokkaido University Press, 2008 (authors: Cheung T, Wong J, Parameswaran A, Babul A, Beg F, Kavanagh KL, Jirasek A, and Ribary U).

Chapter 4: Face-selectivity of the M170
In this chapter, inverse methods and strategies were applied to the problem of the M170 response to face versus object stimuli. My contribution in this thesis involved the analysis of data from 4 studies to characterize the M170 in children and adults as well as children with Down syndrome. In particular, I created a 6-dipole model (3 symmetric pairs) that seems to fit well at the M170. This model suggests that the M170 co-activates three areas

of the face network consistent with fMRI findings.

The first section of chapter 4 was an abstract and poster at Society for Neuroscience Conference San Diego (2007) (authors: Cheung, T, Virji-Babul, N).

The second section of chapter 4 is a reprint of material as it appears in Down Syndrome Quarterly, 10:18-21 (2008) (authors: Cheung, T., Virji-Babul, N) [10].

The third section of chapter 4 will be submitted for publication to Human Brain Mapping. (Cheung, T, Barton, J, Iarocci, G, Tanaka, J, Liotti, M.).

Some of the material in third section was published in Journal of Vision, 10, 7 (2010) (authors: Oruc, I, Cheung, T, Dalrymple, K, Fox, C, Iaria, G, Handy, T, and Barton, J) [63]. I worked on the MEG portion of the publication.

Chapter 5: Magnetic Particles for imaging
This chapter describes an original application of MEG for magnetic nano particle imaging. My contribution in this chapter to this thesis was the development of an imaging method utilizing these nanoparticles in the frequency domain for magnetic nanoparticle detection. The particles could be localized through vector beamforming techniques in frequency. By introducing an oscillating magnetic field small enough to be tolerated by the MEG SQUIDs, the ferromagnetic particles' fields were enhanced providing a potential narrow band technique for localization.

The first section of chapter 5 is a reprint of material as it appears in Human Brain Mapping 2009 Proceedings (authors: Cheung, T, Kavanagh, K, Moiseev, A., and Majumder, S.) [7].

The second section of chapter 5 is a reprint of material as it appears in Supek, S, Susac, A (Eds.) 17th International Conference on Biomagnetism Advances in Biomagnetism (2010) (authors: Cheung, T, Kavanagh, K, and Ribary, U) [8].

The third section of chapter 5 will be submitted for publication (authors: Cheung, T, Ka-

vanagh, K).

Chapter 6: Conclusions
Concluding remarks are listed in this chapter that summarizes the overall theme of the thesis.

Chapter 2

Background on MEG

2.1 Neural Basis of MEG

2.1.1 The Electromagnetic Brain

The neuronal electrophysiological activity in a functioning brain is manifested by ionic current flow that is strongest in the most active regions of the brain. These intracellular currents give rise to magnetic fields that extend beyond the scalp where they can be measured. The branch of science that is concerned with the measurement and interpretation of the brain's magnetic fields is called Magnetoencephalography (MEG).

Consider the neuron from an electromagnetic point of view. A neuron is a nerve cell consisting of dendrites (signal transmitter), soma (signal receiver), and axon (signal processor) [27]. A synapse is the gap between the axon of one neuron and the dendrites of the next. This junction can either be a direct electrical connection or more commonly a chemical connection in which the connecting axon releases neuro-transmitters that change the neuronal membrane permeability to Na+ and K+ ions (sodium-potassium pump) which causes a change in potential at the dendrites. The change in potential is known as post-synaptic potentials (PSPs). They have rise times of about 10 ms with peak amplitudes of about 10 mV. This signal from the dendrites is sent to the soma. If the potential reaches a certain threshold, an action potential (AP) is generated along the axon and passed to the next neuron. Action potentials have signals that are larger (100 mV) but shorter duration (1 ms) than PSPs. The summation flow of current caused by the post-synaptic potential

and the action potential from an assembly of neurons (thousands) over a cortical patch of a few mm give rise to the source currents known as impressed or intracellular currents (Figure 2.1). These source currents happen within an ionic conducting media consisting of the brain, the cerebral spinal fluid, the skull and the skin. The source currents are mostly responsible for MEG signals, while the return currents that flow through the conducting media are responsible for the electroencephalography potentials (EEG) detected at the scalp surface. These return currents are known as volume or extracellular currents. Volume currents also produce magnetic fields particularly when measuring in a non-radial direction and must be accounted for when modelling the impressed currents [1].

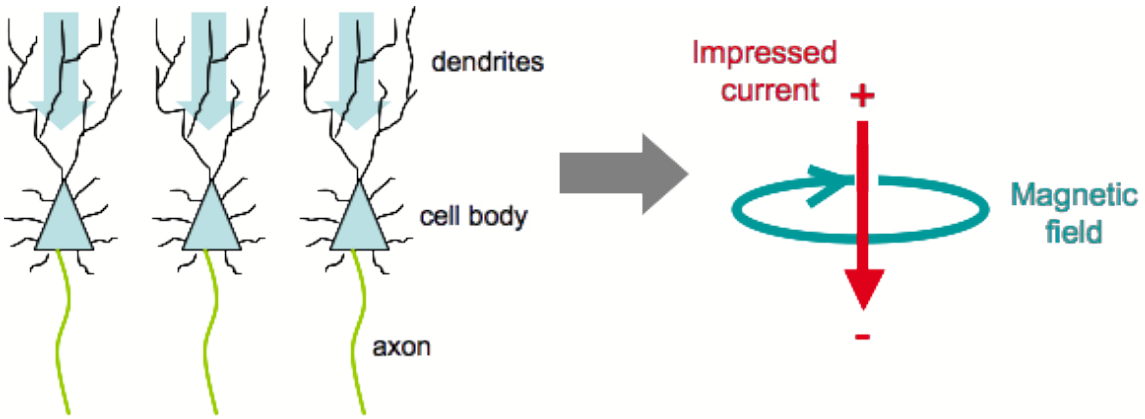

Figure 2.1: Impressed Current from an assembly of aligned neurons (thousands) can be modelled with a current dipole (impressed current). The magnetic field curls around the current flow according to the right hand rule.

The neuron comes in different geometries of dendrites. The vector summation of the dendritic currents produces the dendritic signals observed outside the cell body. Open field, pyramidal cells have asymmetric dendrites and give the largest dendritic signals. Closed field stellate cells have symmetric dendrites. Dendrite signals in stellate cells tend to cancel, reducing the dendritic currents observed outside the cell body.

MEG is mainly sensitive to the PSP activity of pyramidal cells, which are aligned perpendicular to the cortical surface ([51], [62]). The slower rise time of PSP signals are more forgiving to jitter and more likely to survive the summation process needed for a detectable signal to be generated. On the other hand, APs, though larger in amplitude, are so short in duration that jitter across neuronal assemblies will typically reduce their effects. However,

there is evidence ([52], [58]) that some high frequency (150 Hz-1000 Hz) MEG activity may be the result of action potential signals from stellate cells.

To model the magnetic fields from neuronal currents, a model for the source current as well as the conducting media must be included. The source current, in it's simplest form is often modelled with an equivalent current dipole. This dipole represents the summation activity of a small region of cortex. Larger cortical patches are modelled with a collection of current dipoles. The simplest conducting media model is a single sphere with concentric uniform conductivity. The conductivity is cancelled in the magnetic field equations, which allows this model to be quite robust because it does not require any estimation of the conductivities of the head.

2.1.2 Instrumentation

The brain's magnetic fields are extremely small, comparable to a magnetic field of a passenger car at a distance of about 1 km ([53]). Figure 2.2 illustrates the scales of magnetic fields and some of the instruments used to detect them. On the scale of brain signals, which are of the order of femto-Tesla to pico-Tesla, instruments sufficiently sensitive to measure such fields are SQUIDs (superconducting quantum interference devices) and atomic magnetometers.

At the present time, the only detectors that can rapidly measure the brain's magnetic fields with sufficient resolution are SQUID (superconducting quantum interference device) based magnetic field detectors operating at 4 Kelvin - the boiling point of liquid helium (low critical temperature (Tc) SQUIDs). Low Tc SQUIDs also can be designed to have a very flat frequency profile down to the low frequencies. 1/f noise can be restricted to below 0.5 to 0.1 Hz. Although detection of magnetic fields can also be achieved using atomic magnetometers, which utilize "Larmor spin precession of optically pumped atoms", they lack the sensitivity of SQUID magnetometers especially for small volume detection. However, the recent introduction of a "new spin-exchange relaxation-free atomic magnetometer" may finally challenge the SQUID's dominance in low field magnetometry ([73], [45]). These atomic magnetometers have sensitivity at the atto-Tesla level and recent advances suggest the poor low frequency 1/f response has been greatly improved. Additionally, room temperature atomic magnetometers have been achieved removing the need to cool the devices

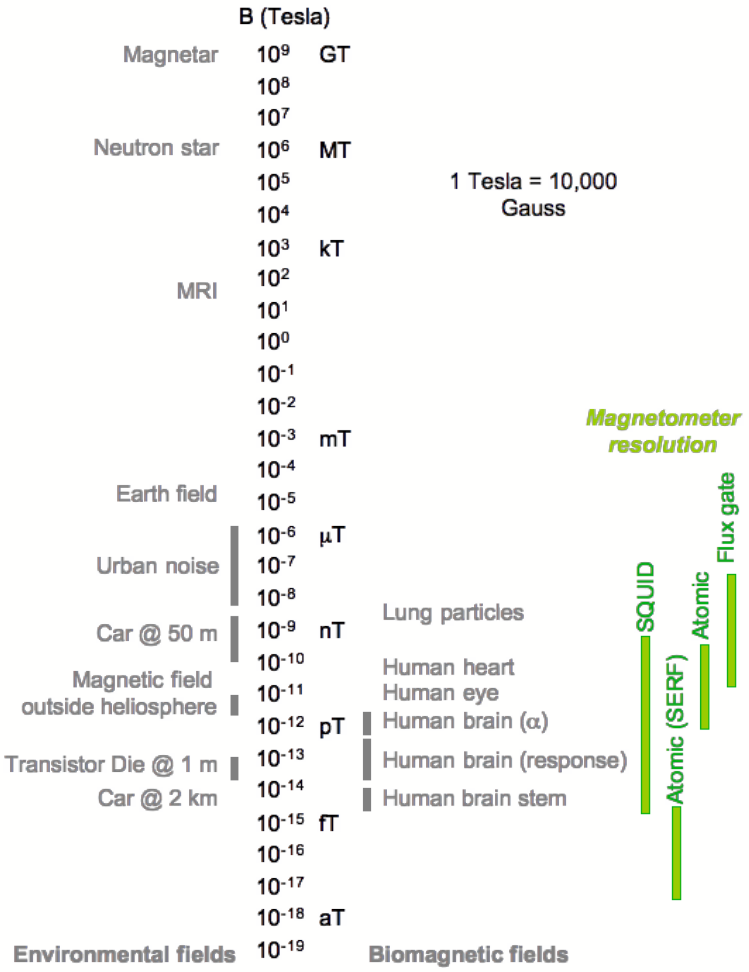

Figure 2.2: Sources of magnetic fields and magnetometer sensitivities. The human brain response is between 10^{-14} to 10^{-13} Tesla. In this range, only SQUID and Atomic magnetometers have sufficient sensitivity to detect these signals. (Magnetic field values were obtained from: [83] [92])

to a temperature comfortable for biological measurements [5]. Atomic magnetometers may indeed supplant SQUID magnetometers as the choice for MEG detection within the next decade [77].

For the last 20 years however, the only commercially viable technology for low field measurements have been SQUID sensors ([31], [86]). The first MEG system using a shielded room was operated at the Francis Bitter Magnetic Laboratory at MIT. It was under

the direction of group leader David Cohen, a pioneer in the field of MEG. Dr. Cohen, who is considered the inventor of the MEG system, first measured the magnetoencephalogram in 1968 ([14], [15]). One of the first whole head MEG systems was developed by CTF Systems in the late 1980's and early 1990's in Port Coquitlam, British Columbia, a company which can trace its beginnings to the Physics Department at Simon Fraser University. The first whole head system sold by CTF was shipped in 1992 [87]. Figure 2.3 shows a 151 channel whole head CTF MEG system ([85]).

MEG measures the distribution of magnetic field outside the scalp surface. However, it is often required to invert the magnetic field measurements and provide information about the current distribution within the brain. Methods used in MEG practice include current dipoles, minimum norm, beamformers, principal and independent component analysis (PCA and ICA) and Bayesian methods. MEG is finding its way into clinical applications in the areas of presurgical mapping, epilepsy, and closed head injury, and is employed in numerous research investigations, including pathological functional deficits, neuropharmacology, and a growing list of applications in neurosciences and psychiatry. Research using MEG has been growing at a steady pace since the 1990's.

The choice of reconstruction technique is dependent on the complexity of the observed field patterns and is vulnerable to model errors. The ill-posed nature of the problem means that there exists an infinite number of volume patterns that can produce the same surface pattern detected by the MEG [76]. A number of priors are required to pick a suitable solution and copious software simulations are used to verify the reliability of the reconstruction. Software simulations, however, are subject to issues of approximating the real world such as noise conditions and hardware construction errors [47]. Some of these simulation issues are addressed by the use of phantoms – a physical device that produces artificial "brain signals" that can be measured by the MEG. Hardware dipoles are used in place of neurons to generate the artificial brain signals.

Other brain imaging modalities

Brain imaging technologies can be generally classified into two broad categories: devices that image anatomical information and devices that image functional activity. The two categories are complementary and it is often when anatomical information is merged with functional that a useful picture of brain activity emerges. In practical applications, the

MEG results are usually combined with anatomical magnetic resonance images to give better information about the brain.

Figure 2.3: The 151 channel CTF MEG System installed at the Down Syndrome Research Foundation, Burnaby, BC.

X-rays, computed tomography (CT) scans, magnetic resonance imaging (MRI) and utrasonography provide anatomical information. The resolution and nature of the image depends on the individual technologies applied. Figure 2.4 illustrates the spatial and temporal resolutions of some common brain imaging equipment. Positron emission tomography (PET), single photon emission computerized tomography (SPECT), functional magnetic resonance imaging (fMRI), near-infrared spectroscopy (NIRS), EEG and MEG provide functional information. Functional imaging techniques provide the ability to assess how the brain behaves during normal cognitive, sensory, and motor performance as well as in

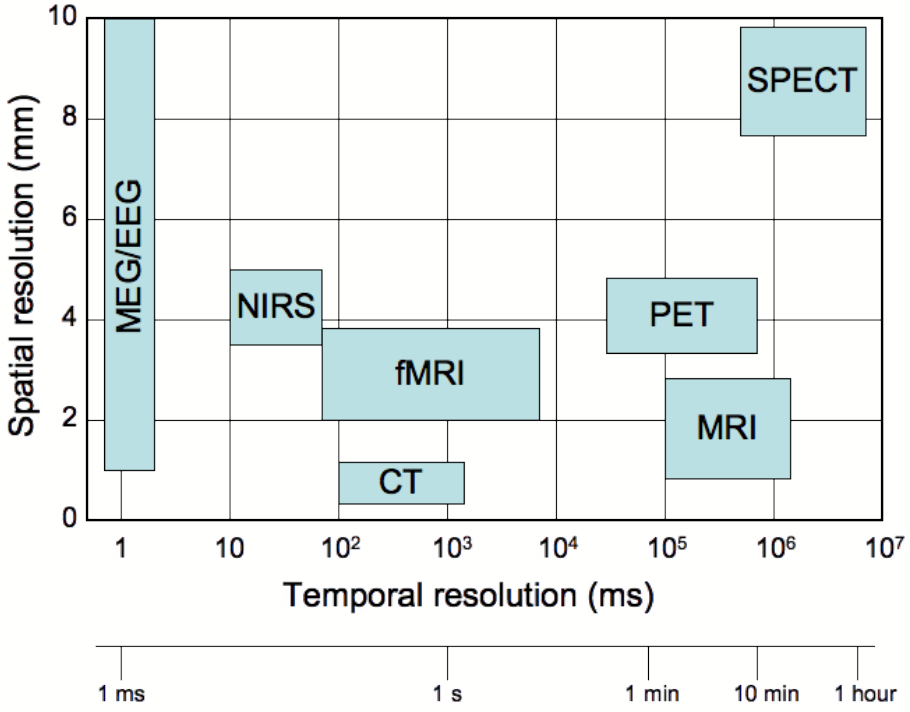

Figure 2.4: Spatial and temporal resolutions of different brain imaging devices.

various brain diseases. These techniques differ from one another in the particular aspect of neuronal activity that is chosen to represent the functional activity.

MEG and EEG provide a direct measure of neural activity because these technologies measure current flows and magnetic fields generated by neurons depolarizing in the brain - the source of brain function. Technologies such as PET, SPECT, fMRI and NIRS measure changes in blood flow or metabolism (perfusion dependent images) produced by neural activity and are more indirect measures of neural function. While methods based on blood flow are very useful and have good spatial resolution, a limitation is that changes in blood flow in response to stimulus or task occur slowly compared to the electrical and magnetic consequences of neural activity. MEG and EEG images change in the scale of milliseconds while the other technologies produce images that change in the range of 5 to 20 seconds because this is how long it takes blood flow changes to react to a change of electrical activity. The superior temporal resolution of MEG is important because much of the computational activity of the brain is conducted on a millisecond time scale, which cannot be imaged

by other techniques. MEG however is not very useful without additional co-registration with an image of the structural brain anatomy. This is typically achieved by combining an anatomical MRI with MEG through careful co-registration of the coordinate systems between the two devices.

The use of EEG to measure electrical activity has been available for many decades, long before the introduction of MEG. EEG alone is useful in assessing time signal patterns. However, even with the introduction of high-density EEG systems, EEG lacks MEG ability to localize sources of brain activity accurately. This is because tissue impedances in the skull and brain distort the electrical fields measured by EEG from electrodes placed on the scalp surface. The magnetic fields detected by MEG are not distorted by this factor and hence precise localization of tangential intracortical generators is possible. To obtain information on radial sources that are not seen by MEG sensors, simultaneous MEG and EEG recordings are collected. The head model that is necessary for imaging sources of brain activity with EEG is then corrected from simultaneous MEG and EEG measurement of tangential sources. This combined approach yields more accurate depiction of radial sources by EEG, enhancing the power of this technique with concurrent MEG measurement.

MEG is a favourable modality for brain function measurements when high temporal and spatial resolution images are required. It is also relatively safe technology, non-invasive and non-hazardous making MEG well suited for measuring children, patients and people with disabilities. Extra movement produced by these subjects can be tracked continuously and subsequently removed using head correction techniques [93].

Measuring MEG

The MEG is usually (but not always) installed within a magnetically shielded room. MEG sensors distributed evenly within a helmet shaped shell measures the magnetic field that extends beyond the scalp surface. These MEG sensors convert magnetic field to voltage, which is sent through amplifiers and digital to analog converters and recorded by a computerized data acquisition system. The recorded signals measured from the outside of the scalp surface are used to reconstruct a 3 dimensional volumetric image of the magnetic brain activity. The technique of modelling the magnetic field generators and describing it's spatial and temporal profile known collectively as the forward and inverse problems will be

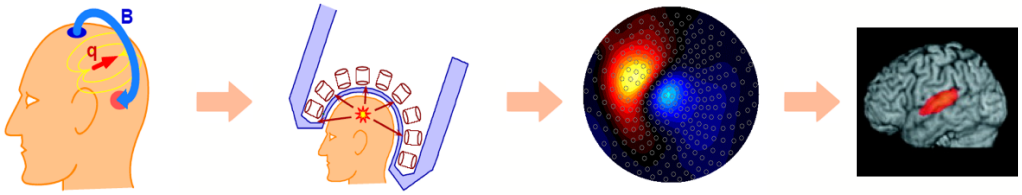

Figure 2.5: Magnetic field from a source (such as from the brain) is recorded using an array of MEG sensors distributed over a helmet shaped surface. The signal is collected over time according to the sampling frequency. At each time point, the instantaneous magnetic field response can be spatially mapped on a flattened 2D topography. The 2D surface data is converted to a 3D image of source activity through the process of inverse modelling or source modelling.

described in the next two chapters. Figure 2.5 illustrates this process.

SQUID biomagnetic measurements

The MEG sensors based on SQUIDs operate on quantum mechanical principles. The basic element of the SQUID sensor is a Josephson junction. Josephson junctions are employed to form either a DC or an RF SQUID. SQUID sensors alone are not well suited for the direct detection of magnetic fields, and often, they are coupled to the measured fields with the use of a flux transformer. Because the flux transformer circuits are also superconducting, their addition has the advantage of introducing a noiseless gain and providing a flat frequency response from DC (0 Hz) to the maximum system frequency (highest sample rate divided by 4 for most CTF and divided by 3 for Elekta) ([87], [90]).

The SQUIDs and flux transformers are enclosed in a helmet-shaped dewar filled with liquid helium at 4 K. The flux transformer consists of pickup coils, which are placed close to the helmet surface and exposed to the measured fields. The flux transformer is connected to the SQUID by leads and a coupling coil, which provides inductive coupling to the SQUID sensor. Depending on the objective of the measurement, the flux transformers can have a variety of configurations. The simplest flux transformers are magnetometers, which consist of a single loop of a superconducting wire such as niobium. They are sensitive to the field component normal to the loop. The flux transformers can also be 1st-order

gradiometers, which consist of two loops wound in opposing directions. The baseline is the distance between the gradiometer coils. The two pickup coils are placed along an axis that is perpendicular to the plane of it's sensing surface. For example, a baseline of 5 cm and coil diameter of 1.8 cm is used for CTF axial gradiometers. Such devices are sensitive to the magnetic field change over the gradiometer dimensions, and insensitive to uniform magnetic fields because the contributions from the two coils cancel. Connecting lower order gradiometers in an opposing sense can also create higher gradiometer flux transformers [91]. In addition, planar gradiometers may also be constructed by wiring two magnetometers along an axis that is parallel to the plane of the sensing surface. Elekta's planar gradiometers are rectangular with a baseline of 1.683 cm and dimensions 2.1x 0.948 cm [21].

The depth sensitivity differs between these coil geometries, as do their noise profiles. Magnetometers see the deepest but are the noisiest because they do not have a built in constant field subtraction. Axial gradiometers see the next deepest and can be considered as magnetometers with noise cancellation. Planar gradiometers have the shallowest depth of field but has the advantage of picking up neuronal currents directly below the pick up coils.

SQUID sensors in MEG systems are coupled to the room temperature read-out electronics. Most systems operate SQUIDs as null detectors within a feedback loop. Utilizing the flux periodicity of the SQUID transfer function can extend the dynamic range of the SQUID feedback loop. The loop is locked at a certain point of the SQUID transfer function and remains locked for the applied flux in the range of plus or minus 1 phi0. When this range is exceeded, the locking point is shifted by 1 phi0 along the transfer function. The flux transitions up and down the transfer function are counted and are combined with the signal from the digital integrator to increase dynamic range.

2.2 The Biomagnetic Forward Problem

2.2.1 The Physics of MEG

Magnetic fields from biological sources are generated from electric currents in a volume of conducting tissue. The forward problem describes these magnetic fields which are dictated

by the sources and conducting media. Biological magnetic fields occur in frequencies below 1 kHz and more typically below 100 Hz. It is therefore reasonable to constrain our attention to Maxwell's quasistatic equations ([65], [31]).

Maxwell's Quasistatic Equations

We begin with Maxwell's equations ([70], [31])

$$\nabla \cdot \mathbf{E} = \rho/\varepsilon_0 \tag{2.1}$$

$$\nabla \times \mathbf{E} = -\frac{\partial \mathbf{B}}{\partial t} \tag{2.2}$$

$$\nabla \cdot \mathbf{B} = 0 \tag{2.3}$$

$$\nabla \times \mathbf{B} = \mu_0(\mathbf{J} + \varepsilon_0 \frac{\partial \mathbf{E}}{\partial t}) \tag{2.4}$$

where ρ is the charge density, $\mathbf{J}$ is the current density, $\mathbf{E}$ is the electric field, $\mathbf{B}$ is the magnetic field. The permeability of tissue is assumed to be the same as that for free space, that is $\mu = \mu_0$ [31].

In the quasistatic approximation, we may treat the displacement, inductive and capacitive effects as negligible by setting $\partial \mathbf{B}/\partial t = 0$ and $\frac{\partial \mathbf{E}}{\partial t} = 0$. Equations (2.1)-(2.4) become the quasistatic approximations of Maxwell's equations and are given by

$$\nabla \cdot \mathbf{E} = \rho/\varepsilon_0 \tag{2.5}$$

$$\nabla \times \mathbf{E} = 0 \tag{2.6}$$

$$\nabla \cdot \mathbf{B} = 0 \tag{2.7}$$

$$\nabla \times \mathbf{B} = \mu_0 \mathbf{J} \tag{2.8}$$

where ρ is the charge density, ε_0 is the permittivity of free space and μ_0 is the permeabiity of free space. As a consequence, $\mathbf{J}$ only appears in the magnetic field equations. Notice also that the equations for electric and magnetic fields can be treated separately in this approximation. We treat the time it takes the signals to reach the sensors to be instantaneous.

The Magnetic Field Equations

Using the well known property that the divergence of a curl is always zero, $\nabla \cdot \mathbf{B} = 0$ can be rewritten as

$$\nabla \cdot (\nabla \times \mathbf{A}) = 0 \tag{2.9}$$

by setting $\mathbf{B} = \nabla \times \mathbf{A}$ and substituting back into equation (2.8),

$$\nabla \times \mathbf{B} = \nabla \times \nabla \times \mathbf{A} = \nabla(\nabla \cdot \mathbf{A}) - \Delta \mathbf{A} = -\Delta \mathbf{A} \tag{2.10}$$

$$\Delta \mathbf{A} = -\mu_0 \mathbf{J} \tag{2.11}$$

Equation (2.11) is a Poisson equation with solution

$$\mathbf{A}(\mathbf{r}) = \frac{\mu_0}{4\pi} \int_{\mathbb{R}^3} \frac{\mathbf{J}(\mathbf{r}')}{|\mathbf{r} - \mathbf{r}'|} \, \mathrm{d}\mathbf{r}' \tag{2.12}$$

when we assume the condition that the magnetic field is zero at infinity, $\mathbf{A}\,|r| \to \infty$. Then taking the curl on both sides we arrive at the well known Biot Savart equation

$$\mathbf{B}(\mathbf{r}) = \frac{\mu_0}{4\pi} \int_{\mathbb{R}^3} \mathbf{J}(\mathbf{r}') \times \frac{\mathbf{r}'}{|\mathbf{r} - \mathbf{r}'|^3} \, \mathrm{d}\mathbf{r}' \tag{2.13}$$

Once a boundary and the current sources $\mathbf{J}$ are specified, the forward equation will be fully described. In biological systems, magnetic fields are generated through ionic currents. Magnetic contaminants such as lung particles may also produce a magnetic field when moving or under the influence of an external field. In addition, magnetic particle tracers introduced intravenously may also produce a magnetic signature either by movement or under a changing magnetic field of sufficient amplitude.

A description is needed to describe the current density of the biological media. Currents are generated in biological tissue through the movement of ions such as K^+, Na^+, Ca^{2+},

Cl^-. These current sources happen within the conductive and capacitive medium of tissue, which induces extracellular currents caused by the electric field generated from the source current. The total current density can be described as the sum of these two current densities:

$$\mathbf{J} = \mathbf{J}_E + \mathbf{J}_S = \sigma\mathbf{E} + \mathbf{J}_S \tag{2.14}$$

$\mathbf{J}_E$ is called the ohmic current and $\mathbf{J}_S$ is the source or impressed current. $\mathbf{J}_E$ is also known as the current density of the volume conduction and $\mathbf{J}_S$ is also known as the primary current density. Setting $\mathbf{E} = -\nabla V$,

$$\mathbf{J} = \mathbf{J}_S - \sigma\nabla V \tag{2.15}$$

Substituting (2.15) into equation (2.13),

$$\mathbf{B}(\mathbf{r}) = \frac{\mu_0}{4\pi}\int_{\mathbb{R}^3}\mathbf{J}_S(\mathbf{r}')\times\frac{\mathbf{r}'}{|\mathbf{r}-\mathbf{r}'|^3}\,d\mathbf{r}' - \frac{\mu_0}{4\pi}\int_{\mathbb{R}^3}\sigma\nabla V(\mathbf{r}')\times\frac{\mathbf{r}'}{|\mathbf{r}-\mathbf{r}'|^3}\,d\mathbf{r}' \tag{2.16}$$

$$\mathbf{B}(\mathbf{r}) = \mathbf{B_0} - \frac{\mu_0}{4\pi}\int_{\mathbb{R}^3}\sigma\nabla V(\mathbf{r}')\times\frac{\mathbf{r}'}{|\mathbf{r}-\mathbf{r}'|^3}\,d\mathbf{r}' \tag{2.17}$$

where

$$\mathbf{B_0} = \frac{\mu_0}{4\pi}\int_{\mathbb{R}^3}\mathbf{J}_S(\mathbf{r}')\times\frac{\mathbf{r}'}{|\mathbf{r}-\mathbf{r}'|^3}\,d\mathbf{r}' \tag{2.18}$$

Here $\mathbf{B}_0$ depends only on the source currents independent of the conducting medium while the second term depends on the volume currents. It is also interesting to note that in an infinite conducting medium, the second term disappears ([31], [76], [28]). So in an infinite conducting media, one needs only consider the primary currents, the volume currents do not contribute at all.

Extending (2.17) to a piecewise homogeneous conductor [31], we obtain the formulation derived by Geselowitz [26]

$$\mathbf{B}(\mathbf{r}) = \mathbf{B_0} + \frac{\mu_0}{4\pi}\sum_{ij}(\sigma_i - \sigma_j)\int_{\mathbb{R}^3}\mathbf{V}(\mathbf{r}')\frac{\mathbf{r}-\mathbf{r}'}{|\mathbf{r}-\mathbf{r}'|^3}\times d\mathbf{S}'_{ij} \tag{2.19}$$

Magnetic Field of a Current Dipole

The continuous current density $\mathbf{J}$ can be discretized by dividing the volume within which current may occur (the brain space), into voxels with each voxel segment represented by a point current dipole. This process permits simplification of the Biot Savart equation to the discretized form for the magnetic field of a current dipole within a conducting volume. We proceed then by setting the impressed current, $\mathbf{J}_S = \mathbf{q}\delta_{\mathbf{r0}}(\mathbf{r})$ where $\mathbf{q}$ is the dipole moment, $\mathbf{r}_0$ is the location of the dipole, and the Dirac function δ at location $\mathbf{r}_0$ is used to discretize the continuous current density. Integration of (2.18) yields the familiar Biot Savart equation in an infinite conducting media or in a vacuum:

$$\mathbf{B_0} = \frac{\mu_0}{4\pi}\mathbf{q} \times \frac{\mathbf{r} - \mathbf{r}_0}{|\mathbf{r} - \mathbf{r}_0|^3} \tag{2.20}$$

If we impose a spherical boundary to the conducting medium and if we are only interested in measuring the magnetic field at a point outside this sphere (outside the head), then the following relation holds [76]

$$\mathbf{B} = -\nabla U \tag{2.21}$$

where U is a scalar potential that becomes zero at infinity. This is because in the quasistatic Maxwell's equations, the magnetic field is being measured in a domain with no current sources. Hence, $\nabla \times \mathbf{B} = 0$. The surface normal $d\mathbf{S}$ for a spherical shell is given by

$$\mathbf{n}(\mathbf{r}') = \frac{\mathbf{r}'}{|\mathbf{r}|'} \tag{2.22}$$

From (2.19), we can see that the spherical boundary may be a homogeneous sphere or a series of concentric homogeneous spheres.

Along the radial direction, the magnetic field equation is trivial because the volume current term vanishes. The radial component of (2.17) is simply obtained by taking the dot product along the unit vector $\mathbf{e}_r = \mathbf{r}|/|\mathbf{r}|$:

$$B_r = -\mathbf{B}(r) \cdot \mathbf{e}_r = \mathbf{B}(\mathbf{r}) \cdot \mathbf{r}/|\mathbf{r}| \tag{2.23}$$

$$\mathbf{B}(\mathbf{r}) \cdot \mathbf{r}/|\mathbf{r}| = \mathbf{B_0} \cdot \mathbf{r}/|\mathbf{r}| + \frac{\mu_0}{4\pi}\sum_{ij}(\sigma_i - \sigma_j)\int_{\mathbb{R}^3} \mathbf{V}(\mathbf{r}')\frac{\mathbf{r} - \mathbf{r}'}{|\mathbf{r} - \mathbf{r}'|^3} \times \mathrm{d}\mathbf{S}'_{ij} \cdot \mathbf{r}/|\mathbf{r}| \tag{2.24}$$

where (since the surface is now a sphere)

$$(\mathbf{r}-\mathbf{r}')\times \mathrm{d}\mathbf{S}'_{ij}\cdot\frac{\mathbf{r}}{|\mathbf{r}|}=(\mathbf{r}-\mathbf{r}')\times\mathbf{n}(\mathbf{r}')\cdot\frac{\mathbf{r}}{|\mathbf{r}|}=(\mathbf{r}-\mathbf{r}')\times\frac{\mathbf{r}'}{|\mathbf{r}'|}\cdot\frac{\mathbf{r}}{|\mathbf{r}|}=0 \tag{2.25}$$

which leaves the radial component of the magnetic field in a spherical conductor depending only on the first term

$$B_r=\mathbf{B_0}\cdot\mathbf{e}_r=\frac{\mu_0}{4\pi}\int_{\mathbb{R}^3}\mathbf{J}_S(\mathbf{r}')\times\frac{\mathbf{r}'}{|\mathbf{r}-\mathbf{r}'|^3}\cdot\mathbf{e}_r\,\mathrm{d}\mathbf{r}' \tag{2.26}$$

To derive the tangential components of the magnetic field, we return to the relation given in (2.21) and appealing to symmetry, a line integral for U may be written [27]

$$U(r)=-\int_0^\infty\nabla U(\mathbf{r}+t\mathbf{e}_r)\cdot\mathbf{e}_r\,\mathrm{d}t=\int_0^\infty\mathbf{B}(\mathbf{r}+t\mathbf{e}_r)\cdot\mathbf{e}_r\,\mathrm{d}t \tag{2.27}$$

We can immediately see that only the radial component survives the dot product, giving

$$U(r)=\int_0^\infty\mathbf{B}_r(\mathbf{r}+t\mathbf{e}_r)\cdot\mathbf{e}_r\,\mathrm{d}t \tag{2.28}$$

for a current dipole, we obtain

$$U(r)=\frac{\mu_0}{4\pi}\mathbf{q}\times(\mathbf{r}-\mathbf{r}_0)\cdot\mathbf{e}_r\int_0^\infty\frac{1}{|\mathbf{r}+t\mathbf{e}_r-\mathbf{r}_0|^3}\,\mathrm{d}t \tag{2.29}$$

and we arrive at the familiar formulation given by

$$U(r)=\frac{\mu_0}{4\pi}\frac{\mathbf{q}\times\mathbf{r}_0\cdot\mathbf{r}}{F} \tag{2.30}$$

where

$$\mathbf{a}=\mathbf{r}-\mathbf{r}_0 \tag{2.31}$$

$$F=a(ra+r^2-\mathbf{r}_0\cdot\mathbf{r}) \tag{2.32}$$

Taking the gradient, Sarvas' magnetic field equation of a current dipole in a conducting sphere is obtained [70].

$$\mathbf{B}(\mathbf{r})=\frac{\mu_0}{4\pi F^2}[F\mathbf{q}\times\mathbf{r}_0-(\mathbf{q}\times\mathbf{r}_0\cdot\mathbf{r})\nabla F] \tag{2.33}$$

where once again, μ_0 is the permeability of free space (vacuum) and

$$\nabla F = \hat{\mathbf{x}}\frac{\partial F}{\partial x} + \hat{\mathbf{y}}\frac{\partial F}{\partial y} + \hat{\mathbf{z}}\frac{\partial F}{\partial z} \tag{2.34}$$

substitution into (2.32) yields

$$\nabla F = (\frac{a^2}{r} + \frac{\mathbf{a}\cdot\mathbf{r}}{a} + 2a + 2r)\mathbf{r} - (a + 2r + \frac{\mathbf{a}\cdot\mathbf{r}}{a})\mathbf{r}_0$$

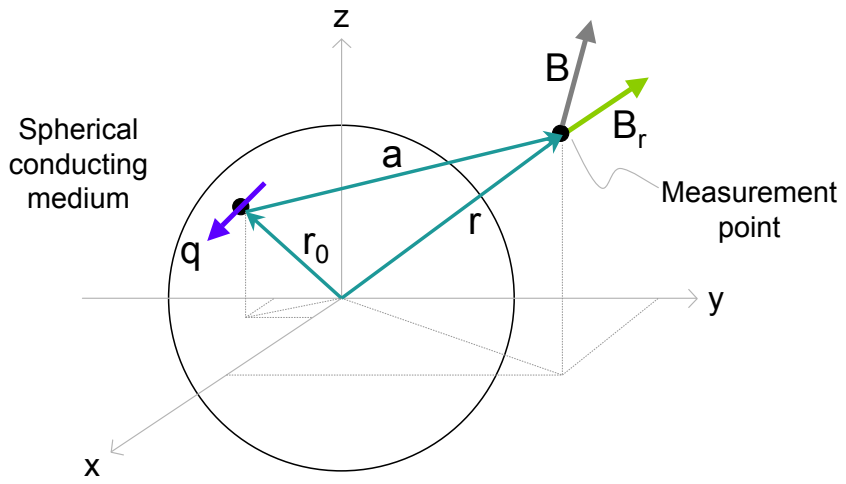

Figure 2.6: Equivalent current dipole in a spherical conducting media. q is the dipole moment. r_0 is the distance from the sphere centre to the dipole. r is the distance from the sphere centre to the measurement point. a is the distance between the dipole and the measurement point. B is the vector magnetic field at the measurement point due to the current dipole. B_r is the radial component of the magnetic field.

Figure 2.6 illustrates the geometry for this equation. It is useful to note that although the volume currents affect the tangential components of the magnetic field, this equation is independent of conductivity just like the special case for the radial component of the magnetic field. This makes the forward model very simple to compute and implies that when a sphere can approximate the volume conductor, the magnetic fields are not affected by the internal conductivities of the medium. As a consequence, MEG dipole fits are more accurate than EEG because in the EEG forward equations, the conductivity terms do not drop out.

Note too that dipoles, **q** that are radial to the sphere produce zero field because of the cross product terms in equation (2.33). As a direct consequence, MEG is known to be insensible to radial sources. Because the human head is not a perfect sphere, some leakage of nearly radial components will be detectable but the best solution to detect radial sources is to include EEG in the forward model.

The single sphere model has been very successful in modelling many types of cortical activity using different inverse methods. It is due to this independence of conductivity that this model is so widely adopted. An extension of this model is the so-called multiple local sphere model [55].

The Equivalent Current Dipole Model

In the previous sections, equations were developed that described a point dipole in a spherical conducting media. The method was developed in context of discretization of a conducting volume containing a current density, **J**. Using superposition principle, the total magnetic field is the vector integration over the volume conductor or in the case of the discretized volume, a vector sum. Under some circumstances, it is possible to model the brain activity using only a small number of discrete sources, setting the rest of the sources in the volume conductor to zero. The simplest brain source model is an infinitely small current element embedded within the conducting medium of the brain (Equivalent Current Dipole, or ECD), representing coherent activation of neurons located within a small area (of the order of about $1cm^2$). The ECD corresponds to intracellular current and it induces volume return currents in the conducting medium. The model is especially simple if a uniformly conducting sphere can represent the brain, however, the model has also been extended to spheroidal conducting media [19], multiple local sphere approximation [55], or realistic head shapes [61]. The model can be incrementally extended by the addition of more dipoles. The number of dipoles used in the model is dictated by the a priori factors and must be determined based by a strong hypothesis. Examples of brain functions that can be successfully modelled with ECD include somatosensory stimulation of the median nerve (one dipole, sometimes two), auditory evoked field (2 dipoles), motor (1 or two dipoles) and visual evoked field (one dipole to 4 dipoles). Epileptic spike generators are also very well modelled with single ECD.

An alternative view such as that used by beamformers considers each voxel in the vol-

ume separately and a vector sum will not yield the total magnetic field of the sources. This method will be discussed in context of the next chapter.

2.2.2 Noise and Artifact removal

Because the magnetic fields from brain signals are very small, the influence of biological and environmental noise can have a significant impact on MEG measurements. Signal to noise is a ratio computed that quantifies the quality of brain signals extracted compared to the noise encountered. Environmental sources of noise include the sensor themselves, which has a white noise profile. Typical low Tc MEG gradiometer sensors have noise floors below 10 fT rms/sqrt(Hz). This noise floor extends down to below 1 Hz and up to the Nyquist frequency. In contrast, transient noise may also be encountered from changes in the magnetic environment in and around the measuring device including moving cars, trains, the power line, elevators and other machinery that may emit a magnetic field. While shielding will dampen the effects, these environmental signals cannot be completely eliminated. Biological sources of noise include other current generating signals in the body as well as movement. These include eye movements, which are typically an order of magnitude larger than brain signals, the heart, and general background brain noise. Dental appliances and other body implants or ferrous material attached to the body will generate magnetic field through galvanic processes or movement. Techniques have been devised to reduce the effects of noise [90]. White noise or noise of a random nature can be reduced through signal averaging. The amount of noise reduction is given roughly by the square root of the number of epochs in the average. Events phase locked to the average are undisturbed while the randomness that is not phase locked will diminish in amplitude. This method is successful in extracting evoked signals from the MEG data. By averaging in the frequency domain, frequency bands of time locked (but not necessarily phase locked) events can emerge. Filtering the data will remove power line noise as well as low frequency drifts. A reliable and uncontroversial technique is to simply remove segments of data where artifacts appear and not use them in subsequent analysis. This has the advantage that any secondary brain signals that may be generated from the artifact (such as in the case of an eye blink causing potential visual effects), may also be reduced. However, if very few epochs are collected, the number of noise free epochs may be greatly reduced.

An alternative is to clean the data using methods like independent component analysis and principle component analysis. These techniques work by creating a basis set of signals using criteria such as statistical independence or orthogonality. Components containing the artifact are assumed to exist in a subspace separate from the signal and these components are removed. This assumption is not always met and some signal may ultimately be removed as well. Source modelling methods like beamformers have a built in spatial filter that attempts to reduce the effects of artifacts generated from other spatial locations. In CTF MEG systems, a technique called 3rd order gradient correction is applied ([91], [23]). This technique creates synthetic 3rd order gradiometers using a linear combination of reference channels which are positioned about 27 cm away from the head surface. These coils measure more environmental field and less brain signals and have the effect of synthesizing a gradiometer of a higher order. The higher order gradiometers cancel noise. In Elekta systems, SSS or signal space separation and tSSS (temporal SSS) is used for noise removal [22]. The signal space is separated into three domains defined by two concentric spheres. Within the smallest sphere is the brain region only. Between the brain region and the outside fields is the space where all the sensors are found. Outside the largest sphere is the region with no sources and no sensors. Utilizing Maxwell's equations and the fact that the harmonic functions for the space outside can be separated from the harmonic functions from the space inside. This technique then removes components of noise by subtracting harmonic function components from the space outside. The resulting cleaned data is well suited for equivalent dipole modelling but as a consequence of the harmonic subtraction the rank of the subspace preserved is greatly reduced which can be problematic to methods like beamformer, which relies on an inversion of a covariance matrix.

2.3 The Inverse Problem

2.3.1 The Lead Field Equation

MEG records the magnetic fields from the brain using an array of SQUID sensors surrounding the outside surface of the head. Like EEG, these recorded sensors may be used directly to describe the nature of the recorded brain functions. Through techniques like signal averaging, event related signals that are phase locked to a trigger can be clearly described

from the temporal and spatial distribution of field patterns on the helmet shaped surface. Much can be determined using this data such as differences between stimulus conditions and when the patterns are simple, the number of potential source generators. The only irrefutable results with MEG are the sensor level signals because this is the collected data. Any conclusions drawn about the sources must by it's very nature involve assumptions and a model. A drawback to sensor level analysis is the variable nature of head position. Because the subject can be placed anywhere in the helmet region and head sizes differ, signal to noise will vary from collection to collection and from person to person. The location of the head is determined by tracking a set of magnetic dipoles placed on rigid locations on the subject's head. For the CTF systems, 3 head positioning coils are used typically placed on the fiducial locations at the left and right pre-auricular points and the nasion. These create the local or head coordinate system, which moves with the subject. The dewar or device coordinates are defined rigid to the sensor array. The coils are located relative to the dewar coordinates. Everything else is located relative to the head coordinates. For the Elekta system, 5 head position coils are placed in arbitrary locations on the head. The fiducials are defined using a pohemus digitizer also on the left and right pre-auricular points and the nasion.

In the last chapter the forward problem was introduced which described the equations for the magnetic field given a description of the source activity and the shape of the conductor model. The forward problem can be viewed as finding values Y (the magnetic field) given a description of the source activity (X) (position, orientation, moment) and the magnetic field equations. The magnetic field at sensor Y is obtained by computing the magnetic field equations for each X and summing the field contributions together. One could reformulate this problem in this simple linear equation:

$$\mathbf{m} = \mathbf{L} \cdot \mathbf{J} \tag{2.35}$$

where $\mathbf{m}$ is an M-dimensional column vector of measured fields, where M is the number of sensors. Its length is equal to the number of sensors. $\mathbf{L}$ is the so called lead field. L is an M x N matrix, where N is the number of sources and M are the number of sensors. The lead field is the magnetic field at each sensor and source location for a unit source moment. The amplitude of the sources are factored out into the $\mathbf{J}$ term which has dimensions equal to the number of sources which includes noise sources. If the dipole equations were invertible,

we could determine exactly the source values given m by solving the set of linear equations. However, the equations are not invertible. In fact there are an infinite number of possible sets of **J** that can give rise to the observed fields **m**. The problem is highly underdetermined and not unique. We are therefore faced with having to find the best set of **J** that best fits the data **m** given the lead field **L**. This is the inverse problem for MEG.

The inverse problem is actually a general technique used in many areas of research and can be stated in general as follows: "Given a set of observables, Y, and model L, what are the values X that produce the best explanation for Y?" It's basic form follows the linear equation described in 2.35. The techniques that govern the best-fit criteria form the basis of inverse problem technique strategies. Because the measured field is never equal model data, a noise term is included in the formulation

$$\mathbf{m} = \mathbf{L} \cdot \mathbf{J} + \mathbf{n} \tag{2.36}$$

Reciprocity and Non-Uniqueness

The inverse solution to MEG is non-unique ([18], [67]). There are three main reasons for this:

1. A unique solution would violate Helmholtz's Reciprocity principle ([35], [61]). Given two points A and B, where A is the location of a magnetic source and B is the location of a detector, reciprocity states that you can swap source for detector without changing anything. In three dimensions, it is impossible to impress an isolated current within a conducting media from any combination of fields from the surface or on the outside. Reciprocity requires then that the reverse is also true: there is no combination of measured fields that are unique to the interior of the conducting media.

2. Some current sources can produce zero field. For example, there could be cancellation of source activity. In addition, for a spherical homogeneous conducting medium, the radial component of a current source produces zero field.

3. If more sources exist than sensors, then, the inverse solution is also non-unique. This is called an underdetermined problem. In linear algebra, this implies an infinite number of solutions because there are fewer equations than unknowns. The MEG

inverse problem is highly ill-posed given there are far more source generators (tens of thousands) than sensors (hundreds).

Fokas [24] gives a rigorous proof of this non-uniqueness principle by proving that certain components of the current is independent the field function outside the conductor. Because of non-uniqueness of the inverse solution, it is necessary to impose constraints and use a priori information to judge the validity of the source solution.

2.3.2 Equivalent Dipole Modelling

The simplest inverse technique with the longest history in MEG is equivalent dipole modelling ([57], [88]). It involves reducing the number of sources to a very small number, typically 1 or 2 and perhaps as many as 10. The number is determined by physiological considerations and/or by review of scalp contour map profiles. A current dipole has a very distinct scalp map pattern and when there are only a few, it is sometimes clear based on map topography the number of dominant dipoles that may be needed in the model. Singular value decomposition can also be used to count the number of significant source generators. In this technique then, the number of dipoles is predetermined before modelling. The lead-field equation given by 2.36 is minimized by using a cost function such as the least squares criteria given by:

$$min \frac{|\mathbf{m} - \mathbf{L} \cdot \mathbf{J}|^2}{|\mathbf{m}|^2} \tag{2.37}$$

The ratio expressed as a percentage gives the residual error and inversely the goodness of fit. The values of m can be from a single time point or a series of time points. When the fit is computed over a series of time points, the dipole positions can be allowed to change at each time point (moving dipole fit) or only the dipole moment is allowed to vary over the time points (spatial temporal fit). Figure 2.7 depicts a dipole fit using the CTF dipole fitting software. The figure illustrates a two dipole fit of the M100 neuromagnetic response of auditory evoked data.

Minimization techniques such as the Levenberg-Marquartdt and the Nelder-Meade downhill simplex are used to search the source space for the solution that minimizes the least squares fit [59]. For example, for the Nelder-Meade downhill simplex, a set of n+1 dipoles

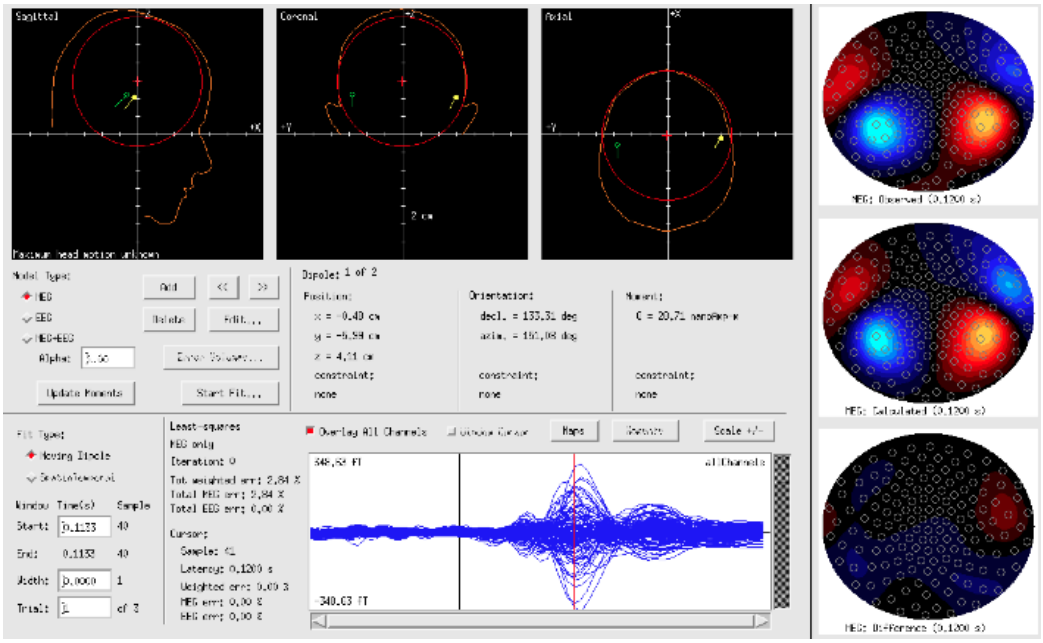

Figure 2.7: An example of a 2 dipole fit using the CTF DipoleFit program. The dipole is shown in three views: saggital, coronal and axial. The data shown is auditory evoked data. The data is fit at a single time point at around the M100 response. The computed data (middle map) based on the dipole locations shown varies in a least squares sense from the measured data (top map) by less than 3% (lower map).

are selected around the starting dipole location, where n is the number of search variables (in this case 3 position and two orientation directions for each dipole - the radial component is set to zero). The leadfield for these source locations are computed. The simplex favours the dipole positions that minimizes the least squares condition. Simplex methods are sensitive to starting conditions and are prone to local minima. The simplex fit should be restarted with new locations to avoid local minima. The larger the number of dipoles, the more likely a local minimum is found. Montecarlo error volumes generated by adding random noise to the system can be used to judge the stability of a source solution. The goodness of fit, computed by taking the difference between the measured data and the computed data based on the found source locations gives another criteria to judge how well the sources fit the data. When the data is very dipolar, the goodness of fit can exceed 99%. It should be cautioned however, that one can always manufacture an excellent goodness of

fit by continually adding more dipoles to the model. The additional dipoles fit to noise, reducing the goodness of fit but these dipoles have unstable solutions and will be reflected for example in the error volumes generated from Monte Carlo simulation checks (Figure 2.8).

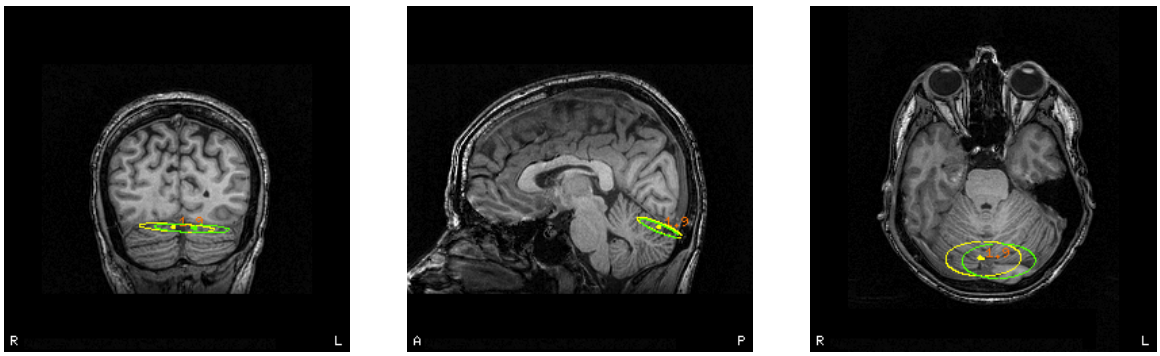

(a) Coronal (b) Sagittal (c) Axial

Figure 2.8: Coronal, Sagittal and Axial views of 95% confidence error volumes. The error ellipsoids are computed by repeating 100 dipole fits with added random noise. In this case, the noise level was selected based on the inter-trial noise variance. The ellipsoid that describes 95% of the variation is determined from the spread of the dipole fits. This is known as a Monte Carlo simulation.

2.3.3 The SAM Beamformer

Another technique for finding source solutions falls under the general classification of source scanning techniques known as beamformers [81]. Beamformers operate on each voxel in source space independently. At each location, a set of weights is constructed to form a linear combination of the measured sensor data. These weights aim to "steer" the sensors so that magnetic signals from the target voxel are summed constructively while other signals are summed destructively. Hence beamformers minimizes all measured signal except for those that are defined by the signal-space vector predicted using the forward model. The synthetic aperture magnetometry beamformer or SAM is an adaptive minimum-variance scalar beamformer, which uses a current dipole with a fixed orientation forward model [89]. The orientation is selected by scanning the tangential plane at the

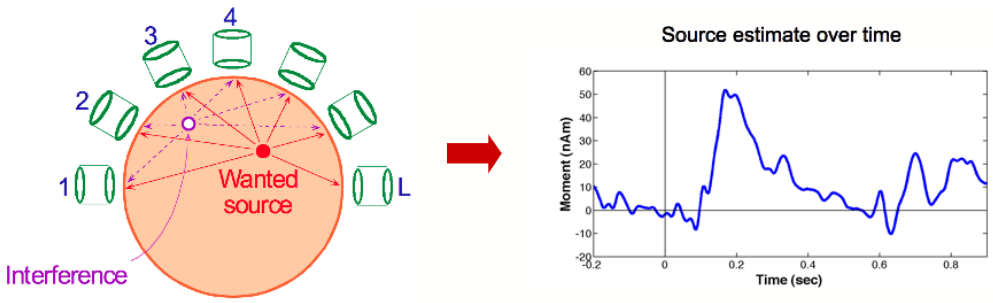

Figure 2.9: Beamformers are computed at a single voxel. A set of weights are computed that that selects for activity at the location of interest while suppressing interference from other locations (left image). A virtual channel that describes source activity over time is computed from these weights (right image). This is then repeated for the next voxel.

voxel location and finding the orientation that maximizes the projected signal. In reality it is impossible to zero the effects of all external signals while preserving the signal at the voxel of interest. For an axial gradiometer, the region of least sensitivity is directly below the sensor (the null region). By using all the sensors, the beamformer steers sensitivity patterns of the sensors in such a way as to create nulls at interfering sources while preserving the signal at the voxel and orientation of interest.

Equation 2.36 is inverted by selecting a series of weights that are applied to the measured fields at each MEG sensor. Let S be the source moment at location θ over a window of time of interest. The source is computed by applying appropriate weights to measured signals:

$$S_\theta = \mathbf{w}_\theta^T \cdot \mathbf{m} \tag{2.38}$$

where $\mathbf{m}$ are the measured signals and $\mathbf{w}$ is a matrix of weights. It can be shown that these weights are computed by minimizing the power given by

$$P_\theta = \mathbf{w}_\theta^T \mathbf{C} \mathbf{w}_\theta \tag{2.39}$$

and subject to

$$\mathbf{w}_\theta^T B_\theta = 1 \tag{2.40}$$

$$\mathbf{w}_\theta^T \Sigma \mathbf{w}_\theta < \psi^2 \tag{2.41}$$

where Σ is the projected noise and ψ^2 is some threshold value and B are the measured fields. This results in the relation

$$\mathbf{w}_\theta = \frac{(\mathbf{C}+\mu\Sigma)^{-1}\mathbf{B}_\theta}{\mathbf{B}_\theta^T(\mathbf{C}+\mu\Sigma)^{-1}\mathbf{B}_\theta} \tag{2.42}$$

C is the covariance matrix given by

$$\mathbf{C} = \frac{1}{T}\sum_{t=1}^{T}(x_i(t)-\mu)(x_j(t)-\mu), i, j = 1, ...M \tag{2.43}$$

M=number of sensors.

The weights applied to the measured data form a virtual channel, which aims to describe the source moment over time at the voxel location. This process is then repeated for every voxel in the brain. Hence a description of the moment over time is computed for every voxel. Volumetric images are computed by performing operations on these virtual channels. For example, a pseudo-Z score can be computed by taking the ratio between the source power over a specific bandwidth and time window and the projected sensor noise variance. Event related beamformers utilize the time locked averages of these virtual channels ([66], [12]). Figures 2.10, 2.11, 2.12 illustrate some examples of outputs from SAM beamformer analysis. Generally a volumetric image over a window of time is computed and locations of peak activity are determined. Virtual sensors at these locations are then analyzed in time and frequency and compared across conditions.

Correlated Sources

Minimum variance beamformers rely on sources being uncorrelated. If not - various distortions and reduction in signal to noise as a result of cancellation may occur. Signals from correlated sources can be strongly attenuated. In addition, nearby sources - even if uncorrelated - can reduce the estimated source strength of the target voxel. However, sources must be highly correlated over the entire period of estimation for the beamformer to fail completely. VanVeen estimated the correlation needed to be above 80% [81]. To address this

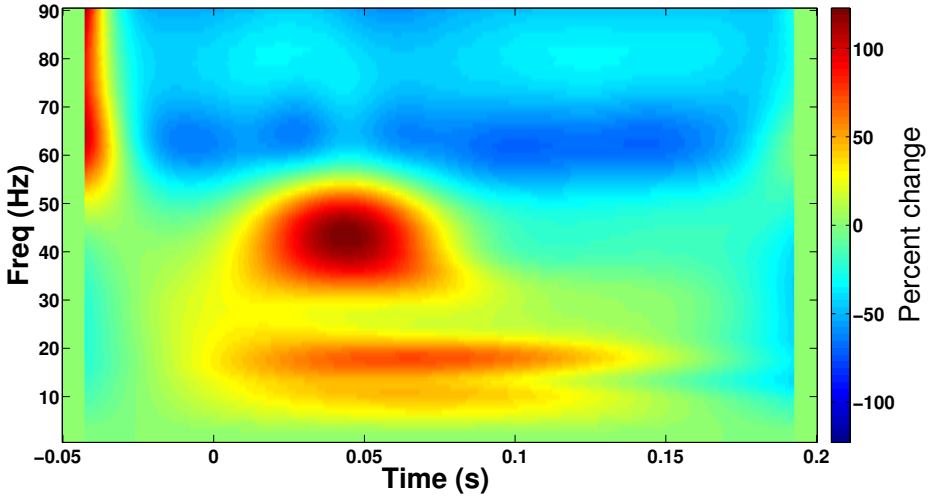

Figure 2.10: Example SAM beamformer output: time frequency plot of a virtual channel from somatosensory data. A peak activity can be observed at around 50 ms between 30 and 50 Hz. This information can inform bandwidth selections for source analysis.

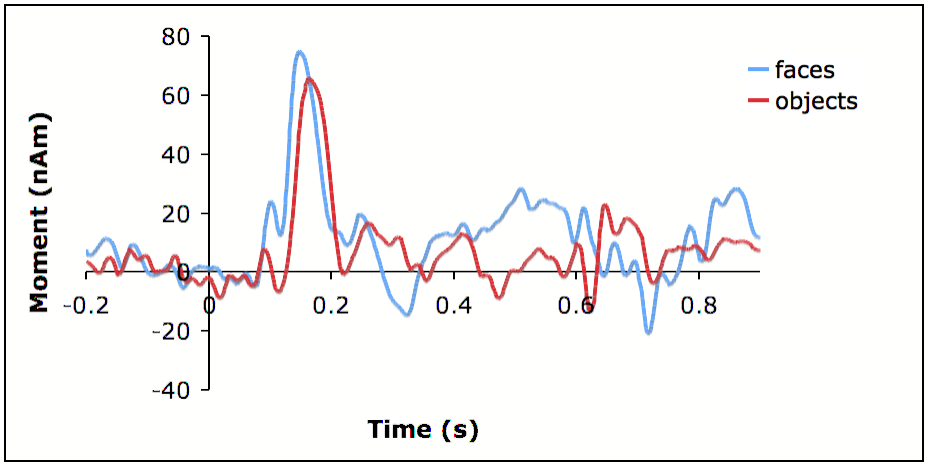

Figure 2.11: Example SAM beamformer output: virtual channel comparison of two conditions. The face condition (blue) appear to occur earlier and with larger amplitude than the object condition.

problem, consider using a larger time window to construct the covariance matrix. Multi-source beamformers and nulling beamformers have also been developed to address this

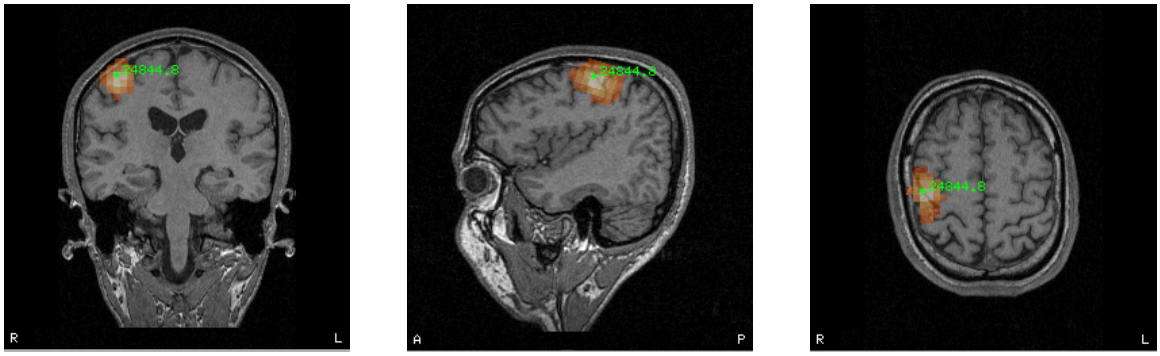

(a) coronal (b) sagittal (c) axial

Figure 2.12: Example SAM beamformer output: functional image. The data shows the SAM peak from somatosensory evoked data.

situation [56].

Covariance Rank

Beamformers rely on the construction of an invertible covariance matrix from a time window of data across all sensors ([84]). Beamformers also rely on an estimation of the sensor noise. The rank of the covariance matrix depends strongly on whether the covariance is constructed using averaged or unaveraged data and the amount of data used. The rank of the covariance matrix of unaveraged data can further be affected by the choice of processing techniques applied prior to beamforming. Head position correction and signal space separation are two processing techniques that will affect the rank of the original unaveraged data because these techniques remove the noise subspace. In order to invert a covariance matrix that is degenerate, noise is added to the diagonal. The amount of noise depends on the degeneracy and has the affect of smearing the beamform peaks. Another approach is to invert the covariance in a non-degenerate subspace.

Chapter 3

A Magnetic Source Phantom for MEG Calibration

3.1 Device ground truth using a single dipole phantom

[1]

3.1.1 Abstract

We describe the construction of a single magnetic dipole phantom with a hardware-independent microcontroller operated on a DC voltage input. Thus the phantom and microcontroller can be taken to different MEG labs regardless of manufacturer and power line voltages. The microcontroller was preset to a constant current and data from the phantom was collected at different MEG sites from different manufacturers in North America and in Europe. Data was preprocessed using device specific software to remove environmental noise such as 3rd gradient correction for CTF data and signal space separation for Elekta data. All preprocessed data were converted to CTF format for further analysis. A modified dipole fitting program was created with a point magnetic dipole forward model. The phantom dipole moment, and positions were fitted for the data from each site. From the MEG machines we have measured so far, the dipole moments were very consistent, varying by about 4%

[1] A version of the abstract has been submitted to Biomag 2012. Cheung, T, Lui, J, Furlong, P, Wilton, C, Braeutigam, S, Parameswaran. Device ground truth using a single dipole phantom.

from each other. This phantom offers a potential ground truth for comparing MEG devices providing a controlled and reproducible magnetic field to compare MEG machines directly for projects that span different sites.

3.1.2 Introduction

MEG devices have been slowly growing in number throughout the major medical and research centres around the world. Devices from several manufacturers as well as custom made machines are available for researchers and clinicians to use. Figures 3.1 shows a CTF installation. Figure 3.2 shows equivalent diagrams for Elekta. As more research is being reported from these machines and as centres upgrade from one machine to another, there is a growing desire to understand if these machines are reporting the same measurements. If not, how do they differ? Machine calibration is manufacturer dependent and while a flux quanta is a constant value, the gains employed to convert flux to field or gradient may be manufacturer or indeed machine dependent. It has been common practice that a phantom is delivered along with the MEG machine and that it is utilized to confirm consistent machine calibration over the lifetime of the system. Typically, the position of the dipole rather than the amplitude is used to judge machine accuracy. Each machine has it's own unique phantom which is used on a routine basis to check the machine's calibration. These phantoms come in different forms. For example, CTF has two phantoms: a dry magnetic dipole phantom with a single coil wound magnetic dipole mounted at a precise location relative to the fiducial coordinates (Figure 3.4); and a wet current dipole phantom consisting of 1 to 9 current dipoles with variable mount points and depth adjustability within a spherical saline solution (Figure 3.3). The former is used to check machine accuracy while the latter is used to test source modelling accuracies ([11]).

Elekta has a dry triangular current dipole phantom consisting of singly energized current dipoles at 32 locations around two planes mounted precisely relative to fiducial coordinates (Figures 3.5 and 3.6). Every MEG system will have a history of phantom collections, which will typically be very consistent over time. For example, the DSRF phantom over 8 years of collections never varies beyond 1/2 mm from its mean location. [2] However, there

[2]It should be noted that in the case of the Elekta phantom, the fiducial locations are digitized using a Polhemus device because the hpi locations for a human subject do not typically coincide with the fiducial

Figure 3.1: CTF Installation at Down Syndrome Research Foundation, Burnaby, BC, Canada

Figure 3.2: A Neuromag Vectorview System. Photo reproduced with permission from Elekta Oy, Helsinki, Finland.

locations. In the case of the phantom however, they do coincide and the digitization is actually redundant.

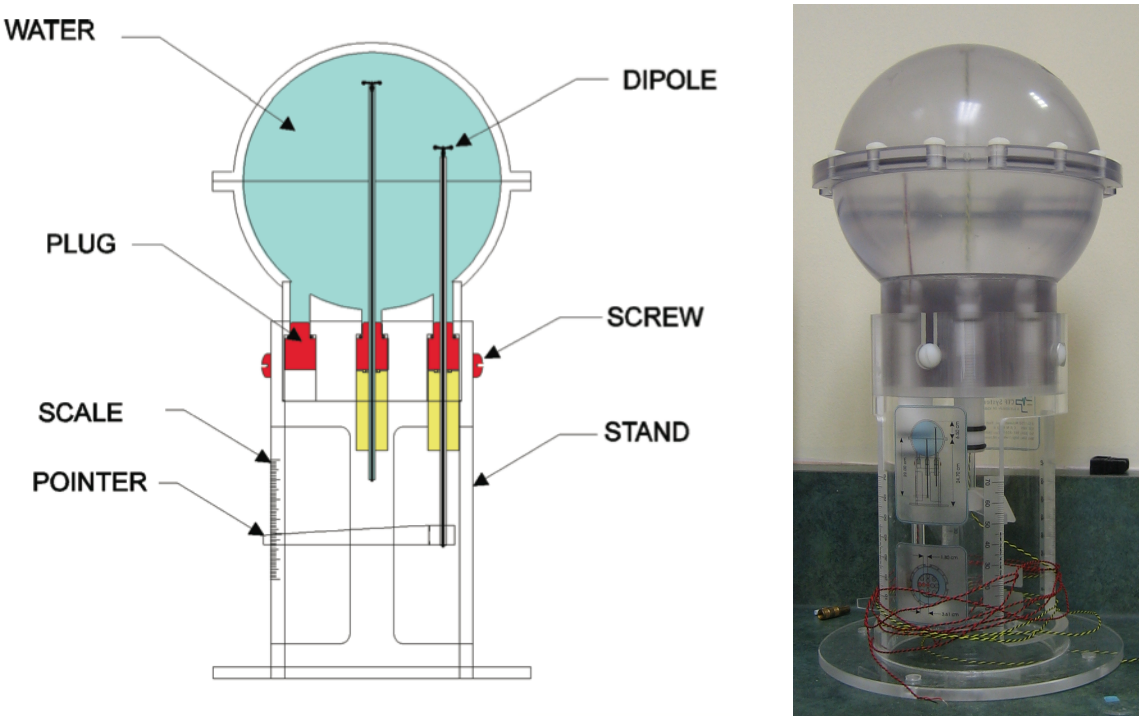

Figure 3.3: CTF Current Dipole Phantom. The conducting media is a saline solution. Current dipoles are inserted from the bottom of the unit. The dipole locations are measured using a pointer attached to the dipole and a calibrated scale along the side of the phantom stand.

have been few reported studies which uses the same phantom on different MEG systems [3] Part of the challenge is that the phantoms delivered with the MEG systems are hardware dependent relying on the MEG electronics to drive the phantom dipole. The CTF magnetic phantom is driven through the head coil box and a user-selectable resistor and voltage specifies the amplitude and frequency. A special lemo connector is used to connect the phantom's twisted pair cable to the head coil box. The CTF current dipole phantom utilizes a custom-made current-isolator controller with BNC or lemo connection points. This

Since the digitized locations are used to form the coordinate system, rather than the hpi locations, the phantom dipole localization is only as good as the Polhemus results. A poor digitization, results in poor localization of the phantom.

[3]CTF collected the same phantom on every MEG device manufactured in the 1990's, however, different electronics were used to drive the phantom.

Figure 3.4: CTF Magnetic Dipole Phantom. This phantom consists of a single magnetic dipole located 5cm above the centre of the stand. 4 holes, placed 90 degrees apart along the base of the stand are used to hold head localization coils. These coils form the local "head" coordinate system.

hardware permits multiple dipoles to be energized simultaneously as each current driver does not share the same ground, thereby avoiding any cross current circuits this might create. The Elekta phantom connects all 32 dipoles to a special cable, which resembles a parallel port and plugs into the Elekta electronics. Only one dipole is energized at a time at a specific frequency and user-controlled amplitude. Thus an independent measure is not possible without constructing specialized cables to interface with the phantom's connectors and without providing an independent current driver. The first phantom we describe is to construct a hardware independent phantom driven with a microcontroller that can be taken to different MEG labs for independent measures.

There have been a few studies that examine the question of cross-site comparability of MEG signals [47]. A current study under way between York (4 D), Oxford (Elekta) and Nottingham (CTF) will measure a set of n same subjects using the same stimuli from each of the these three sites. Recently also, several sites have had two MEG systems (CTF and Elekta) active simultaneously (Aston in Birmingham and CHOP in Philadelphia). The same subjects have been measured from both machines. What has been missing is the ability to directly compare these machines using exactly the same controlled magnetic fields and this

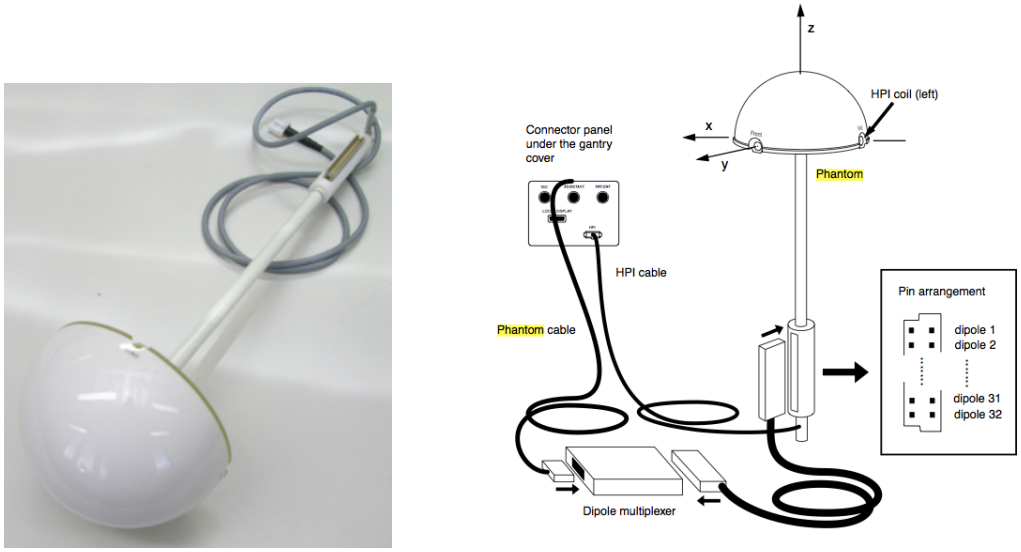

Figure 3.5: Elekta Phantom. This phantom contains 32 triangular dipole sources which can be modelled using the current dipole model if the coordinate system is centred at the tip of the triangular sources. This local coordinate system can be seen in the diagram on the left. Photo and diagram reproduced by kind permission from Elekta Oy, Helsinki, Finland.

is where we find use for our phantom. A comparison between MEG machines has not been recently undertaken and it is the purpose of this study to examine the current state of MEG cross-comparability between sites and between manufacturers. We have designed a phantom and microcontroller that focuses on portability and reproducibility of results to provide a stable device for cross platform comparison.

3.1.3 Methods

The goal was to select and construct components for a phantom driven by an independent current driver that could be transported to different labs possibly in different continents for testing. The phantom must have rigidly fixed magnetic field generators and a rigid coordinate system that could be collected in the same manner independent of system constraints. The current driver must be able to handle 50 and 60 Hz power line frequencies as well as 120-220 V power mains and produce consistent constant oscillating current to drive the

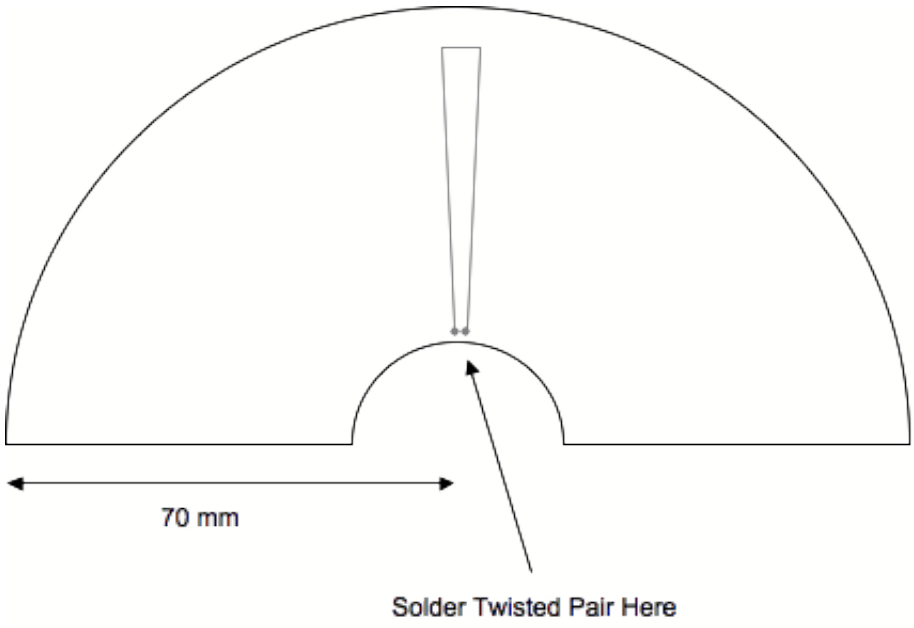

Figure 3.6: Triangular Dipole Phantom. The diagram shows the layout for a triangular dipole. The semicircular disk is made of nonmagnetic material. The dipole is shown in grey and is in the shape of an isosceles triangle with the base at the top and the tip at the bottom. The magnetic field activity will come primarily from the short 5-10 mm horizontal length at the top of the diagram. The tip of the dipole terminates at two points where a twisted pair would be soldered.

phantom.

Choice of Dipole

Since dipoles are often the choice for magnetic field generator in the forward model, it was a natural choice for our hardware phantom model. For the specific purpose of our current study, a single dipole placed in a precise coordinate system was sufficient. Multiple dipoles

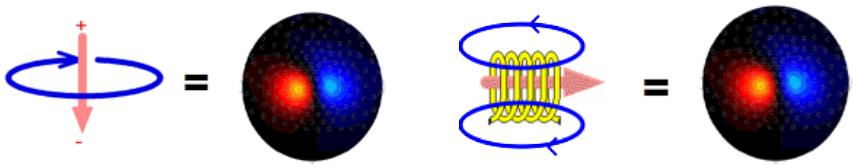

(a) Current Dipole (b) Magnetic Dipole

Figure 3.7: Current dipole vs magnetic dipole. (a) The magnetic field of a current dipole curls around the direction of the current source. (b) The magnetic field of a magnetic dipole curls around the loops of wire. A current dipole oriented from top to bottom has the same topographical field pattern as a magnetic dipole oriented from left to right.

would add to the complexity and were not necessary to meet the goals for this study.

Dipoles come in two forms: magnetic and current. A current dipole consists of a source and sink with the magnetic field generated by the moving current between source and sink. Magnetic fields from other parts of the circuit are shielded, canceled or kept far away from the MEG sensors. Typically the cable that delivers the current is constructed by twisting two insulated wires together thereby canceling the magnetic fields generated along the wire's length. In contrast, a magnetic dipole is a circular loop (or multiple loops) of wire with two poles. The magnetic field is generated from the summation of the current flowing around the coiled wire. Figure 3.7 illustrates the topography of the positive and negative magnetic field patterns between a current versus a magnetic dipole. Whereas the right-hand rule for current along a wire is used to describe the field pattern of the current dipole, the right-hand rule for solenoids is used for the magnetic dipole. It should be noted that one cannot distinguish a magnetic and current dipole source based solely on its topography. However, it is necessary to know what kind of dipole is generating the field for accurate source modelling.

Magnetic dipoles can be constructed by winding wire around a cylindrical non-conducting core. They may also be constructed as a single loop or a flat spiral. The latter two techniques can be etched onto printed circuit boards. See figure 3.8. To avoid connection point artifacts, a continuous wire can be used to create the dipoles, using the centre of a long wire to construct the dipole and then twisting the remaining wire to it's end points. These dipoles do not use the same forward model as neuronal generators. Forward equations need

to be adjusted for localization of these dipoles.

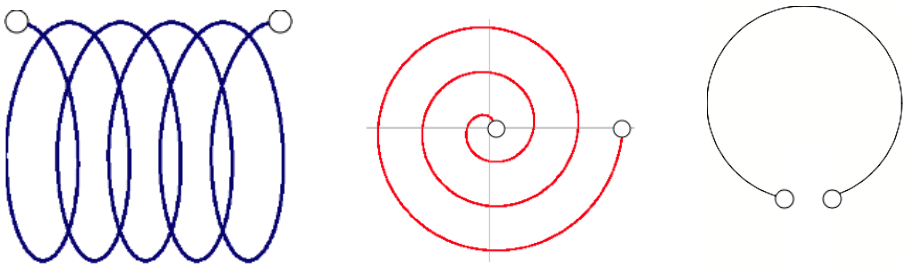

(a) Helical (b) Spiral (c) Circular

Figure 3.8: Examples of m,agnetic dipoles: termination points are connected to a twisted pair cable.

Current dipoles in a conducting media (wet phantom) are made of a twisted pair of insulated wires, which terminate at a positive and negative electrode. These two electrodes are immersed in a conducting ionic medium, which allow a circuit to complete between the two electrodes (figure 3.9). If the conducting media is to be modelled using boundary or finite element methods, the location and shape of the conducting media is included in the modelling. If the conducting media is a spherical volume, the equations for a current dipole in a spherical conductor may be used. In this case, it is important that the local coordinate system is placed at the centre of the conducting sphere. Current dipoles in a conducting media are the basis of the CTF spherical wet phantom. Another type of current dipole phantom was proposed by Ilmoniemi [38] which utilizes the fact that radial dipoles produces zero field. This dry current dipole phantom is constructed using thin isosceles triangles (figure 3.6) with the dipole being the triangle's base and the local coordinate system centred at the vertex opposite this base. The current from the two legs of the isosceles triangle is radial relative to this coordinate system and therefore does not contribute to the field. With this coordinate system, the equation for a current dipole in a conducting media may also be used. Triangular dipoles are the basis of the Elekta phantom. Both types of current dipole have a finite length between 5 mm and 10 mm, though they are modelled using point dipoles. As long as the dipole is far enough away from the sensors, the finite dimension will not deviate too much from those of a point dipole. These dipoles use the same forward model as neuronal signals and do not need adjustment of forward equations

for localizing the dipoles.

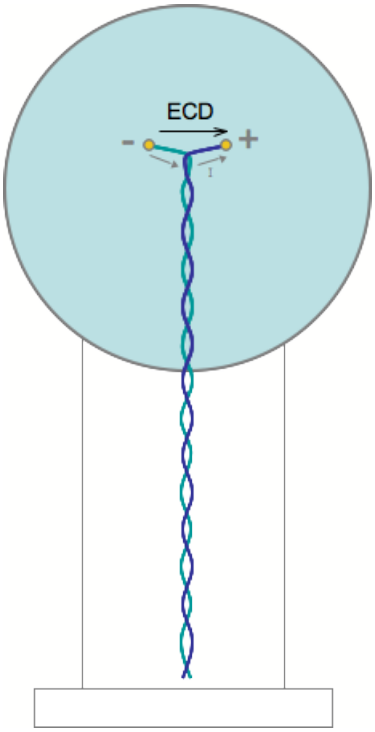

Figure 3.9: Current dipole in a conducting media (saline solution). The dipole is made by twisting two insulated wires together. Where the wire terminates, the insulation is stripped and gold balls are attached to form the dipole source and sink.

In terms of reproducibility and stability, current dipoles in a conducting media is not suitable as the electrolyte will need replenishing over time and could change composition as the electric circuit may cause a chemical reaction to occur. In addition there is a concern about the linearity between the source signal and the magnetic field as a result of the electrical double layer around the electrodes in the saline water [[80]]. In terms of portability, the wet phantom with its liquid or gelatinous conducting media is harder to transport. The dry dipole options are more suitable for stable reproducible signals as well as for portability.

Hand-wound helical magnetic dipoles have been chosen for our phantom for reasons of cost and construction simplicity. Helical magnetic dipoles have a more general coordinate system than triangular dipoles. The triangular current dipoles require a coordinate system to be centred with the tip of the long isosceles triangle, the artificial "sphere" centre as

shown in figure 3.6. It is this geometry that equates to a current dipole in a spherical conducting media. As well, care would also have to be exercised in the choice of substrate and method for etching used to create a non-magnetic printed circuit board. On the other hand, triangular dipoles do not need a different forward model to that of neuronal dipoles. However, we will need to employ magnetic dipoles anyways to define the local coordinate system ("head" localization) since the device coordinate for the head localization coils are arbitrary and cannot be tied to an artificial "sphere" centre. Changing the forward model to that of magnetic dipoles does not alter the purpose of comparing cross-site measurements.

The general nature of magnetic dipoles makes them ideal choices for head position coils. All the MEG systems utilize magnetic dipoles for head positioning. It does not require selection of precise coordinates as the triangular dipoles do and is generally more flexible.

Size of dipole

We wish to obtain a field, which can be approximated by a point dipole to simplify the forward problem. To achieve a field pattern of a point dipole, we need to consider the relative size of the dipole compared to its distance from the sensor array. We can assume the closest distance from the closest sensor pickup coil and the dipole is approximately 35 mm. This includes the distance from the coil to the inside dewar wall through the vacuum space to the outside of the dewar if the dipole were placed directly below a sensing coil. Practically, this is probably the closest the dipole will come to any sensor, though the value will vary a little between manufacturers. Consider then the simple case of a single coil loop to represent the dipole. The on-axis magnetic field can be derived through amperes' law and is given by

$$B = \frac{\mu_0 I r^2}{2(r^2 + a^2)^{3/2}} \tag{3.1}$$

where r is the radius of the loop, a is the distance from the centre of the loop to the measurement point along the axis, μ_0 is the permeability of free space and I is the current. If $a >> r$, then we have the equation for a point dipole along the axis of symmetry,

$$B = \frac{\mu_0 i r^2}{2(a^2)^{3/2}} \tag{3.2}$$

Expressing a as a multiple of r

$$a = nr \tag{3.3}$$

and taking the ratio of the two equations, we obtain the relation

$$\frac{n^3}{(n^2+1)^{3/2}} \tag{3.4}$$

which expresses the ratio between the on-axis field of a finite loop and a point dipole. Hence if we want to achieve a better than 98.5% agreement between the point dipole and the finite coil field equations, a must be larger than 10 times the radius or 5 times the diameter of the coil. For a coil with 1 mm diameter, the dipole must be at least 5 mm away. Since the dipole will be at least 35 mm, we can reliably approximate the magnetic field equation with a point dipole.

The general equation for a point dipole is given by

$$\mathbf{B}(\mathbf{r}) = \frac{3(\mathbf{m}\cdot(\mathbf{r}-\mathbf{y}))(\mathbf{r}-\mathbf{y})}{|\mathbf{r}-\mathbf{y}|^5} - \frac{\mathbf{m}}{|\mathbf{r}-\mathbf{y}|^3} \tag{3.5}$$

where **B** is the magnetic field, **m** is the dipole moment, **r** is the measurement location and **y** is the location of the dipole. It should be noted that since the MEG pickup coils are 9-10 mm in diameter (for CTF) and n for Elekta, integration across the pickup loop may be necessary when the dipole is close to the helmet surface. An insulated copper wire was chosen for the dipoles to allow for small coil windings.

Cable construction

The cable that connects the dipole to the driving microcontroller should not be a generator of magnetic fields. The best choice for this would be the use of twisted pair cables. Shielded coax cables can show appreciable leakage due to the sensitivity of the MEG. The small amount of straight wire exposed along the length of the coil axis is sufficiently small to be negligible. The dipole is constructed with a continuous wire with the helical loop in the middle. It is also possible to solder the cable to the coil, though there may be potential for small leakage in unwanted magnetic field from the solder joints. We used a continuous wire to construct the coil and cable rather than solder the coil to a cable.

Coordinate definition

Because the phantom can be placed in arbitrary locations in the MEG helmet, it is necessary to define a local coordinate system rigidly connected to the phantom dipole. Three fiducial locations are typically used for human data collections and these same locations will be defined for the phantom to create a local "head" coordinate system. As with the subject fiducials for a CTF head coordinate system, the nasion will be placed on the positive x-axis, left ear on the positive y-axis and right ear on the negative y-axis. Note that Elekta uses positive y for nasion. To ensure that the coordinate system is defined the same each time, magnetic dipoles will also be rigidly placed at these points and we will energize each coil separately and collect our own data for these coils. Thus the system specific head localization will not be used to locate the phantom fiducials. We will however collect some data with the site-specific head localization system for comparison.

We wound a series of dipoles with twisted pair cables about 3-4 m long. The long cable allows us to feed the cable through an opening in the MSR. Hence, the current driver could be placed outside the MSR, which is a source of magnetic interference.

We used the CTF magnetic dipole phantom stand to attach the dipoles. This stand has a fixed head coordinate system created with holes drilled at 90-degree intervals around a circular disk. Fiducial head localization coils are screwed to three of these locations to form the head coordinate system. The dipole locations are digitized using a Polhemus device relative to these fiducial locations. The CTF magnetic phantom stand has it's own single dipole (1 mm by 2 mm using gauge wire) rigidly fixed at a location of 0, 0, 50 mm relative to the head coordinate system. This magnetic dipole was also used in the collections described in this section. For the site-to-site collections, it was decided that we would use this dipole instead of our hand made ones because it had a well defined and fixed location.

To convert the CTF magnetic phantom for use with our microcontroller, the construction of a custom cable was required. The CTF magnetic phantom terminates in a 1-pin Lemo, which connects directly to the CTF head localization box, which has the female Lemo end. The connector was soldered to a 4 m length of twisted pair copper wire. The other end was left open for input for the microcontroller.

Microcontroller Construction

The microcontroller was constructed by Jeff Lui and described in his thesis [[49]]. Figure 3.10 shows the photograph of the microcontroller and figure 3.11 is a diagram of the hardware configuration. This microcontroller featured an integrated circuit using ADC's and potentiometers. The electronics was programmed to generate a sinusoidal wave of specified frequency and amplitude. An adaptor was created to permit the device to be used in both 120 and 220 V locations. The total voltage was 3.3 V peak to peak. We measured this using an oscilloscope as well I connected the circuit to an analog-to-digital converter (ADC) channel set to read voltage in the CTF hardware. The peak to peak reported was 3.29 V from the ADC channel.

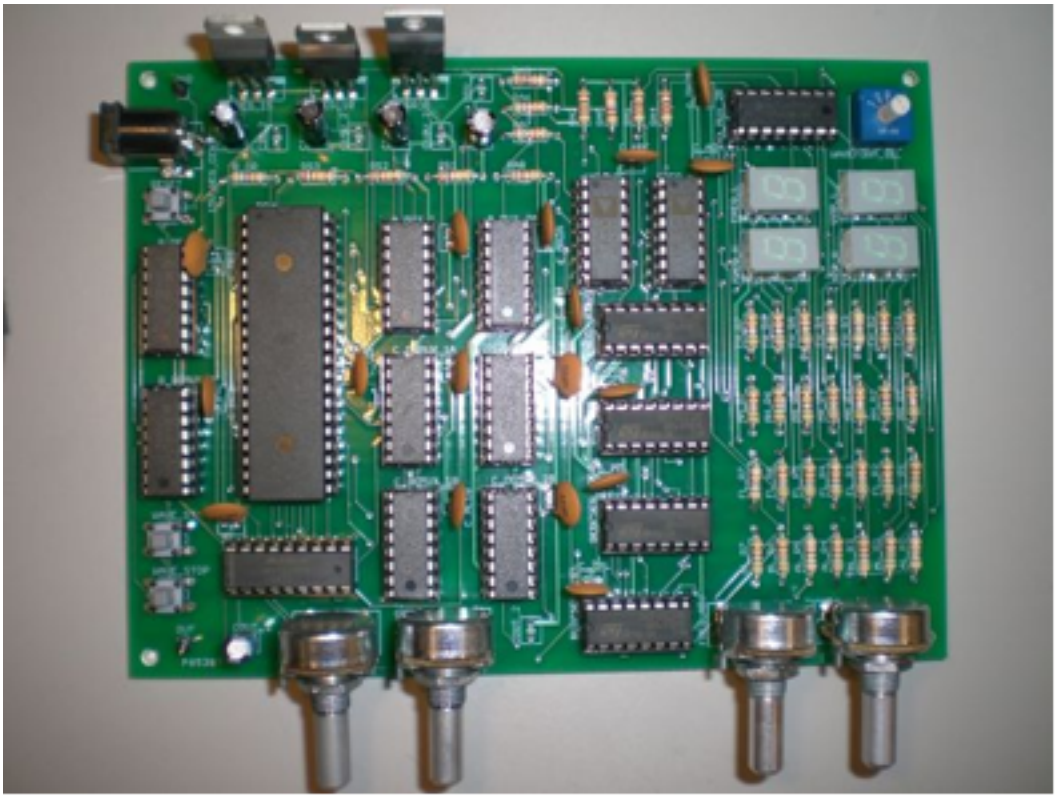

Figure 3.10: Single dipole microcontroller used to collect the data at DSRF, MNI and Aston.

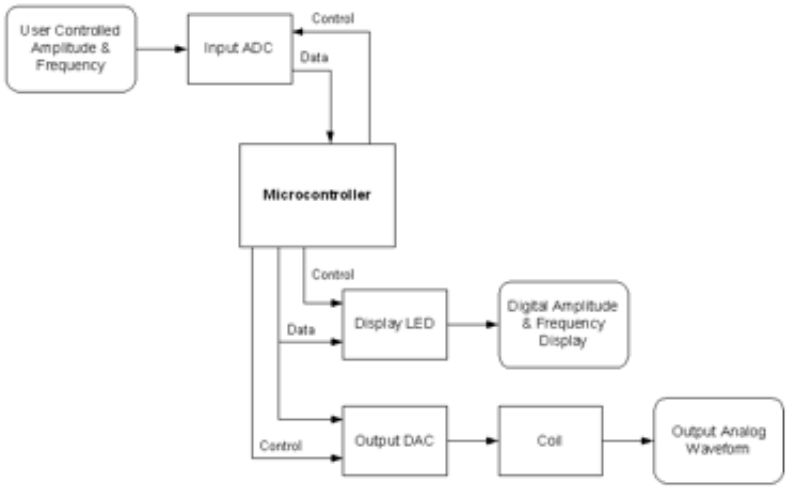

Figure 3.11: Hardware configuration of the single dipole microcontroller

Data Collection - Component Testing

The testing of the microcontroller and dipoles were carried out at the CTF MEG lab located at the Down Syndrome Research Foundation, Burnaby, British Columbia, Canada. This system contains 151 axial gradiometers, and 32 reference magnetometer/gradiometers. The system is housed within a Vacuumshmeltz magnetically shielded room.

All components were tested for magnetic contamination. The microcontroller components (off) were not magnetic placed 1.5 m from the MEG helmet on the floor of the MSR. However, when powered on, the microcontroller could be seen as a source of magnetic noise from the MEG. The microcontroller was relocated to outside the MSR. A 3 m twisted pair cable was fed through a hole in the MSR to connect the phantom to the microcontroller. A series of data was collected using the CTF phantom and the microcontroller. Each phantom dipole as well as the CTF magnetic phantom was collected in position within the helmet with all components off. No magnetic contamination was detected above the empty room noise level.

Each dipole including the CTF magnetic phantom dipole was then connected to the manufacturer- specific (CTF) current driver via the spare coil connector on the head localization box. The CTF hardware can be configured to generate a sinusoidal current at different amplitudes and frequencies. Each dipole was rigidly mounted onto the CTF magnetic

phantom stand. Head coils were connected to the standard locations on the CTF magnetic phantom to create the head coordinate system for the dipoles. Each dipole was collected at different locations and orientations, and the locations digitized using a Polhmeus relative to head coordinates. A rough estimate of the dipole orientation was determined by digitizing the locations of the two magnetic poles on the dipole. Collection parameters ranged from 600 to 1200 samples per second. No filters were applied except for a hard coded hardware antialiasing filter at 1/4 sample rate. Finally each dipole, including the CTF magnetic phantom was connected individually to the microcontroller and the collections were repeated using the microcontroller.

Data Collection - Microcontroller Calibration

Using the CTF phantom, the microcontroller's voltage and current output was tested. The voltage output from the oscilloscope reading was 3.29 volts peak to peak. The CTF hardware also reported the same voltage with the microcontroller connected to the ADC voltage input port and the data collected. The microcontroller is set with a 25 Hz low pass filter. This can be seen in the fft of the voltage data. As well the microcontroller has a setting of 7 Hz sinusoidal. This too was confirmed from the current, MEG signal and voltage recordings.

The amplitude control on the microcontroller is not linear, a series of recordings were collected to determine the nature of the amplitude control. It was determined that the control would be set to nearly maximum and a resistor would be added to control the final current level. A 500 ohm resistor was selected for the CTF phantom. This was soldered permanently to the twisted pair cable. However the head localization coils have dipole moments several orders of magnitude larger. Although a larger resistor was not necessary the magnetic fields recorded were of the order of nano-Tesla. An optional resistor may be added to the circuit should a system's flux transformers saturate under these field values. The value of the magnetic phantom dipole must not change but the head coils may change because only the location of the coils are used for head localization. These values will not change until completion of all collections. To see if these values did not change in time, we collected phantom data over several days and the results were compared.

Site Collections

Since we were interested in cross site collections, it was important to consider a collection design that would be suitable for the different systems we would encounter. CTF systems utilize axial gradiometers with a 32-channel reference array approximately 25 cm from the sensor array. The references comprise both magnetometers and gradiometers. The Elekta 306 system contains 102 sensor sites with two orthogonal planar gradiometers and one orthogonal magnetometer. Each system has it's own method for coordinate definition. To standardize the collections, the coordinate definition (head localization) would be done using our microcontroller and the system specific head localization would be collected for comparison purposes only. CTF head coils would be used for head localization regardless of which system we would use to collect the data. These coils are energized at very large amplitudes. The default values used by CTF are meant to be used with only the reference sensors only. Since some devices would not have references, the head coil data would have to collected using the sensors only and localized using standard dipole fit routines (with the magnetic dipole forward model).

The microcontroller could only be connected to one dipole at a time. A series of 4 collections were necessary to collect the data for a complete phantom. The head coils were attached in advance to the magnetic phantom and the phantom was placed centrally within the helmet region of the MEG system. The four cables that connected to each head coil and phantom dipole were carefully placed on the floor of the MSR and connected one at a time to the microcontroller cable. This cable lead through a hole in the MSR to the microcontroller electronics outside the MSR. The microcontroller was plugged to the local power mains using an appropriate 15 V AC to DC adapter.

First the microcontroller was connected to the phantom dipole with only the soldered resistor and a 60 second collection was done. Then each of the head coils was connected with the necessary additional resistor if needed one at a time also for 60-seconds. The sample rate was set to 1200 Hz or whatever rate was closest to this value for the specific system. Once the microcontroller head localization data was collected, the head coils were replaced by the system's head. These coils were placed at the same location as the microcontroller head coils. The microcontroller was connected to the phantom dipole. The system specific head coils were collected and localized using the system's head positioning algorithms and

then the microcontroller was turned on, and a phantom was collected.

In addition to the phantom data, empty room noise was also collected before the phantom collections. Table 3.1 lists the general collection flow and tables 3.2, 3.3, 3.4 list the collection parameters.

Table 3.1: Datasets Collected at Each Site

Run	Description
1	Noise 1200 Hz
2	Noise 300 Hz
3	Phantom with CTF head coils
4	Nasion coil collection (adjust current with additional resistor)
5	Le coil collection (use additional resistor)
6	Re coil collection (use additional resistor)
7	Phantom with site specific head coils

Table 3.2: Phantom and Head Coils Collection Parameters

Parameter	Description
Low Pass Filter	None (except for the hardcoded anti-aliasing filter)
High Pass Filter	None
Notch Filter	None
Sample Rate	1200 Hz sample rate or something close to this
Time	60 seconds
Number of Trials	1

3.1.4 Data Analysis

Because harmonics of the driving frequency could be clearly seen in the frequency plots, some of the lower harmonics were notched and the data was low pass filtered at 14 hz. The empty room noise data was analysed using stacked fft's and bad channels were removed from analysis. 3rd order gradient correction was applied to the CTF collected data and SSS

Table 3.3: Noise Collection Parameters 1200 Hz

Parameter	Description
Low Pass Filter	None (except for the hardcoded anti-aliasing filter)
High Pass Filter	None
Notch Filter	None
Sample Rate	1200 Hz or something close to this
Time	2048 samples
Number of Trials	50

Table 3.4: Noise Collection Parameters 300 Hz

Parameter	Description
Low Pass Filter	None (except for the hardcoded anti-aliasing filter)
High Pass Filter	None
Notch Filter	None
Sample Rate	300 Hz or something close to this
Time	10 seconds
Number of Trials	10

maxfilter was applied to the Elekta data. The data was then converted to CTF format so that the same analysis tools could be used to fit the data. The Elekta coordinate system was transformed to CTF coordinate system during the data conversion process. Single dipole fits using a dipole fit program that was adjusted for a point magnetic dipole model were performed on the data. The head coils were localized relative to device coordinates and the coordinate frame formed from these points. The phantom dipole was then fit using both the data using the device head coils and our microcontroller collected head coils.

3.1.5 Results

DSRF Data

The first set of data was collected at the MEG laboratory at the Down Syndrome Research Foundation in Burnaby BC, Canada. Testing of the phantom and adjustment of parameters

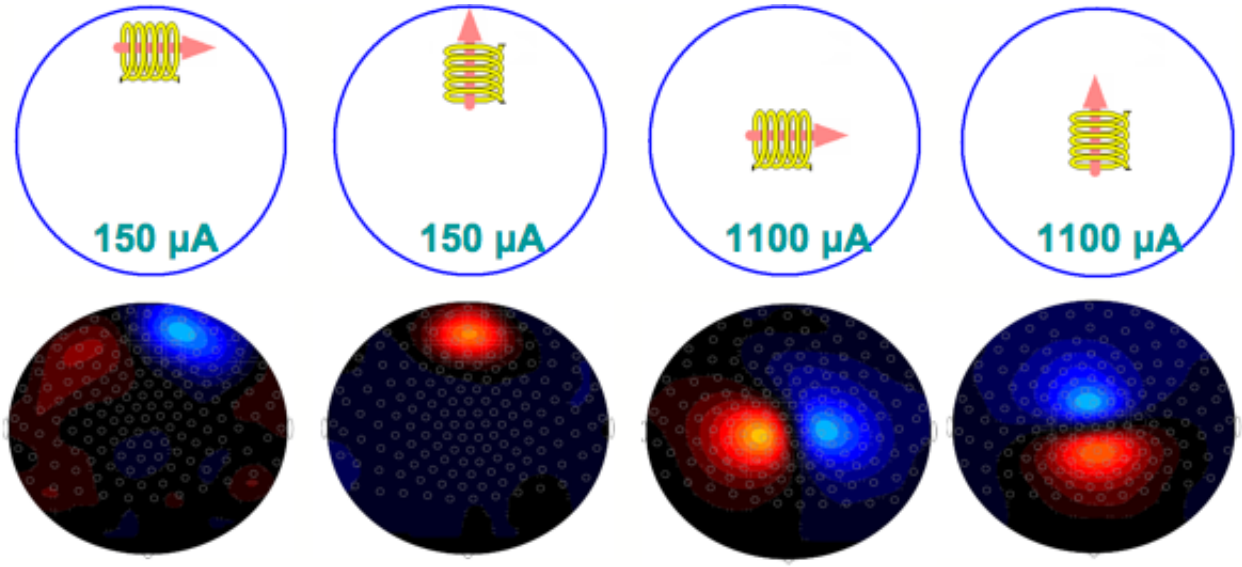

Figure 3.12: Single dipole phantom topographical maps for different dipole orientations.

were done at this site before the phantom was sent to other sites. The DSRF MEG is a CTF system with 151 axial gradiometer channels housed in a 4 layer mu-metal shielded room. Figure 3.12 shows the results of single dipole collections of a magnetic dipole coil at different locations and orientations. The results, together with their dipole fits confirmed that the modelling software and the microcontroller produced the desired currents and frequencies. Goodness of fit were above 98% and the positions agreed well with Polhemus results.

Stacked fft of the empty room noise showed several bad channels which were removed from further analysis. Figure 3.13 shows the topological maps during the collection of each head localization coil and figure 3.14 the topological map of the phantom collection.

McGill Data

The next set of data was collected at the Montreal Neurological Institute (MNI) at McGill University, Montreal, Canada. This centre has a 275 CTF axial gradiometer system also in a shielded room. Bad channels were removed. Figure **??** show the topological maps of the individual head coils and figure 3.16 show the phantom collection.

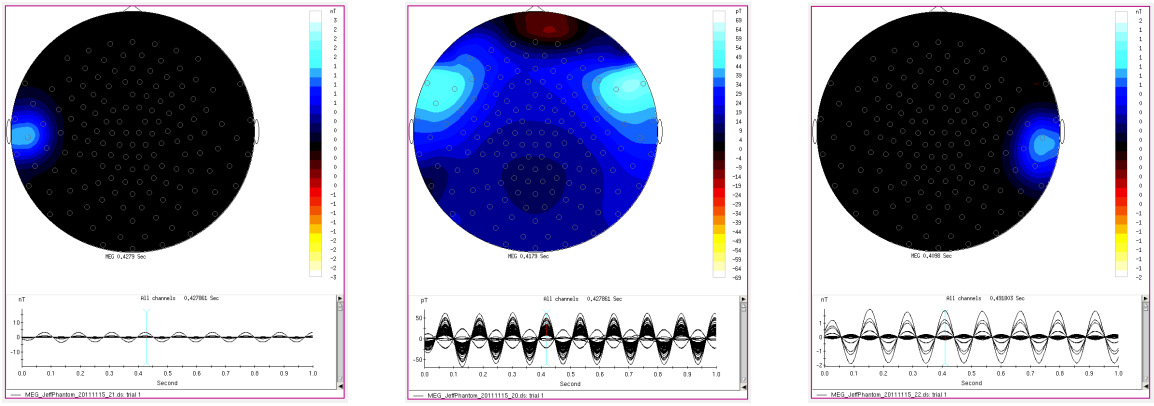

(a) LE (b) NA (c) RE

Figure 3.13: The magnetic field patterns from each of the three head localization coils collected at DSRF. The latency is selected at the peak of the sinusoidal signal.

Aston Data

At the time of the phantom collections, Aston University's MEG centre had two MEG systems in operation simultaneously, an older 275 channel CTF axial gradiometer system and a new 306 channel Elekta planar/magnetometer system. Maxshield was active for the Elekta collections. The data was pre-processed with SSS maxfilter. The CTF data was collected with a 40 Hz low pass filter and the data was processed with 3rd gradient correction.

Dipole Fit results

The table 3.5 shows the dipole moments from the phantom dipole fits for each MEG device. The moment differs at most by 0.5, a 4% difference. It is interesting to note that the two devices at Aston differ by about the same amount as the device at MNI compared to DSRF. There does not seem to be a consistent moment emerging for a specific machine manufacturer although there are too few data points at present to draw any firm conclusions. Between these machines at least, there are no dramatic deviations in moment.

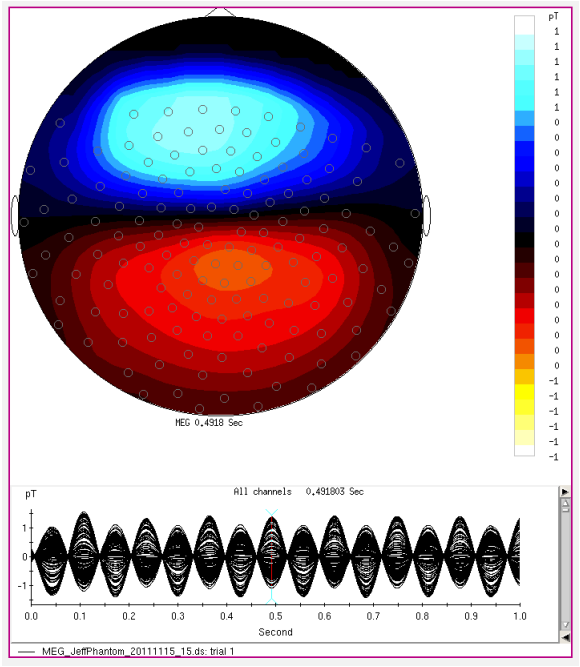

Figure 3.14: The magnetic field pattern of the phantom collected at DSRF. The latency is selected at the peak of the sinusoidal signal.

3.1.6 Discussion

There has yet to be declared a gold standard ground truth for MEG. For testing differences between devices, it seems a phantom with it's own current driver could be a potential candidate. Such a phantom need only be able to produce it's own consistent current to provide a standard, reproducible magnetic field that can be tested at any laboratory. Our phantom and microcontroller has proven to be a valuable contribution towards the goal of a device ground truth for MEG. The resulting data showed there were clear differences between devices even operating at the same laboratory site and that while these deviations were small they were not necessarily insignificant. Indeed it seems reasonable to consider doing such measurements on a routine basis before embarking on cross-site studies.

Our phantom and microcontroller data collections using 4 different MEG machines has demonstrated that the device was stable, portable and efficient. The data collection was performed in under an hour for each machine with the collection stream and parameters well tolerated by both CTF and Elekta machines. The device itself was sufficiently robust

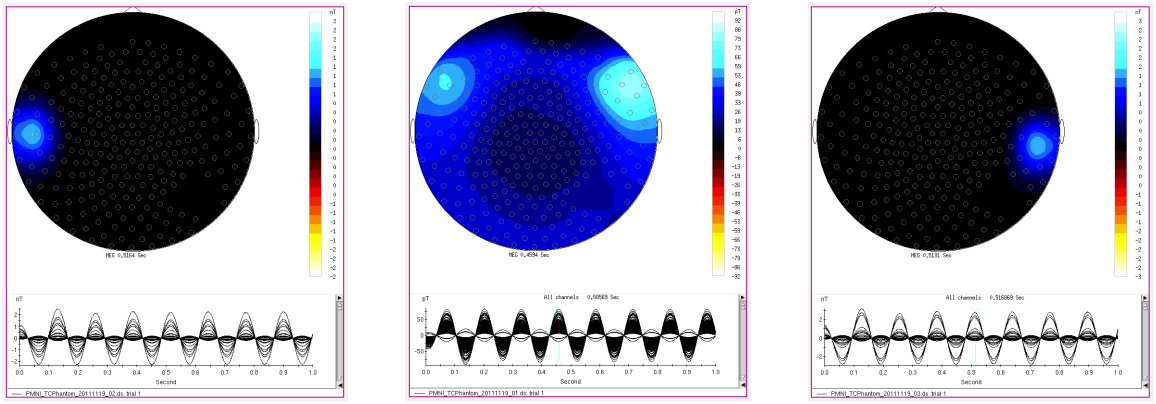

(a) LE (b) NA (c) RE

Figure 3.15: The magnetic field patterns from each of the three head localization coils collected at MNI. The latency is selected at the peak of the sinusoidal signal.

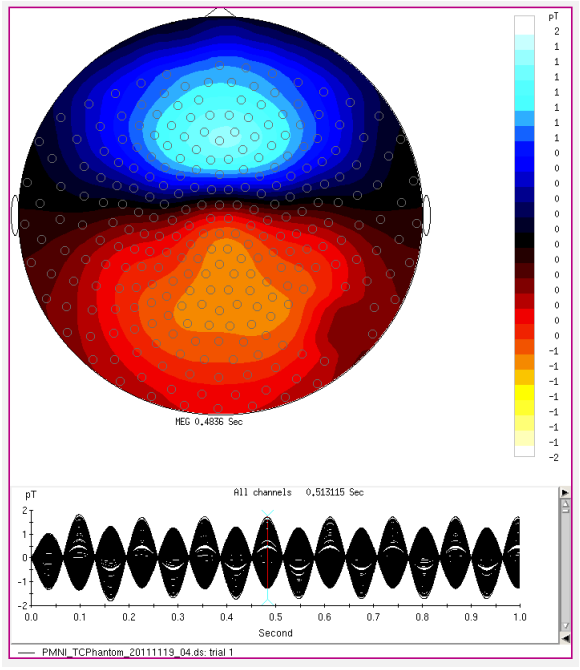

Figure 3.16: The magnetic field pattern of the phantom collected at MNI. The latency is selected at the peak of the sinusoidal signal.

to be transported in person or by mail to the different sites

Table 3.5: Dipole Moments

Site	System	Moment (nAm^2)
DSRF	CTF	12.79 ± 0.01
MNI	CTF	13.2 ± 0.01
Aston	CTF	13.32 ± 0.01
Aston	Elekta	12.71 ± 0.01

Improvements could also be made to the phantom and microcontroller. For example, fixed dipoles could be mounted directly on the phantom permanently to represent the head coils. This would eliminate one potential source of error. The microcontroller could be simplified to only generate a constant current and frequency rather than being variable. This would eliminate the possibility of inadvertently changing the settings. A better low pass filter on the microcontroller would help eliminate some of the observed harmonics in the data. Although a triangular dipole phantom might be an interesting next step, the analysis of the magnetic dipole phantom undertaken in this study suggests that the helical coil design, being coordinate free, is a much more forgiving to deviations in head localization results. Only the coil position would shift leaving the moment unaffected. The triangular dipole would require a well defined coordinate system. The appeal however to use current dipole models rather than an adjusted magnetic dipole model is very compelling however.

3.1.7 Conclusions

We collected data using a single magnetic dipole phantom with it's own microcontroller to drive the phantom dipole. Data from 4 different MEG machines has demonstrated that the device is well suited to be a potential device ground truth for MEG. Improvement on the design of the phantom and microcontroller would further improve it's stability enabling a long term solution for cross-site comparisons of MEG data.

3.2 A Scanner Independent Approach to Modeling Neural Activity with a Hardware Phantom

[4]

3.2.1 Abstract

We describe the construction of a prototype hardware phantom that demonstrates proof of principle towards the construction of a large dipole array phantom. The prototype focuses on answering questions regarding choice of dipole construction. It consists of 8 fixed magnetic dipoles mounted on a plastic stand. The dipoles are energized using the MEG system's electronics or a prototype microcontroller. Data were collected using pairs of active dipoles at different separations representing different physiological processes and compared against simulated data. These data illustrate the role and value of including a hardware model that is intrinsically scanner independent in the analysis process and demonstrates in principle the feasibility to construct a phantom with many more sources mimicking cortical and sub-cortical levels for validating source localization procedures.

3.2.2 Introduction

With increasingly ambitious modeling and functional mapping techniques in MEG, it has become vital to construct test data with known ground truths that will provide sufficient challenge to test the effectiveness of these new algorithms. Algorithm verification has been accomplished using three kinds of data: data acquired from human subjects, simulated data computed from forward models and phantom data acquired using hardware devices constructed to emit magnetic fields.

Data collected from subjects have the advantage of including system and environmental variability in addition to obtaining magnetic field patterns from actual neurophysiological processes without any assumptions about the magnetic field generators. However, ground

[4] A version of this section has been published. Cheung T, Wong J, Parameswaran A, Babul A, Beg F, Kavanagh KL, Jirasek A, and Ribary U, A Scanner Independent Approach to Modeling Neural Activity with a Hardware Phantom. In Kakigi R, Yokosawa K, Kuriki S, (Eds.), Biomagnetism: Interdisiplinary Research and Exploration (pp. 89-91). Hokkaido: Hokkaido University Press, 2008 [11]

truth of the subject is not well defined. Functional MRI or other functional mapping modalities as ground truth is still in question due to lack of direct connection between hemodynamic and electrodynamic processes.

Simulations have the advantage of a known ground truth with the potential to construct highly complex models but it is limited by the choice of forward equations used to compute the data. Simulations can at best only approximate environmental and system variability and hence cannot be used to evaluate system performance. While it could be argued that for model verification, exactness in representing system and environmental variability are less important factors, it nevertheless introduces a level of artificiality into the data that phantoms avoid.

Phantoms have the advantage of including real system and environmental conditions and an absolutely known ground truth. Phantoms have the potential to provide a gold standard for evaluating model performance under real situations and provide a portable model for cross site comparisons. However, because it is a hardware device, increasing the complexity of the phantom such as adding more sources becomes an engineering challenge.

Each of the three types of data serves important purposes in the verification of any source model technique. However, in terms of seeking a known ground truth, phantoms provide the best compromise between the real and the artificial.

All MEG phantoms operate on the same basic principles. They are magnetic field generators that emit time varying signals detectable by an MEG scanner. The construction of a phantom parallels the source modeling techniques they are used to verify. Source construction and the choice to include a conducting medium, its shape and choice of media comprise the components that are important to verification of the forward problem. The placement and number of sources are important to verification of the inverse problem. Much effort has been put into constructing accurate phantoms for forward model verification while inverse problem verification has mainly been the domain of simulated data due to the limitations in constructing phantoms with large number of sources.

The magnetic field generators for phantoms are typically point dipoles. Extension to distributed sources could be accomplished by using dipole groupings. To verify forward equations for neurophysiological events, current dipoles imbedded in a conducting media such as saline or conductive gelatin with spherical [3] or skull-shaped boundaries ([47], [75], [2]) best represent neuronal activity. Using real conductors by combining human data

with known sources have also been studied through stimulation of electrical implants in human patients and within cadaver heads ([3], [16]). Ilmoniemi [38] proposed a method to construct a conductor free phantom using isosceles triangular magnetic dipoles with a small base that is nearly equivalent mathematically to a current dipole in a spherical conductor [80].

The use of current dipoles in conducting media for phantoms has its limitations. Most notably, as the number of sources increases, challenges keeping the individual dipoles isolated and behaving as point sources becomes more difficult. While Ilmoniemi's approach would readily allow for increase in dipole number because there is no conducting medium, the needed geometry required to accomplish the cancellation of the radial fields potentially limits the placement of the dipoles and therefore lessens the advantage of being able to use current dipole forward equations for this type of phantom.

Magnetic dipoles of general construction do not have these limitations. Magnetic dipoles operate in air rather than in a conducting medium. They are easier to construct, can be placed arbitrarily and pose less difficulty in activating simultaneously when the numbers are increased. Micromachining techniques exist that could allow for a significant increase in the number of dipoles included in a phantom. While magnetic dipoles have been used as fiducial markers for head localization and are used as fixed dipoles in phantoms built specifically to verify system performance, they have not been used in phantoms for algorithm verification because they do not represent a realistic forward model for neural activity. This has mainly been because both forward and inverse problem verifications have traditionally been coupled in the phantoms that have been constructed. It is however possible to decouple the two processes and consider the construction of a magnetic dipole phantom that is used for the purposes of inverse problem verification only.

Building on the experience of the phantoms that have been constructed by Leahy, Mosher, Spencer [75], McVeigh [54] and others, we propose the construction of a large array dipole phantom that potentially could be made of magnetic dipoles. We explore this possibility further with the construction and measurement of a prototype magnetic dipole phantom.

3.2.3 Methods

Phantom Construction

Our prototype focuses on magnetic field generators from point sources. To simplify the problem, our prototype focuses on answering questions regarding the inverse problem rather than both forward and inverse problems. By separating these two processes, we have the advantage of being able to use more manageable magnetic source generators and eliminate the need for a conducting medium for our device. We have chosen to use magnetic dipoles, small coils that produce magnetic fields for this purpose. These dipoles have a well characterized magnetic field equation which when substituted for the current dipole forward equation allow for accurate localization of these sources. Therefore, this phantom cannot be used for forward model verification. However, inverse problem verification can be explored without introduction of further variables caused by conductor model inaccuracies. The dipoles are mounted on a plastic stand upon which 3 fiducial markers for nasion, left ear and right ear are also mounted forming a right handed coordinate system for the measurements. Using the same coordinate system, a Polhemus digitizer is used to determine the locations of each dipole.

Dipole Construction

Two layer coil wound magnetic dipoles with 8 windings per layer were constructed using 32 gauge magnet wire. A small plastic spool 1 mm in diameter was used to wind the coils. With two windings, the leads start and end at the same point minimizing unwanted magnetic field contamination from lead effects that were not cancelled. The leads were twisted to a length of 3 meters. Each dipole was hand wound but since moments are part of the inversion process, the slight variabilities in the dipoles are not relevant.

Phantom Data Collection

The CTF MEG system housed at the Down Syndrome Research Foundation MEG Laboratory was used to collect the data. The system consists of 151 radial gradiometer sensors within a magnetically shielded room. The data was collected at 600 samples per second with a 150 Hz low pass anti-aliasing filter and software third gradient balancing. Both the

CTF hardware and a microcontroller constructed for the phantom was used to drive the dipoles. Dipole moments were varied to simulate different signal to noise ratios. 100 trials of data one second long were collected for each run. A 5 or 7 Hz sinusoidal or 1 Hz square wave was used to drive each dipole. The onset of each trial was triggered by monitoring the current output from the electronics or from a sync pulse generated from the microcontroller. Averaged data using all or a subset of trials was created to represent different signal to noise conditions. Dipoles were energized individually and in pairs.

Pairs of dipoles 11.6 mm apart and 67.0 mm apart were simultaneously and individually collected. The dipole pairs were energized simultaneously with synchronous currents. As a confirmation of localization accuracy for the specific MEG system used to collect the data, the CTF magnetic dipole phantom, which contains a single fixed magnetic dipole, was also collected.

Simulations

Simulations were carried out using a current dipole forward model. Added noise was assumed to be white and was selected to match signal to noise ratios similar to that encountered in the collected phantom data.

Magnetic Dipole Fits

By substituting the magnetic field equation of a magnetic dipole in place of the current dipole equation, source localization of the magnetic dipole phantom can be achieved using the same inverse algorithms. The magnetic field equation for a magnetic dipole is given by the relation:

$$\mathbf{B}(\mathbf{r}) = \frac{\mu_0}{4\pi}\frac{3\mathbf{n}(\mathbf{n}\cdot\mathbf{m})-\mathbf{m}}{r^3} \tag{3.6}$$

where $\mathbf{r}$ is the vector from the dipole to the measurement point, $\mathbf{n}$ is the corresponding unit vector, $\mathbf{m}$ is the dipole moment and μ_0 is the permeability of free space. The dipole fits were performed at a single time point at the peak of signal activity. For the dipole pairs, the dipoles were energized synchronously. Therefore, both dipoles peak at the same time point. The resulting fits were compared to the Polhemus measurements and a resulting error is computed between the Polhemus location and the fit location.

3.2.4 Results

The preliminary results examine only the localizations with the highest signal to noise reflecting near ideal conditions. Polhemus digitized locations on average had errors of 1.2 mm. Preliminary source localization of individual magnetic dipoles agreed with Polhemus measurements to within 2.3 $\pm$ 1.2 mm and 99.99% goodness of fit. Source localization of simulated single dipoles were accurate to 0.5 mm and 99.95% goodness of fit and the source localization of the CTF phantom was accurate to 1.1 $\pm$ 0.5 mm. Source localization errors of the phantom dipole pairs were accurate to 2.3 mm $\pm$ 1.2 mm and 99.84% goodness of fit whereas the simulated data were accurate to 0.4 mm error and 99.71% goodness of fit.

3.2.5 Discussion

The use of a phantom is important for validation of detailed distributed source analysis and correlation procedures across 3D-space, frequency and time. Such a hardware phantom will also be important for testing specific neurophysiological models underlying sensory and cognitive human brain functions in order to match and explain real MEG data. By substituting a magnetic dipole for a current dipole, the questions of inverse problem accuracy can be separated from the question of forward model accuracy. Without the need to include a conductor model, magnetic dipoles could be used effectively to address questions of resolvability of nearby sources as well as explore correlated and uncorrelated signals. The preliminary data collection using our prototype magnetic dipole phantom demonstrates that the inverse algorithm used for current dipole fits can be used without modification to fit magnetic dipoles. Only the forward equation needs to be changed. In principle other inversion techniques may also be adaptable with little to no modification for magnetic dipoles. Without coupling issues involving forward model accuracy, it is possible to study the effectiveness of the inverse problem under real system and environmental situations. Our single dipole phantom results agreed with the CTF phantom results to within the error caused by the variability in the Polhemus measurements. The dipole fit results from the magnetic dipoles illustrate that even under near ideal signal to noise conditions, real system variation prevents localization of the dipoles better than a few millimeters. Comparable simulated data under similar noise conditions but using idealized sensor locations resulted in more exact dipole fits that do not reflect real system variability. These results illustrate

the difference between localizations using data simulated from idealized sensors compared to phantom data collected from a real system.

3.2.6 Conclusion

There are still many challenges yet to be resolved before a full ground truth for MEG can be realized. Our phantom serves as a prototype towards the creation of a phantom for the purposes of providing known, characterized signals for MEG measurements in order to validate many complex analysis algorithms and to test neurophysiological models explaining the circuitry of underlying normal and altered cognitive brain functions. This work lays the foundations for the construction of a more complex phantom using micromachining techniques.

3.3 Conclusions and Future Work

This chapter describes the development of two phantoms. A single dipole phantom was developed for the purpose of a device ground truth for cross-site data comparisons. The second was the development of a multiple dipole phantom to test inverse problem solutions. Both phantoms were made from magnetic dipoles which were deemed to be the most reproducible and portable despite the problem that this poses to the forward magnetic field modelling. In the case of a device ground truth, the magnetic dipole is the best choice because it can be localized in free space without the real need for head localization. In the case of a ground truth for source modelling, the magnetic dipole does pose some problems as only half the source modelling problem can be addressed with these phantoms. While it can be argued the more complicated half lies in the inverse solution and a real hardware model which accounts for more real environmental variabilities is still better than simulations, the need to incorporate both together to test existing software is not realized with this design. The question once again falls to the question of dipole design and perhaps the next step should be a move towards a triangular dipole phantom. In terms of improvements to the microcontroller design - more dipoles and the ability to program more complicated signals would be helpful. Studying coherence and correlation using phantom dipoles could be a useful future exercise towards our goal of building a ground truth for MEG.

Chapter 4

Face-selectivity of the M170

4.1 MEG correlates of static and dynamic facial expressions in typically developing children

[1]

4.1.1 Abstract

Dynamic facial expressions represent one of the most common forms of nonverbal human communication. While neural substrates have been described for adults using functional magnetic resonance imaging (fMRI) ([71]) little is known about how children process dynamic facial expressions. Further, little is known about the temporal nature of these neural substrates. We utilized the spatial and temporal qualities of magnetoencephalography (MEG) to compare the neural activity between dynamic and static facial presentations for one of the developmental age groupings described by Batty and Taylor [4]. Four typically developing girls (mean age = 10 years) volunteered for the study. Static and dynamic emotional faces and non facial images (that of a static or moving fan) were presented to each subject. To keep the subject's attention, the subject was asked to identify if the images

[1] A version of this section was presented in the form of a poster at SFN 2007. Cheung, T., Virji-Babul, N. MEG correlates of static and dynamic facial expressions in typically developing children. In Society for Neuroscience Conference San Diego (2007).

were male, female or neither by pressing one of three buttons using the subject's dominant hand. Expressions of happy, sad or neutral were presented for the same length of time using the same actors in both the dynamic and static conditions. The dynamic images began with a neutral face changing to one of the 3 emotions which is sustained till the end of the video. The static images showed the emotion at image onset. Separate time locked averages synched to the onset of image presentation and grouping all emotions together were separately generated for the dynamic and static conditions. The data were analyzed in the 0.1 to 40 Hz bandwidth in both sensor and source space. Channel morphology was similar in both the dynamic and static conditions. Peaks in the MEG channels were observed for the M100 component which localizes to the occipital visual region and for the M170 component which localizes to the right temporal region. In addition, a peak at mean = 300 ms was observed in the central parietal region. Although individual amplitudes varied from subject to subject, the M170 amplitude and the component at 300 ms were larger for the dynamic compared to the static condition. These results suggest that dynamic images produce an enhanced effect over presentation of static images consistent with Sato's fMRI study on adults ([71]). This provides a possible alternate stimulus strategy for presentation of facial expressions. Studies of special populations might benefit from the additional temporal information provided from dynamic over static facial expressions.

4.1.2 Introduction

Dynamic facial expressions represent one of the most common forms of nonverbal human communication. Neural substrates have been described for adults using fMRI ([71]). Using Magnetoencephalography (MEG), we examined how children process dynamic facial expressions.

4.1.3 Materials and Methods

Subjects

Four right handed volunteers (girls, mean=10 years) with normal vision participated in the study.

Stimuli

Static and dynamic faces and non facial images (fan) were presented using the Presentation stimlus program. Faces depicted emotions of happy, sad or neutral. 96 trials were collected with 50% dynamic, 50% static; 90% faces and 10% non-faces

Data Recording

Subjects viewed visual stimulus while their magnetic brain activity was collected using MEG. Subjects pressed one of three buttons (using dominant hand), to indicate male; female; neither. Three blocks of continuous data were collected with head localization between blocks. A sample rate of 600 Hz with a 150 Hz anti-aliasing filter and 3rd gradient noise correction (bandwidth 0-150 Hz) was used. The head shape was digitized using a Polhemus device.

Data Analysis

The continuous data was filtered with bandwidth 1 to 50 Hz. Trials (from -200 to 500 ms) were constructed for the dynamic and static conditions. Using all sensors, RMS for the dynamic and static conditions were constructed for each subject and then each condition was separately grand averaged. Using Event Related Synthetic Aperture Magnetometry, locations of peak power related to both conditions were identified for each individual subject. Grand averaged source waveforms at peak locations were constructed for each condition.

4.1.4 Results

Sensor Space Results

The grand RMS average revealed 4 latency regions. At the M100 (100 ms visual activity), there were no differences between Dynamic and static images. At the M170, Dynamic faces showed an increased amplitude compared to static faces. At 300 ms, Dynamic faces again showed an increase in amplitude compared to static faces.

Source Space Results

Peak Powers were observed in occipital and posterior temporal (3 right hemisphere dominant, 1 left hemisphere dominant) regions. We focused our time analysis on the right posterior temporal and occipital regions only. Figures 4.1 and 4.2 show the virtual channels. The occipital virtual channel shows little change. This agrees with the sensor space analysis of the M100 response. The right posterior temporal channel shows an increase in amplitude for dynamic compared to static faces at the M170 and a later latency effect is also evident. This also agrees with the rms sensor level analysis at the M170.

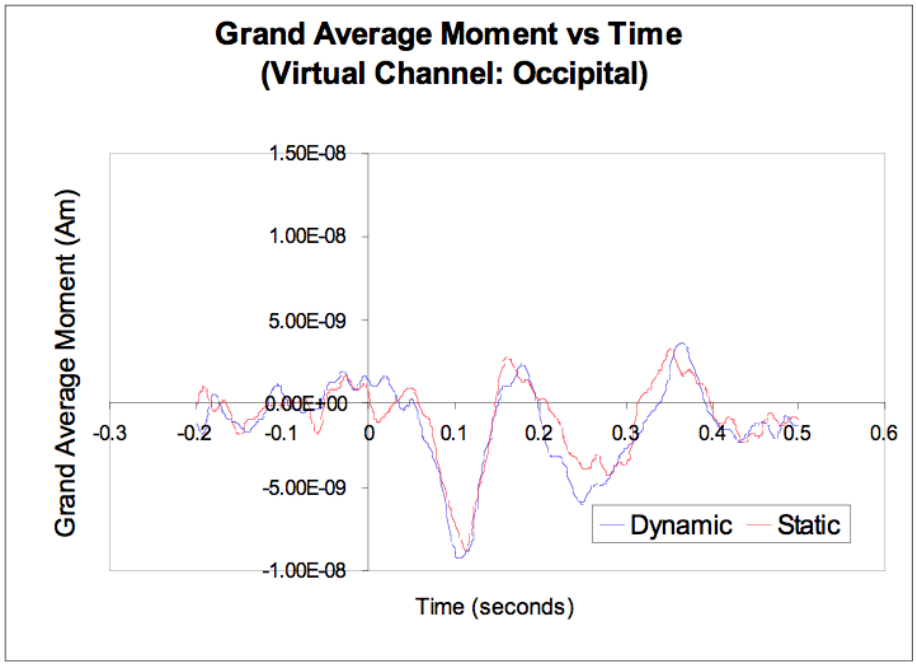

Figure 4.1: Occipital virtual channel for the dynamic face condition (blue) and the static face condition (red). There was no difference between the dynamic and static conditions. The peak at 100 ms is shown in this plot as a negative deflection. Polarity of dipole moments are arbitrary because it is dependent on the dipole orientation. This peak is consistent with the M100 response for visual evoked stimulus.

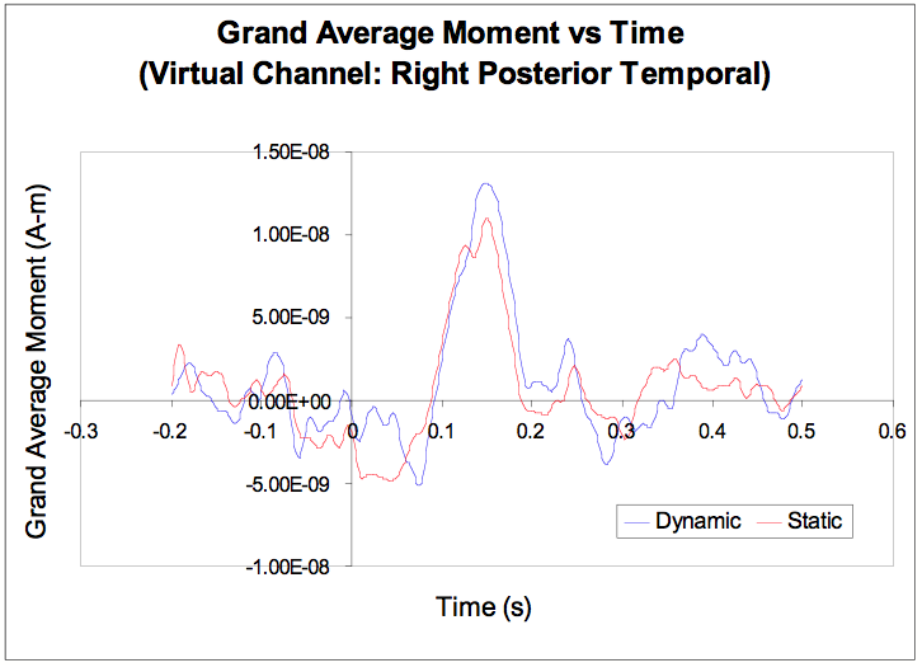

Figure 4.2: Right posterior temporal virtual channel for the dynamic face condition (blue) and the static face condition (red) There is a peak at around 150 ms which corresponds to the M170 response to faces. There is difference between the two conditions at this latency.

4.1.5 Conclusion

This first study on children (age 10) is in general agreement with Sato's [71]) study on adults. The dynamic condition shows higher activity than the static condition consistent with the more realistic scenario of viewing dynamic images. Temporal analysis of peak source activity further reveals latencies of higher amplitudes in the dynamic condition. Most notably, it appears that the higher activations in the dynamic condition emerges in the later latencies.

4.2 Magnetoencephalographic analysis of emotional face processing in children with Down syndrome: a Pilot Study

[2]

4.2.1 Abstract

Emotional face processing was studied using magnetoencephalography in five typically developing (TD) children and two children with Down syndrome (DS), between the ages of 10-12 years. MEG data were analyzed using event related SAM beamformer to create a volumetric description of the sensor data. Locations with the highest signal to noise ratio were identified for each individual subject and the average time distributions of virtual sensor signals from these locations were calculated. The neural response to facial images resulted in a large peak over occipital regions at 113 ms and a peak at 150 ms in the right temporal region in the TD group. In contrast, the first peak in the occipital regions was delayed by 15-45 ms in the participants with DS. The timing and pattern of the peak activity in the right temporal region for each participant with DS showed more variability. This pilot study suggests that viewing human faces activates similar neural regions in children with DS but with subtle differences in the pattern and timing of the activity. Further work with a larger group of children with DS is currently underway.

4.2.2 Introduction

The ability to process and interpret the actions and facial expressions of others is critical for effective social interactions. Infants orient to faces immediately after birth and by 4-9 months of age can begin to discriminate a number of facial expressions including happiness, anger, fear, sadness, and surprise ([6], [74]). This ability follows a long time course and continues to develop into adolescence ([4]). Numerous neuroimaging studies have shown

[2] A version of this section has been published. 6. Cheung, T., Virji-Babul, N. Magnetoencephalographic analysis of emotional face processing in children with Down syndrome: a Pilot Study. In Down Syndrome Quarterly, 10:18-21 (2008) [10]

that in adults, viewing human faces selectively activates regions of the ventral occipito-temporal cortex around fusiform gyrus, particularly in the right hemisphere ([78]). EEG and MEG studies show that activity in this area peaks at approximately 140-200 msec following stimulus onset. This response is commonly referred to as the N170 or M170 in MEG. In infants and children, face sensitive EEG responses are reportedly bilateral and of longer latency ([30], [79], [36]). MEG responses have been shown to be of the same latency in children and adults, however children tend to show a bilateral response ([46]).

Children with Down syndrome (DS), show a range of deficits in the perception of emotional cues in human movement ([82]) and in interpreting facial expressions ([43], [95]). There is preliminary data that suggests that adults with DS demonstrate an unusual reliance on processing the local features of the face with a preference for the mouth region (Kaiser et al, 2005). To date there have been no studies that have examined the underlying neural basis of facial and emotional processing in children with DS.

The purpose of this pilot study was to investigate the neural basis of emotional face processing in children with DS using magnetoencephalography (MEG). MEG is particularly suited for studies of children with developmental disabilities as it is a non-invasive technique. Most studies can be conducted with minimal external sensory and auditory disturbance so that children with hypersensitivity to noise and/or sensory stimulation can be tested without feeling anxious or fearful. MEG is sensitive to cortical activity and has a time resolution of milliseconds (ms) making it ideal to study cognitive processing. We investigated whether we could identify differences in the location and timing of neural activity evoked by viewing faces, between typically developing children and children with DS. Some of the results from the typically developing children have been reported previously ([9]).

4.2.3 Materials and Methods

Participants

Five typically developing (TD) children (all female; mean age 10 years) and two children with Down syndrome (1 male, 1 female; mean age 10 years) volunteered for the study. Informed consent was obtained from each participant and a parent/guardian after full explanation of the study. This study was approved both by the Simon Fraser University Research

Ethics Board and the Down Syndrome Research Foundation Research Ethics Committee. All participants were right handed with the exception of one female participant with DS and one typically developing female.

Stimuli

The children viewed static colour images (Figure 4.3a) and colour video clips (dynamic) (figure 4.3b) of the faces of young adults ([37]). Static and dynamic emotional expressions included happy, sad, angry and neutral. For both static and dynamic stimuli, a white dot was digitally added to the middle of the lower 15 pixels of each image (Figure 4.3). This dot was imbedded directly into the image or movie file starting from the first frame to the last frame of the image. During data collection, a photo diode was placed over this dot to determine precise timing of image onset.

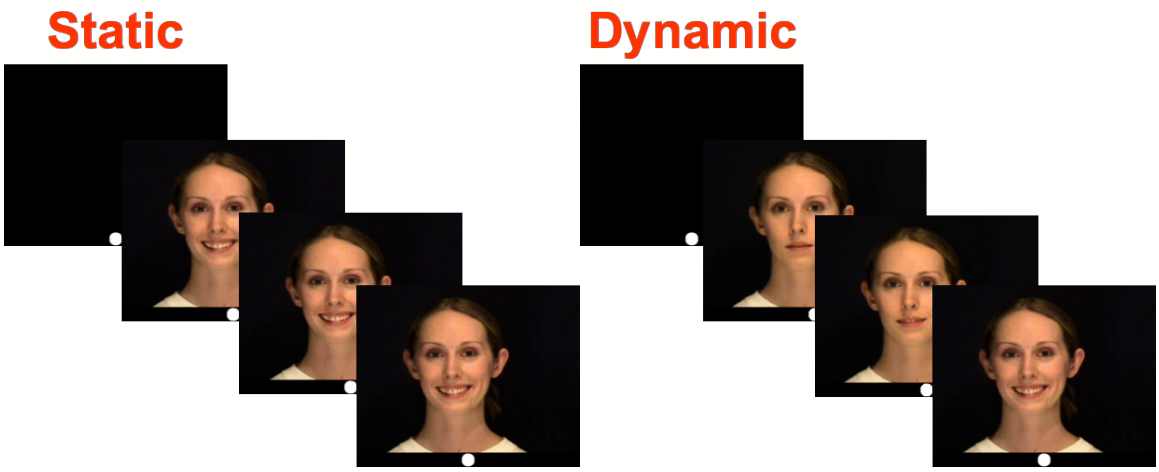

(a) Static (b) Dynamic

Figure 4.3: Face stimuli. (a) The static image is displayed over the same time period as the dynamic image which begins with a neutral expression and ends in an emotional expression.

Pre-recording Training

All participants practiced the task outside the shielded room to at least 95% proficiency. Each participant was instructed to sit quietly, focus on the images and indicate the sex of the face with their dominant hand using a three-button response box (Lumitouch, Burnaby B.C. Canada). The participants were trained to fixate on the image and to refrain from looking down at the button pad to make the button response. The typically developing children practiced until they were 100% proficient at distinguishing the different stimuli and able to press the button without looking at the button pad with little to no head movement. The children with DS also practiced the task outside the shielded room but were unable to become proficient at the challenges of the multitasking required to remember the buttons, press without looking and remaining still. The practice session was therefore modified so that the DS child verbally indicated their response. With this modified training, the children with DS also became proficient at recognizing the different stimuli to 95%-100%.

Data Recording

All measurements were performed at the MEG laboratory at the Down Syndrome Research Foundation (DSRF) in Burnaby B.C. using a 151 channel whole head MEG system (VSM MedTech). Participants were seated or supine in an electromagnetically shielded room (Vaccumschmeltz). Signals were sampled at a rate of 600 Hz with a bandwidth of DC to 150 Hz and 3rd gradient noise correction. One researcher sat inside the shielded room away from the MEG device to observe the subject and to provide supervision. All TD children were seated during data collection. The two children with DS were collected in a supine position to limit movement artifacts from head motion. The data were collected for three to four 5 minute epochs with the location of the head checked before and after the collection. The head location was determined by energizing and localizing three electromagnetic coils placed on the nasion, left and right preauricular points of the subject.

Procedure

Using a rear projection system the images were presented onto a translucent screen positioned 40 cm in front of the subject. The images and movies were presented randomly. Each image was presented for a fixed length of time (1000 ms) with a random inter-trial

stimulus before the next trial was presented (3750-4000 ms). The stimulus program was created to accept one of three button responses to identify the sex of the face. This feature was only used for the control participants. The stimulus was programmed to continue to the next image regardless of whether a button press was detected. A total of 32 trials were presented in one block. The block was repeated several times to achieve the desired total number of trials. Short 10 second breaks were interspersed within the block to allow the subject to blink. 50% of the images in a block were static images while 50% were dynamic movies. Of these, 90% were of faces and 10% were non-faces. For the control group, a total of 100 trials over all conditions were collected. For the DS group, a total of 260 trials were collected.

Data Processing and Analysis

Each 5 minute long collection was examined for data integrity and movement. The collection was accepted only if the head movement was less than 0.7 cm during collection and if it was within 1.0 cm from the other collections for the same subject. For each subject, data meeting these criteria were combined into one dataset of 5 minute long trials for further processing. The photo diode response was checked against the trigger timings. All triggers were within 25 ms (1.5 times the refresh rate) of the photo diode. The data was marked for each stimulus type and emotion. However, for this study, only static images with no distinction of emotion were combined for analysis. A total of 45-55 static facial triggers were identified for each of the TD participants while a total of 130-140 static facial triggers were identified for the DS participants. Signal to noise was therefore significantly better for the DS participants and individual results could be used for analysis. However signal to noise was not sufficient in the TD participants for individual analysis and therefore group averaging techniques were used for data analysis of the TD group. A multiple local sphere model was constructed for each subject using the head shape data collected from the Polhemus. This model describes the volumetric conductor boundary needed for source analysis. Sphere fits of less than 7% were reported for these participants and was well within acceptable fit levels. Event related SAM beamformer was used to create a volumetric description of the sensor data. Locations with the highest signal to noise ratio was identified for each individual subject. The average time distributions of virtual sensor signals from these locations were calculated between -100 ms to 600 ms. For the TD group, the virtual sensor

activity for the corresponding individual peak locations were averaged together due to poor individual signal to noise. For DS participants, individual time waveforms for the corresponding peak locations were used. Areas of peak activity similar to all control participants were selected for further analysis. Other areas of peak activity was assumed to be attributed to non-task related activations such as eye artifacts, motor and non-specific activity.

4.2.4 Results

Overall pattern of neural activation

In all children, viewing faces broadly evoked a similar pattern of neural activity in the occipital and temporal regions. Figures 4.4 and 4.5] show the grand averaged moments in the occipital and right temporal regions respectively. In each figure the average moment from the TD group is shown in comparison to the two participants with DS referred to as DS1 and DS2. Specifically, in the TD group, regions of peak power were observed in occipital and right temporal regions corresponding to the vicinity of occipital face area (OFA) and the right fusiform face area (FFA). The morphology of individual virtual channels for each source location was similar and confirmed the correspondence of these source activities between the individual participants. In 2 of the 5 participants, left temporal activation (left FFA) was also observed with similar morphology to the right temporal virtual channels. For the DS participants, regions of peak power were also observed in occipital and in bilateral temporal regions also in the vicinity of occipital face area and fusiform face area respectively. The right temporal area had larger activity than the left for both DS participants. The morphology of the virtual channels was similar to the corresponding grand averaged virtual channel of the TD participants.

Timing

Interestingly, although the general morphology of signals was similar between the two groups, there were differences in the peak latencies. Comparison of peak latency timings in the virtual channels between the two groups, revealed delays in the time to peak activity in the two participants with DS compared to the typical group in the occipital and temporal regions.

Figure 4.4 shows the grand average virtual channel for occipital activation for the TD group and the two children with DS. Note that the virtual channels are selected based on individual peak locations rather than an averaged peak location. In the TD group the first peak occurred in the occipital region at 113 ms after stimulus onset. This was followed by smaller peaks occurring at approximately 160, 270 and 350 ms. In the participant labeled as DS2, the first large peak occurred at approximately 128 ms followed by further smaller peaks at 250 and 318 ms. In the participant labeled as DS1 the first large peak occurred at 158 ms followed by further smaller peaks at 222 and 292 ms. In both DS participants a small (negative) peak near 100 ms was observed, however it was difficult to resolve this small peak in the control group due to the poor signal to noise.

Figure 4.5 shows the grand average virtual channel for the right temporal region. Only the right temporal region was analyzed for controls while both left and right were analyzed for DS participants. A single peak at 150 ms were prominent in the right temporal region in the TD group (the group average has smeared it's peak somewhat). The corresponding peak for one of DS participants occurred at 192 ms. This subject also exhibited a single peak morphology. However, the second DS subject had a more complex pattern. Two peaks were observed in this subject's data. The first peak occurred at 150 ms, 8 ms earlier than the activity in the occipital region. This was followed by a second peak at 220 ms. Analysis of the left temporal data demonstrated a pattern of activity similar to the TD participants right temporal activity.

In analyzing the timing of the virtual channels, a distinct pattern of neural activity emerged. In the TD group, 113 ms after the presentation of a static facial image, activity was observed in the central occipital region. This was followed by a large peak in the right temporal area at 150 ms. Further activity in the occipital region was noted at 270 ms. The participant labeled as DS2 exhibited a similar pattern of activation, although the latencies were delayed. Occipital activity occurred at 128 ms after onset of visual stimulus and was followed by activity in the left temporal region at 162 ms and closely followed by right temporal activity at 192 ms. The participant labeled as DS1, exhibited a different activation pattern. A peak was observed 150 ms after presentation of the visual stimulus in the right temporal region closely followed by occipital and left temporal activation. The difference in the peak timing between these regions was relatively small suggesting that activity in these regions may occur simultaneously. Further activation occurs in the right

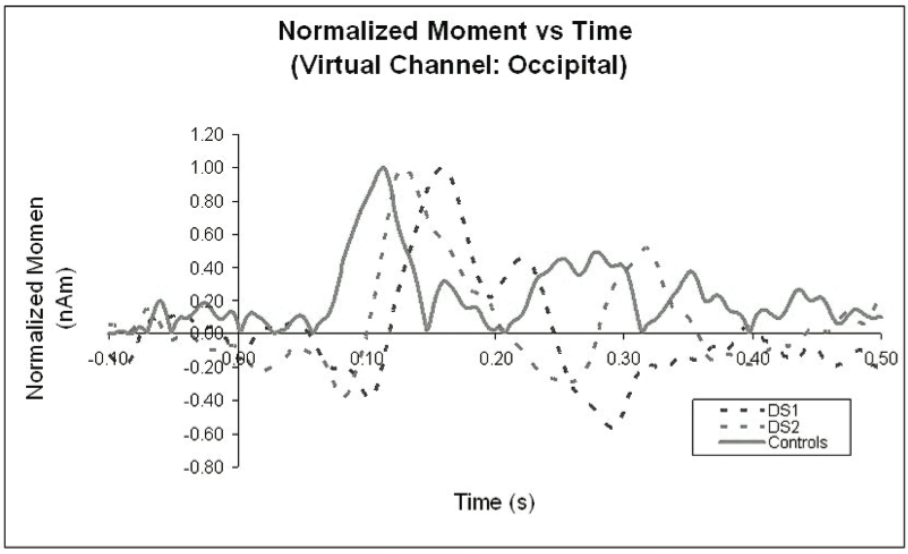

Figure 4.4: The normalized moment vs time for a virtual channel in an occipital SAM peak. The controls are plotted in solid grey and represents and average. The DS participants are plotted individually. Whereas the controls exhibit a typical M100 primary visual evoked response the DS subjects primary visual responses are delayed.

temporal at 220 and occipital at 222 ms.

4.2.5 Discussion

In this pilot study we measured the neural responses to emotional facial expressions in a group of TD children and compared these responses in two children with DS. Our preliminary findings suggest that the neural responses of all children show similarities in the general locations of activation. There were differences however, in the overall signal latencies and pattern of the responses in the two children with DS. In both children with Down syndrome, we observed a sequence of activity starting in the mid-occipital region corresponding generally to the occipital face area (OFA) near 100 ms. This smaller earlier peak was not observed in the TD data but may be consistent with other studies describing an early peak at 60-70 ms ([46]). In both DS participants, a second larger peak was observed in the same occipital region although at different latencies (128 and 158 ms). This second large peak corresponds to the 100 ms response in TD studies and may be reflective of face

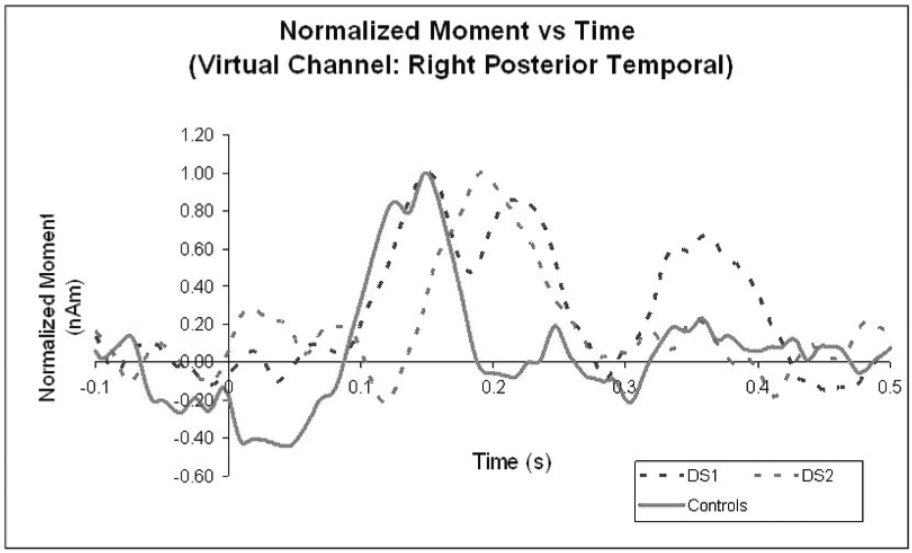

Figure 4.5: Normalized moment vs time for the virtual channel in a right posterior temporal SAM peak location. The controls are plotted as a grand average (solid grey) while the DS participants are plotted individually. The M170 response is typical in the controls but are altered in the DS participants.

specific processing ([48]). The sequence of activation between the two DS participants is more variable in comparison with the TD group. In one participant the sequence of activity is different from the TD group with right temporal activity corresponding generally to the fusiform face area (FFA) occurring 8 ms earlier than left temporal and occipital activity. In the other participant the right and left temporal regions showed peaks at 192 ms - 64 ms after the occipital activation. The latter subject's response is consistent with the typically developing group's sequence of activation of the occipital region followed by right temporal region as well as with literature although the timing is delayed. Further activity was then observed in the occipital region for DS2 in the later latencies, with little activity observed in the left and right temporal areas consistent with the typically developing participant's data and literature. However the latencies are again delayed. The pattern of activity in later latencies for DS1 is different from the TD group. These preliminary data are consistent with emerging behavioural evidence that children with DS have difficulties in recognizing and using emotional information from faces ([43], [94]). The results from this pilot study suggests that although viewing emotional facial expressions activates similar neural regions in

children with DS, the timing and pattern of these responses are delayed and more variable.

4.3 The role of the FFA, STS and OFA in the M170 Response to Faces in Adults

Functional magnetic resonance imaging studies have revealed a core facial processing network which involves the fusiform face area (FFA), occipital face area (OFA) and superior temporal sulcus (STS) ([33], [34]), which generally shows a right hemisphere dominance. In EEG and MEG, scalp electrodes and sensors near these anatomical regions also exhibit a difference in amplitude at around 170 ms between the perception of faces compared to object stimuli (N/M170). The effects are most prominent in the posterior channels, often larger in the right hemisphere. The neurogenerators of this EEG and MEG activity remain uncertain. Potential candidates include the FFA, OFA and STS consistent with the fMRI findings. While the 170 ms effect is evident in both MEG and EEG, MEG is best suited to find the sources because MEG has better spatial resolution to EEG due the insensitivity of magnetic fields to the changing conductivities in the head. The localization of this effect is challenging as it involves bilateral and highly correlated sources. However, a combination of event related beamformer and dipole fitting addresses this issue and reveals a core functional network for face processing. We studied the effects of face selectivity using data collected from two separate studies. In the first study the subjects viewed emotional faces and objects. The other study involved patients with prosopagnosia who underwent a battery of neuropsychological, behavioural, MRI, fMRI, EEG and MEG data recordings. In each study, full frequency neutral faces were presented to the participants. Using this neutral face data alone, each participant's face network was located using event related beamformer and dipole modelling and each location was tested for face-selectivity. Time averaged MEG face data localized at the M170 revealed a network of up to six locations bilaterally. Beamformer results often were unilateral showing only the dominant hemisphere. This effect was likely the result of correlation between the bilateral sources. However, the same core 6 locations were found across the subjects as a group. These locations corresponded to the FFA, STS and OFA core face network and when contrasted to the object data, all three areas showed face selectivity in some participants with the STS showing face

selectivity in all participants. Several of the subjects exhibited left lateralized rather than right lateralized face selectivity. In the patient data, all but one patient with lesions in the FFA showed no M170 response. For the patient with the M170 but no FFA, the location of the face selective M170 was found to be in the STS. These data support the hypothesis that the face-selective M170 generators are located in the FFA, STS, and OFA locations of the core face network.

4.3.1 Introduction

Facial processing is important for social human interactions and socio-emotional functioning. Studies have shown that people can identify and process faces faster than other object categories. The anatomical locations of the core face network have been identified robustly using fMRI consisting of the fusiform face area (FFA), occipital face area (OFA), and superior temporal sulcus (STS) ([63], [42], [96]). These studies image the response over seconds of activity during the presentation of face and non-face object stimuli. The temporal dynamics of the same paradigms has been characterized from electroencepahlography (EEG) recordings. An early response to faces versus objects occurs around 170 ms in EEG. This N170 response is characterized by a negative deflection between 140 and 200 ms after stimulus onset, which is larger for faces than objects and occurs bilaterally but stronger over the posterior right hemisphere consistent with one or more of the areas identified by fMRI. MEG studies have reported an M170 in roughly the same scalp locations and timing ([32], [39], [96], [20], [29]). Although there is still debate as to the equivalence of the N170 and M170 (Itier et al., 2006), most studies treat these two responses to be equivalent.

Localization of the M170 points strongly to the fusiform face area as a likely generator of the M170, however, there is evidence that it is not the only face-selective area active at this early latency. For example patients with prosopagnosia who show a loss of the FFA does not necessarily result in the loss of the N/M170 response [63]. Whether the FFA fully explains all of the M170 response has not been fully explored.

A serious issue that is not always addressed in the localization of the M170 is that the left and right hemisphere sources are highly correlated. The method chosen and the the approach to the MEG analysis is therefore critical in forming a complete picture of the M170 network. Methods such as minimum norm images bilateral activity consistent with fMRI

findings however source location is in question due to its depth bias towards shallower sources. Methods like beamformer have successfully identified contributions to the M170 neurogenerators but because beamformers are blind to correlated sources, the sources tend to be biased towards one hemisphere or the other, not unlike the situation faced with auditory sources. Null beamformers and bilateral source beamformers have imaged the bilateral nature of the M170, showing a major contribution from the FFA but these studies did not explore additional source contributions from the STS and OFA. Dipole analysis does account for correlated sources but again analysis using a 2 dipole fit is insufficient to account fully for the data variance observed.

The present study endeavours to extend the source localization strategies used in previous studies by continuing to look for additional sources in addition to the FFA to fully account for the M170 signals recorded. Of particular interest was the data that exhibited large residual variance after fitting the first dipole pair which. Data from three studies were utilized in the strategies developed for this analysis. In the first study, MEG was recorded while healthy adult participants viewed negative emotional faces and non-face objects while undergoing MEG imaging. In the second, the same participants viewed spatially filtered and full bandwidth face images and similarly altered non-face objects while undergoing MEG imaging. In the third study, patients with acquired prosopagnosia were imaged with EEG and MEG, separately while viewing faces and non-face objects. All the patients had also undergone behavioural and neuropsychological testing as well as structural and functional MRI recordings.The functional MRI utilized a face localizer (Fox et al, Human Brain Mapping 2009) that characterized the post-lesion status of the patient's core face-processing network (FFA, OFA and STS). These patients had combinations of lesions in FFA, OFA and STS some with M170 and some without M170 responses. MEG data using the full bandwidth neutral faces and non-face objects were used from each of the three studies for our data analysis.

Using a combination of event-related beamformer and dipole fitting, the core face network was localized for each healthy adult participant. A similar procedure was undertaken for the patients with intact M170 responses. The goal of this project was to determine a full description of the sources present at the M170 and to determine which of these sources were sensitive to face selectivity.

4.3.2 Methods

In the proceeding sections study A refers to the MEG data from healthy adult participants while viewing faces versus objects modulated by emotion and study B refers to the MEG data collected from patients with acquired prosopagnosia while viewing faces versus object stimuli. Note that only the full bandwidth, neutral faces were analyzed in this study.

Participants

Twelve healthy young adults (mean age: 26.2 years, 5 women, range: 19-41 years) with normal or corrected-to-normal vision participated in studies A. Participants self-reported right-handedness and had no history of neurological or psychiatric disorder. They were undergraduate or graduate students in the Department of Psychology at Simon Fraser University, Burnaby, British Columbia and either volunteered or participated for course credit. Three acquired prosopagnosia patients with brain damage, in one or more of the core face network were tested in study B. These patients also had normal or corrected-to-normal vision.

Stimuli

In study A, stimuli consisted of grey-scale photographs of front-view human faces showing a neutral, angry or fearful expression, or front-view objects of fishes, butterflies or guitars. Figure **??** shows examples of the face stimuli and figure **??** shows examples of the object stimuli. In study B, stimuli consisted of grey-scale photographs of front-view human faces showing a neutral expression, or front-view objects of fishes, butterflies or guitars. Every 2 out of 26 face images were inverted. It should be noted, where the conditions overlap, the same stimuli were used in both studies.

Average luminance did not differ across the face conditions and the butterfly condition was within 1 standard deviation of the face data. However both the fish and guitar images were more than 1 standard deviation from the other images. To ensure consistent results without confounds produced by image luminance differences, the guitar and fish conditions were not included in the analysis. See tables 4.1.

In all studies, faces and objects were presented with equal probability. All stimuli were viewed at a distance of 30 cm on a 42 cm x 32 cm screen (visual angle 56ą).

(a) Neutral (b) Angry (c) Fearful

Figure 4.6: Emotional face stimulus example. Neutral (a), angry (b) and fearful (c) were presented with equal probability.

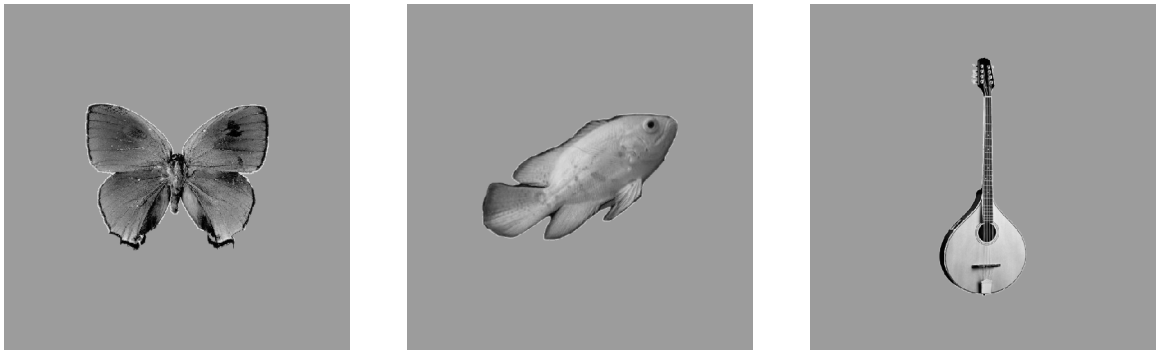

(a) Butterfly (b) Fish (c) Guitar

Figure 4.7: Object stimulus example. Butterflies (a), fishes (b) and guitars (c) were presented with equal probability.

Procedure

Participants sat in a dimly lit and magnetically shielded room at the Down Syndrome Research Foundation in Burnaby, British Columbia, and were instructed not to move their heads. A cuff was placed around the head to help the participant stay still. Participants practiced the task until they were comfortable with the button box before starting the experiment. In study A, Participants were instructed to make face-nonface discriminations. Participants signalled their response as quickly and accurately as possible by pressing a but-

Table 4.1: Mean luminance on a 256 grey-level scale

Image Category	# Images	Mean luminance	Standard Deviation
Face Angry	50	143.4459	2.5885
Face Fearful	50	143.9624	2.2913
Face Neutral	50	143.8920	2.2754
Butterfly	50	147.5770	3.6953
Guitar	50	153.7083	1.8366
Fish	50	152.0041	2.4645

ton for face and a second button for non-face stimuli with left and right thumbs. In study B, participants were asked to signal a response when an inverted face was presented. This response was predominantly used to ensure the subject was maintaining vigilance during the task. The stimuli in the three studies appeared one by one, in a randomized order, at the centre of the screen on a grey background for 500 ms, followed by a randomized jittered inter-stimulus interval of 1500 to 2500 ms (average: 2000 ms). The experiment was divided into three 5-minute blocks, separated by short pauses of 45-60 seconds. Participants were instructed and reminded to remain with their head as still as possible throughout the study.

Magnetoencephalography (MEG) recording

Whole-head MEG was measured in a magnetically shielded room while the participant sat with his or her head surrounded by the helmet shaped CTF 151-channel MEG system (VSM MedTech Inc., CTF Systems Inc, Coquitlam, B.C). Each MEG sensor consists of an axial first-order gradiometer, which were approximately 4.2 cm apart, with a 5 cm baseline and a 2 cm diameter. This system includes a reference array that allows third-order spatial gradient environmental noise cancellation (Xiang, Wilson, Otsubo, Ishii, & Chuang, 2001). Synthetic third-order gradient noise cancellation minimizes environmental noise and maximizes measurement of low frequency ranges (Fife et al., 1999). Data was recorded with the third-order gradients noise cancellation. The data was collected at a sample rate of 600 samples per second with a online hardware antialiasing filter set at 1/4 sample rate = 150 Hz. No other filters were used during collection.Head localization was collected at

the beginning and end of the main collection and subject with movement greater than 1 cm was excluded from the analysis. Head localization coils were placed on the left and right preauricular locations as well as 1 cm above the nasion location. The 3-D locations of such fiducial points, along with an average of about 500 points on the head surface, were recorded for each subject at the end of the session using a 3-D digitizer (Polhemus Inc., Vermont, USA).

Data Processing

In study A, the continuous data was divided into epochs according to the 6 conditions: face, angry face, fearful face, butterflies, fish and guitars. In study B, the continuous data was divided into epochs according to the 5 conditions, neutral face, inverted face, fish, butterfly and guitar.

The epochs were centred around the onset of the visual stimulus (time$\bar{0}$) with a pre-stimulus interval of 200 milliseconds and a post-stimulus interval of 900 ms. The buffer of 100 ms on either side of the epochs was to allow for filter ringing when filters are applied to the epoched data. It should be noted that there was potentially up to a one refresh rate jitter in the timing of stimulus equivalent to 16.7 ms. A total of 300 epochs were extracted for each subject. The epochs were then baseline corrected using the 200 ms prestimulus interval. Epochs contaminated with eye movements and other artifacts greater than 2 picoTesla within the 0 - 500 ms post-stimulus interval were removed from further analyses. The remaining epochs were averaged for each condition as well as averaged for all faces and all objects. A 1 Hz high pass filter and a 40Hz low filter were used for some of the subsequent analysis.

All of the the patients had structural MRI's but since only one of the heallthy adult participants had a structural MRI, source space analysis was done using a single sphere model for each subject. The best-fit sphere was obtained by fitting a sphere to the polhemus points collected relative to the fiducial markers which formed the subject's head coordinates. Because the nasion head coil was placed 1 cm above the true nasion, the coordinate system was a little bit different from what was normally expected. This did not however cause any difficulties in terms of source space analysis so long as this difference was accounted for when corregistering an average MRI to the results.

For the subjects with MRI, the polhemus data was carefully coregistered to the MRI to

allow for MEG source image overlay. For consistency, the best fit sphere from the pohemus was used for all the subjects regardless of whether a structural MRI was available or not.

Source space MEG analysis

Dipole fit was performed over a window of 10-15 ms around the peak of the M170 response using the face condition only. Dipole analysis was performed using a technique of adding pairs of bilateral mirror symmetric dipoles until the residual variance reported less than 10% difference between the model data and the measured data. Dipole analysis involving more than 2 or 3 dipoles tend to be very unstable and prone to local minima. To control the fit better, an iterative process was employed. The first pair of dipoles were freely fitted to the data. These dipoles were then fixed in place and a new pair of dipoles added. This pair was fitted to a point of stability. The first pair and second pair was then allowed to freely vary and fitted one more time. If necessary, the 4 dipoles were fixed and a 3rd pair of dipoles were added and the process repeated. While the positions were fixed, the dipole moment and orientation remained variable throughout the fits. At the end of each stage, a Monte Carlo process was employed to estimate the error ellipsoids for each dipole. If the error ellipsoids were more than 8 mm, the dipole fit was repeated until a set of locations were found that met our criteria. The 8 mm cutoff was somewhat arbitrarily set but does reflect the approximate spatial resolution achievable by real MEG recordings when head localization, sensor calibration and model errors are accounted for.

Beamformer analysis was conducted using event related SAM beamformer called Brainwave ([12]) and CTF SAM beamformer ([89]). Event related beamformer is based on SAM beamformer developed by Vrba and Robinson. Beamformer methods are voxel by voxel spatial filters that constructs linear combinations of sensors which sum constructively for the voxel location of interest while suppressing signals from other locations. Each individual voxel is treated independently and the result is a virtual channel which describes the moment over time at the voxel. The only drawback to the technique is that highly correlated sources are attenuated according to the amount of correlation. Event related SAM beamformer, selects for phase locked activity by averaging the resulting virtual channel signal relative to the specified stimulus. Phase locked events are more likely to survive the averaging process and these are typically the traditional evoked responses.

A covariance matrix was generated for each subject and each paradigm over the time

window of -100 ms and 800 ms over a filtered bandwidth of 1 to 40 Hz. The covariance was generated across all neutral face epochs (minus any epochs removed for artifacts). This provided a general set of weights that could then be applied to each condition individually. A baseline was defined between -100 and 0 ms. The individual subject best fit sphere as defined in the preprocessing was used to generate the lead fields. The coordinates and dipole orientation of peak activity were identified at the M170 using the face condition only. Virtual channels representing the source activity over time at those locations and orientations were then generated for each condition individually. The virtual channel for each condition was subsequently compared. As well, the beamformed locations were compared to the independently determined dipole fits. A final round of dipole fits were carried out, when the beamformed results suggested a better location for dipole locations. Regardless of whether beamformed results were bilateral or not, the dipoles were always modelled with mirror symmetric pairs.

Using the final dipole fit model, the dipole positions and orientations found for the neutral faces were used to compute the corresponding moment for each condition. It should be noted that unlike virtual sensors, it is not valid to use these positions to compute the moments over the entire epoch. This is because the model is only valid over the window of time used for the dipole fit. By changing the time, the dipole model may change to include other sources. In order to widen the time window, a more extensive search for all the significant dipoles over the window of interest must be identified and added to the model.

4.3.3 Results

Healthy Adults

The M170 latency varied from 125 ms to 185 ms between the 12 participants. Overall rms patterns revealed on average the participants exhibited a larger M170 for the face condition compared to the butterfly condition (picture). The beamformed results from the individual subjects were mixed. As a result of the correlation between left and right hemisphere sources, the beamformed results were often biased in favour of the hemisphere showing dominant facial selectivity. Table 4.2 lists the dominant hemisphere for each participant.

Eight subjects showed right sided dominance while 3 showed left and one had both.

Table 4.2: Lateralization of beamformer results. The dominant hemisphere of face processing for the beamformer analysis is shown here for each subject.

Subject	Dominant Hemisphere
1	Right
2	Left
3	Rightt
4	LEFT
5	LEFT FFA Right STS
6	Right
7	Right
8	Right
9	Right
10	Right
11	Left
12	Right

Where the beamformer showed a peak activity, the dipole fit results also showed a similar location of activity. Note that the dipole fit results yielded more sources because the activity was bilateral. In addition, when face was contrasted to object the direction of contrast (face larger than butterfly for example) agreed between beamformed virtual channels and the dipole moments at the M170. However, there was one exception. In one participant, the contrast between face and object was opposite between the moments in the dipole fit and the beamformed virtual channel. No matter how the data was modelled and how many sources were included, the results remained the same.

The dipole fits from the individual subjects were very consistent. 10 participant's data required 3 pairs of mirror symmetric dipoles to account for more than 90% of the data. The remaining two were fitted with 2 pairs of mirror symmetric dipoles. Spatially the dipoles corresponded well to expected locations for FFA, OFA and STS. This was further confirmed with one subject who had a structural MRI. Figure 4.8 shows the beamformer peaks at 185 ms and Figure 4.9 shows the 6 dipoles found for this subject. The beamformed locations are shown overlaid on the individual's MRI in Figures 4.10 (right FFA), 4.11 (right STS)

and **??**. The dipole fits are shown overlaid on the MRI in Figures 4.13 (right and left FFA), 4.14 (right and left OFA), 4.15 (right and left STS). There is good correspondence on the MRI between the beamformed results for this subject and the dipole fits.

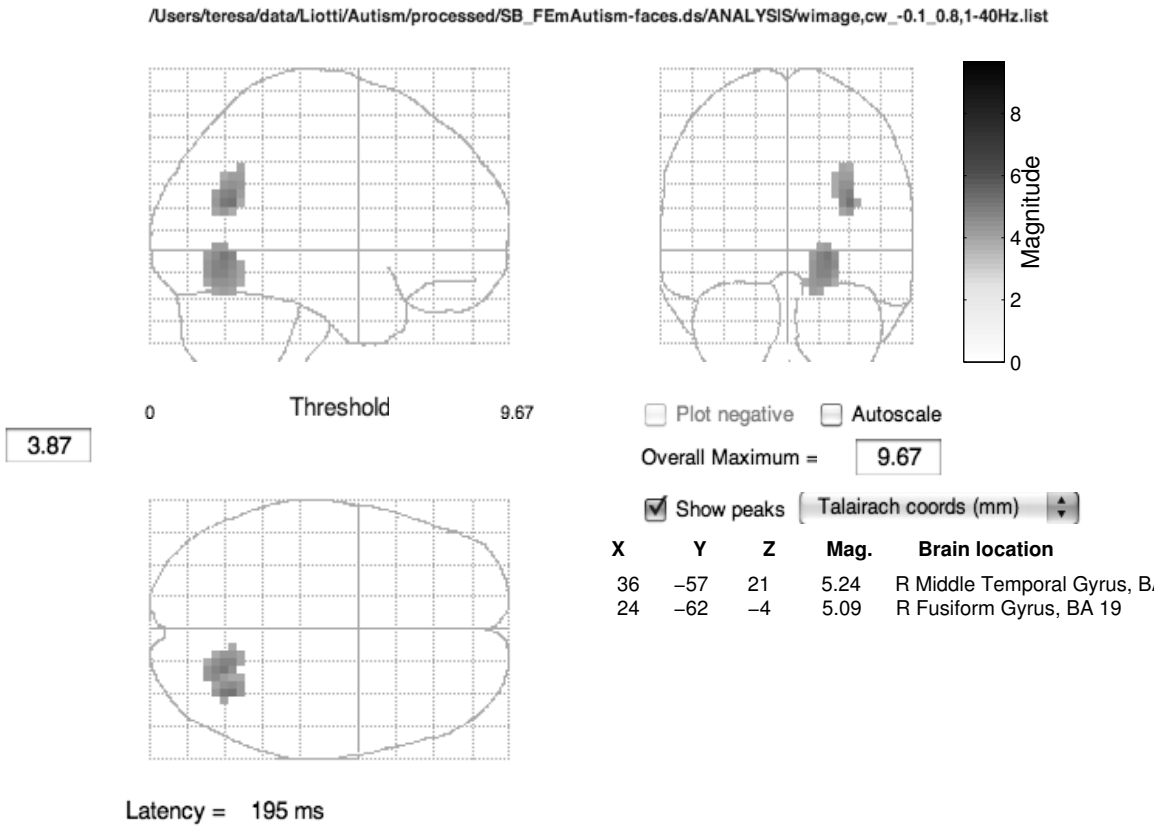

Figure 4.8: Subjec 12 Right FFA and STS from an event related beamformer analysis. The latency depicted is at 195 ms. In Talairach coordinates, both the right middle temporal gyrus and the right fusiform gyrus show peak activity.

Table 4.3 lists the dipoles which showed a face larger than butterfly moment at the M170. This table illustrates the variability between the subjects. It is interesting to note that the subjects showing left dominance in the beamformer results indeed mainly had face selectivity on the left side. As well, two subjects showed only face selectivity in the STS with no FFA involvement. There was a peak found in the beamformer for PP also in the left STS. The virtual channel values between face compared to butterfly agreed with the dipole result.

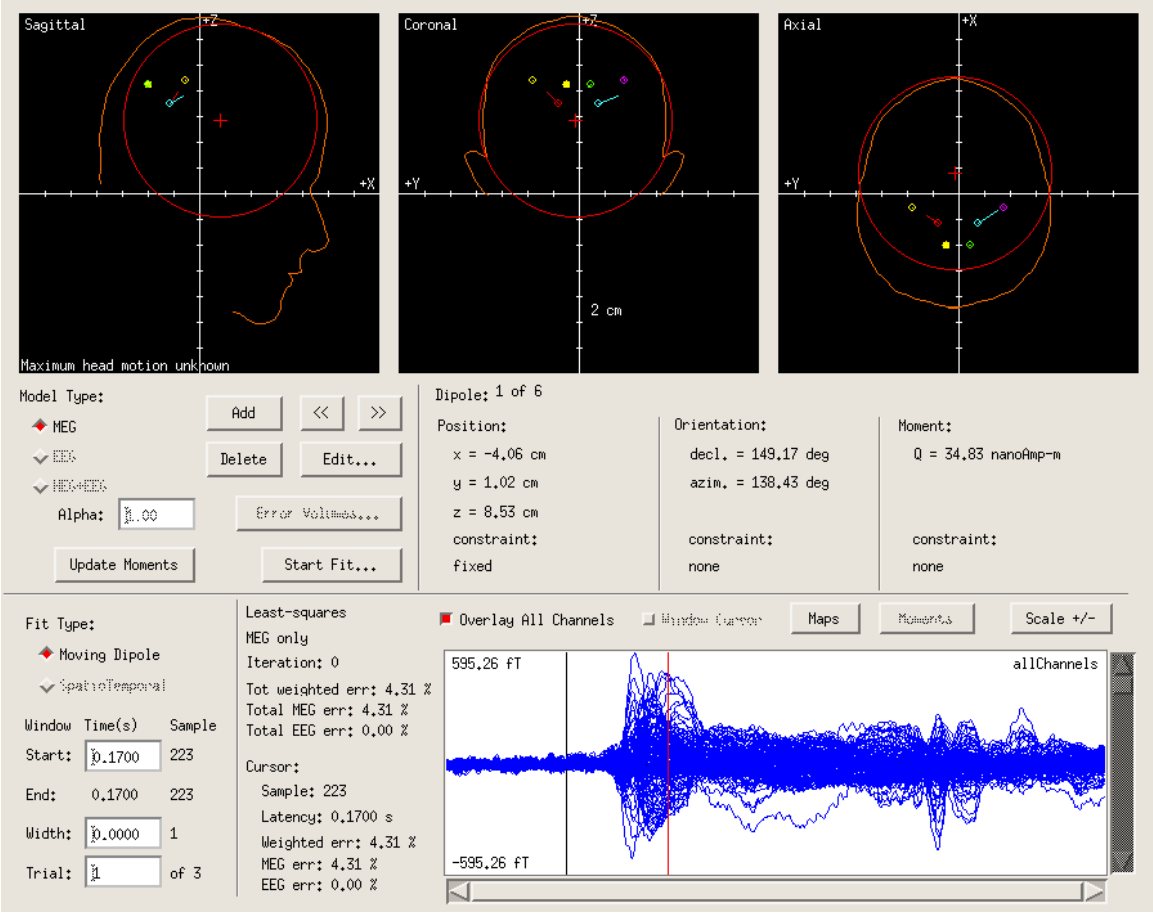

Figure 4.9: The equivalent current dipole fit using three pairs of symmetric dipoles at the M170 for subject 12.

Note too that the STS was the only location that showed face selectivity in all the participants. The FFA appeared in 10 out of the 12 participants and the OFA appeared in 8.

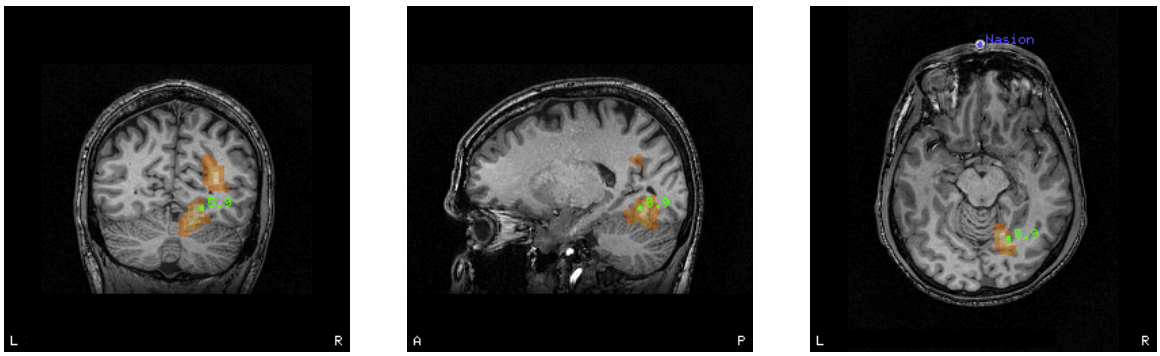

(a) coronal (b) sagittal (c) axial

Figure 4.10: Subject 12. SAM beamformer peak in the vicinity of the right FFA overlaid on the subject's structural MRI.

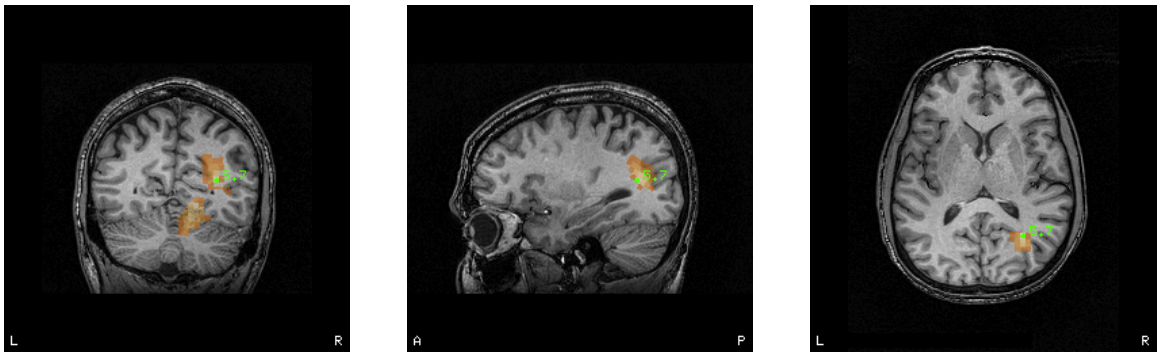

(a) coronal (b) sagittal (c) axial

Figure 4.11: Subject 12. SAM beamformer peak in the vicinity of the right STS overlaid on the subject's structural MRI.

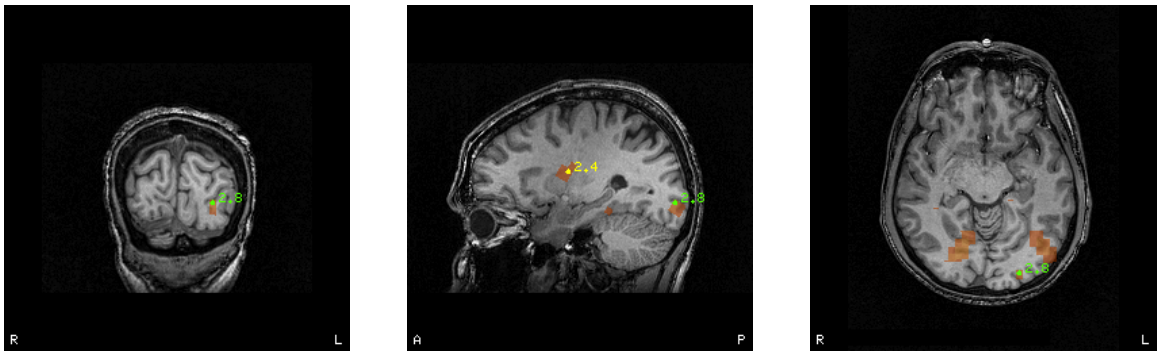

(a) coronal (b) sagittal (c) axial

Figure 4.12: Subject 12. SAM beamformer peak in the vicinity of the left OFA overlaid on the subject's structural MRI.

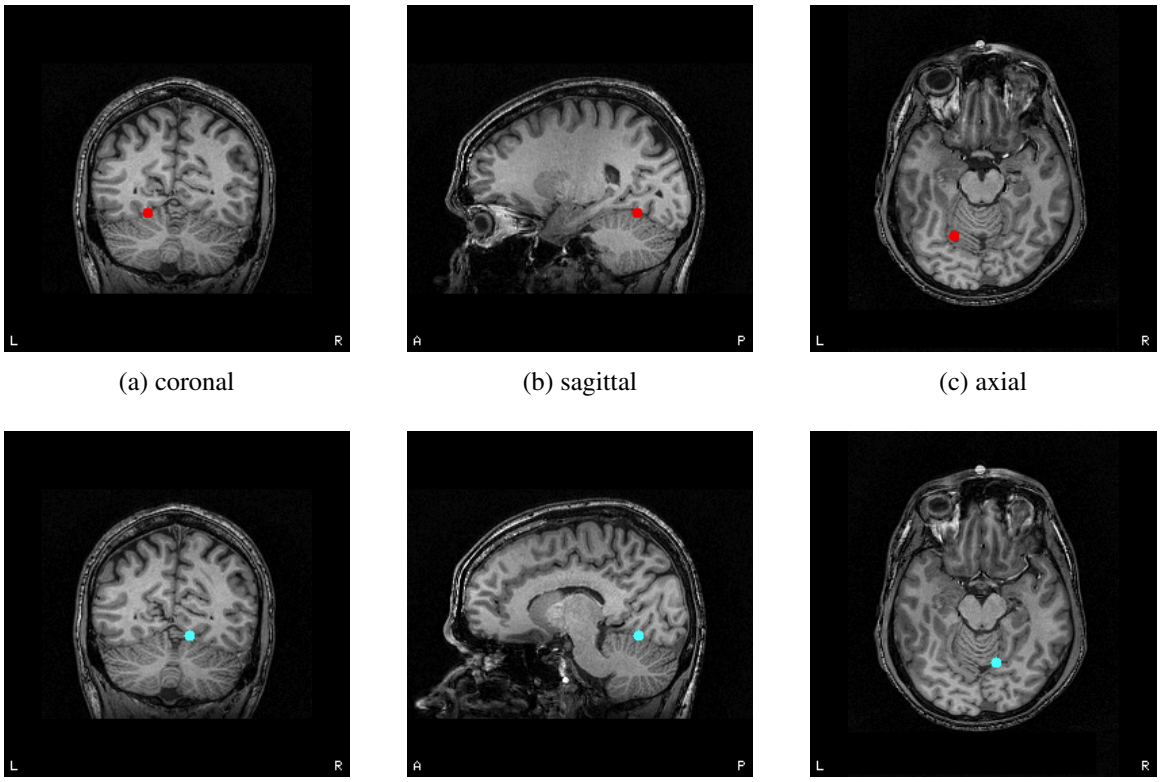

(a) coronal (b) sagittal (c) axial

(d) coronal (e) sagittal (f) axial

Figure 4.13: Subject 12. Dipole fit of the left (a)-(c) and right (d)-(f) dipoles in the vicinity of the FFA.

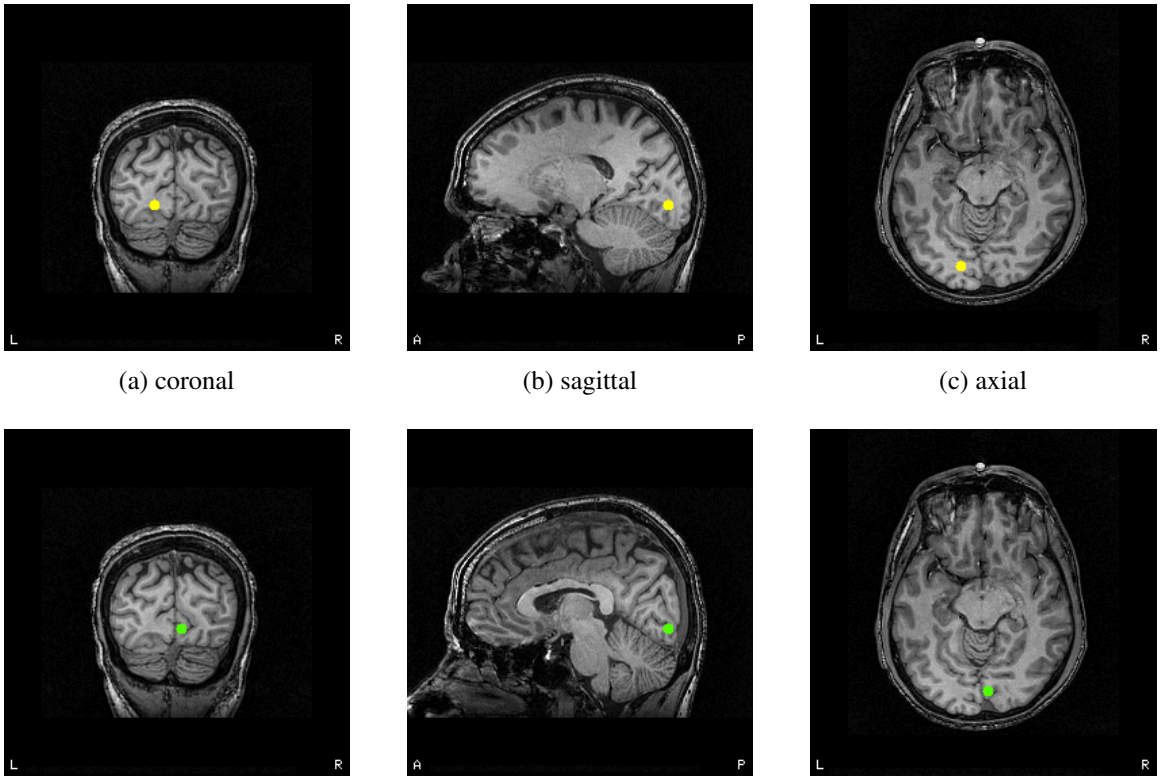

(a) coronal (b) sagittal (c) axial

(d) coronal (e) sagittal (f) axial

Figure 4.14: Subject 12. Dipole fit of the left (a)-(c) and right (d)-(f) dipoles in the vicinity of the OFA

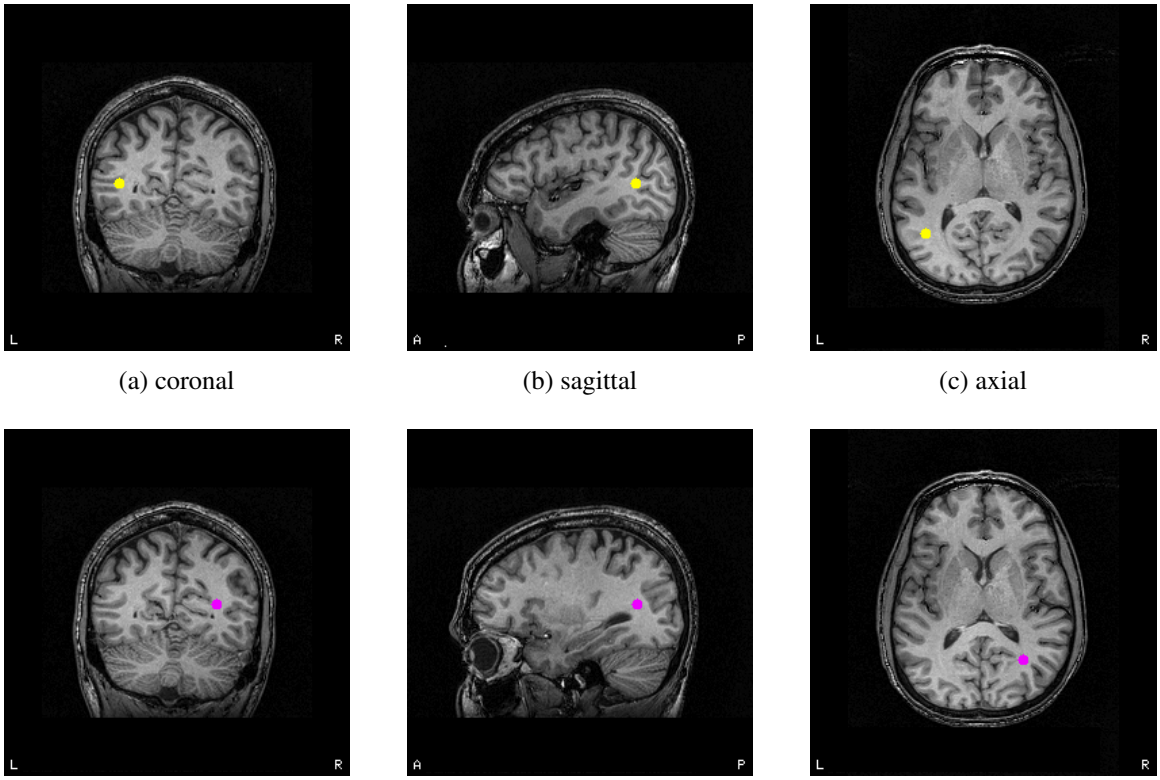

(a) coronal (b) sagittal (c) axial

(d) coronal (e) sagittal (f) axial

Figure 4.15: Subject 12. Dipole fit of the left (a)-(c) and right (d)-(f) dipoles in the vicinity of the STS

Table 4.3: Locations that showed larger moments at the M170 for faces compared to objects. The beamformed dominant hemisphere is repeated in the middle column. The right column shows the locations which exhibited face selectivity.

Subject	Hemisphere	face selective dipoles
1	Right	R FFA, R STS, RL OFA
2	Left	L FFA, L STS, L OFA
3	Right	RL FFA, L STS
4	LEFT	L FFA, L STS, RL OFA
5	L FFA R STS	L FFA, R STS, RL OFA
6	Right	R STS
7	Right	RL FFA, RL STS, RL OFA
8	Right	RL FFA, R STS
9	Right	RL FFA, RL STS, RL OFA
10	Right	L FFA, R STS, RL OFA
11	Left	L STS
12	Right	RL FFA, RL STS, L OFA

Patients

[3]

Of the three patients, only one showed an M170. The two patients with no M170 suffered a loss of both FFA and OFA. The patient with an M170 suffered a loss of only the FFA. The beamformed analysis of this patient showed a network of activity illustrated in figure 4.16. The corresponding virtual channels are shown in figures 4.17, 4.18, 4.19. At the M170, the region with significant difference between face and butterfly is in virtual channel 1 which corresponded to the location of the STS for this patient.

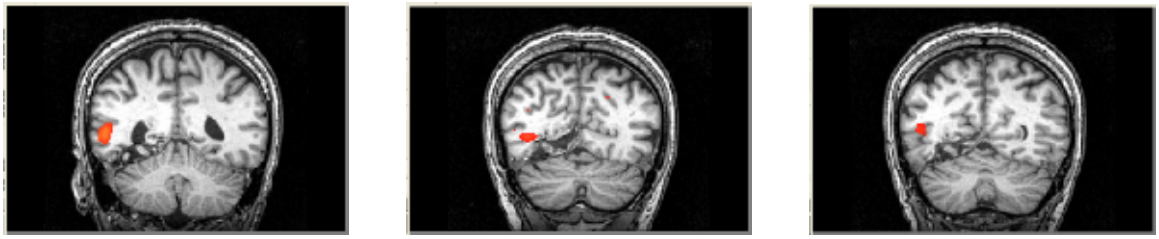

(a) V1 (b) V2 (c) V3

Figure 4.16: Patient Beamform Peaks at location V1, V2, and V3. These labels do not have specific physical meaning and used only to label the virtual channels. V1 corresponds the the subject's STS found in fMRI.

[3]This section has been published. Oruc, I, Cheung, T, Dalrymple, K, Fox, C, Iaria, G, Handy, T, and Barton, J. Residual face-selectivity of the N170 and M170 is related to the status of the occipital and fusiform face areas in acquired prosopagnosia. In Journal of Vision, 10, 7 (2010), 585-585 [63]

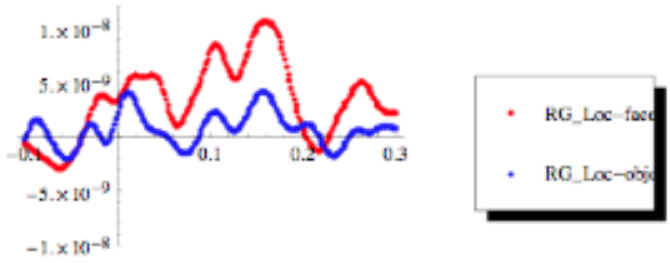

Figure 4.17: Virtual channel V1 time course. The Y axis is in units of A-m and the X axis is in units of seconds. The V1 location corresponds to the subject's STS. The face condition (red) is compared to the object condition (blue).

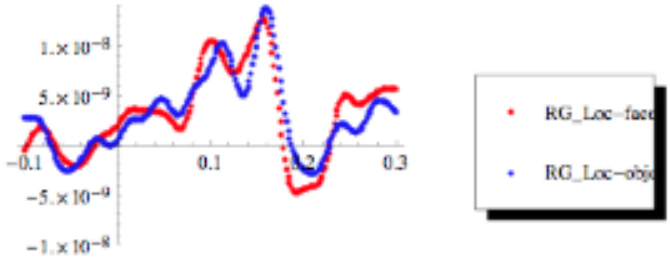

Figure 4.18: Virtual channel V2 time course. The Y axis is in units of A-m and the X axis is in units of seconds. The face condition (red) is compared to the object condition (blue).

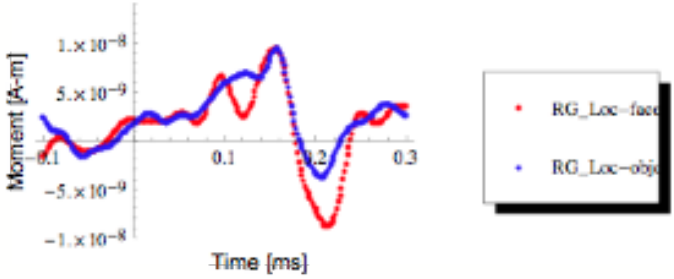

Figure 4.19: Virtual channel V3 time course. The Y axis is in units of A-m and the X axis is in units of seconds. The face condition (red) is compared to the object condition (blue).

4.3.4 Discussion

While the ERP and MEG data on the scalp level suggest bilateral source activity in an occipital-temporal location, previous studies are inconclusive with regards to the location of the M/N170. It has been suggested that the discrepancies lie in the differences in methods used to localize the M170. Dipole source models show a localizations to the OFA ([25]) while beamformed and minimum norm results have localized to areas of the STS and FFA ([39], [29]). These studies strongly suggest that multiple simultaneous sources are involved in the M170 signal. Our source modelling results support this hypothesis.

We used MEG data to localize the core face processing network. Using a combination of beamforming and dipole fitting, it was established that up to 6 dipoles were needed to fit the MEG data. The goodness of fits exceeded 90% with excellent correspondence to beamformed locations. These locations corresponded to the fMRI core face network consisting of the FFA, OFA and STS. We had one subject with MRI and the dipole fit locations for this subject agreed well with fMRI descriptions of the core face network. While the beamformer was unable to pick up the bilateral activity, it served as a useful check of locations for the dipole fit as well as independent verification of face selectivity when peaks were found in the beamformed images. The bias towards the dominant face processing hemisphere observed in the beamformed results was likely due to correlations between the left and right hemisphere sources. Future analysis should include a measure of this correlation as well as measures of connectivity.

When the source locations were contrasted between face and butterfly conditions, the STS was the only location that exhibited face selectivity for every subject. It is interesting to note that the patient with prosopagnosia also had a face selective STS location and the observed M170 with no right FFA was likely originating from the STS location. This study suggests the STS has an important functional role in the processing of faces at the neural level. Further investigation into the role of the STS is needed. This study also showed that the M170 originated from the co-activation of all three core face network locations.

4.3.5 Conclusion

This study had two important outcomes. For the first time, a dipole model of the face network was found for each subject individually that included the three core face network

areas of the FFA, OFA and STS. Second, the STS seemed to be an important contributor to the M170.

4.4 Future Work and Conclusions

This chapter examined the M170 in sensor and source space. It was found that the M170 in typically developing children appeared to exhibit the same temporal profile as the M170 in adults. Children with Down syndrome exhibited a delayed or altered morphology in both source and sensor space. The M170 was larger for dynamically presented facial images compared to static. Finally, the M170 appeared to originate from a co-activation of multiple sources which included all three areas of the core facial network of the FFA, STS and OFA. A patient with brain damage in the right FFA showed an M170 which suggested that the FFA was not necessary for M170 generation and further source analysis revealed the face sensitivity originated in the STS in this patient.

The data from the third paper also included strong negative emotional content which was not presented in this thesis. Future work should examine the six source locations found under emotional modulation. In addition the same participants were also scanned with MEG while viewing faces and objects presented in high, low and broad spatial frequency. Modulation by spatial frequency of these source locations will also be examined. Analysis already done at the sensor level suggests that emotion increased the amplitude of the M170. It would be interesting to examine which source locations exhibit this increased activity. Sensor and dipole source analysis of the right FFA source location indicated that modulation by low spatial frequency tends to occur earlier and with larger amplitude than neutral and high spatial frequency faces. Besides the FFA, which of the remaining sources also shows this modulation should be examined next.

Finally the six source locations should be analyzed for correlation to confirm the why the beamformer results were lateralized and connectivity between these locations should be part of future work on these data.

Chapter 5

Magnetic Nanoparticle Imaging

5.1 Detection of Magnetic Nanoparticles using Sensor Noise for Magnetoencephalography Imaging

[1]

5.1.1 Abstract

Ferrofluids are colloidal suspensions of magnetic nanoparticles in a liquid carrier. The particles are coated with a shell that keeps the ferrofluid grains from agglomerating. These particles are on the order of 10 nm and are considered to be single-domain [72]. Ferrofluids have found applications in biomedicine because they are non-toxic and detectable in opaque tissue. Studies such as Romanus [68] have demonstrated that when bound to a biological marker and subjected to an external field, the relaxation of the magnetic fields of these nanoparticles are detectable and localizable in vivo using SQUID magnetometers. Jia [41] has demonstrated that commercial magnetoencephalography (MEG) devices are sufficiently sensitive to detect the rigid rotations of these particles without pre-magnetization. These studies suggest the possibility of enhancing magnetoencephalography signals by selective targeting using magnetic biomarkers.

[1] A version of this section was published. Cheung, T, Kavanagh, K, Moiseev, A., and Majumder, S. Detection of Magnetic Nanoparticles using Sensor Noise for Magnetoecephalography. In Human Brain Mapping 2009 Proceedings (2009) [7]

Our study aims to demonstrate the detection of the magnetic nanoparticles without the aid of mechanical rotation by measuring the random rotations of the particle's magnetic moments. We hypothesize that these rotations will cause an increase in sensor noise across frequencies which will be difficult to detect in the time series MEG signal but can be observed in the frequency domain. Changes in moment orientation occur through two mechanisms: Brownian rotation and Néel rotation.

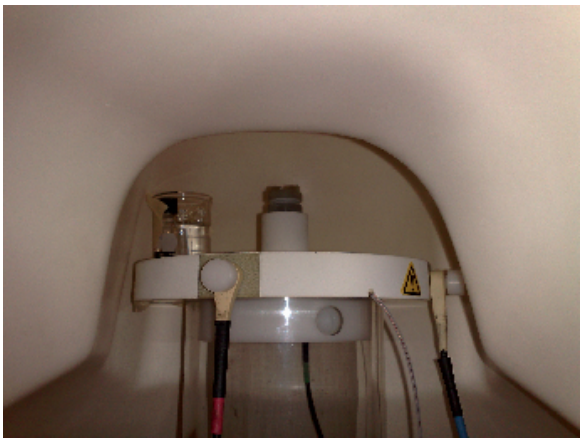

Figure 5.1: Ferrofluid in MEG. The ferrofluid is in the glass beaker water bath (left side of stand).

5.1.2 Methods

A commercial ferrofluid (1 ml) from Ferrofluidics Corporation was placed in a small nonmagnetic glass cylinder and sealed. MEG noise data (10 trials, 1200 Hz sample rate, 120 Hz anti-aliasing filter) was collected with and without the sample inside the helmet region. To further explore the nature of the noise, the sample was also measured at different temperatures. The sample was placed in a water bath of 70 C and positioned within the MEG helmet (Figure 5.1). Data was collected as the water cooled to room temperature. Without moving the sample, ice was introduced to the water bath and left to warm to room temperature as data was again collected. These measurements were then repeated. The 10 trials were averaged in the frequency domain for each channel of each data set.

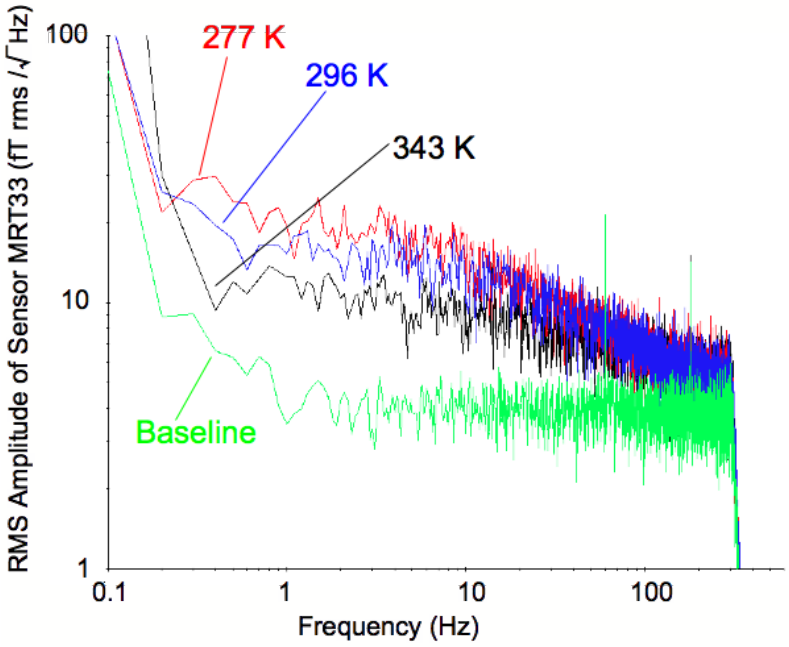

Figure 5.2: FFT as a function of temperature

5.1.3 Results

Figure 5.2 shows a log-log plot of the stacked frequency spectrum for the sensor channel closest to the sample at three temperatures and at baselline (no sample). Regardless of temperature, the frequency spectrum of the MEG data with the sample present was larger than the baseline sensor noise in all measured frequencies although preferentially for the lower frequencies. For the measured temperature range of 70 C to 4 C the noise was observed on average to increase as temperature was decreased.

5.1.4 Conclusion

The random rotations of magnetic moments from a small vial of ferrofluid was detectable using a whole-head MEG device without resorting to mechanical rotation. The presence of the ferrofluid caused an increase in sensor noise through all frequencies of the measured spectrum although the nature of the noise was not white. A temperature dependence was also observed. Detection of these particles using changes in sensor noise rather than sensor signal may lead to different techniques for magnetic nanoparticle localization in vivo.

5.2 A new technique for magnetic nanoparticle imaging for magnetoencephalography using frequency data

[2]

5.2.1 Abstract

Nanoparticles are objects of nanometer dimensions. Magnetic nanoparticles consist of an inorganic core of iron oxide. An outer coating of bioactive molecules such as peptides or antibodies surrounds this core, which can be chemically functionalized to conjugate with specific molecules in cells. There is potential to utilize the magnetic properties of these particles for internal imaging of living organisms using magnetoencephalography (MEG). While it is clear that bulk movement of a collection of particles should be detectable by MEG either as a flow or via rigid mechanical motion, it would be far more useful to detect the particles in situ. We have taken the first step towards this goal by demonstrating that MEG can detect these particles at fixed locations by focusing on the magnetic noise generated from random rotations of the particles' magnetic moments. Using a 151-channel MEG device, a glass vial of Fe_3O_4 in a colloidal suspension was measured at stationary locations within the MEG helmet region. The data was collected at 300, 1200 and 12000 Hz and up to 4000 Hz bandwidth. Between 10 and 50 ten-second trials were collected. Fast Fourier transforms for each MEG channel was generated. The net effect of these fluctuations was not detectable in the time domain. However, these fluctuations appeared as an increase in noise in the frequency domain. The character of the noise had a $1/f^n$ slope where 0<n<1 with n approaching 0 (= white noise) as the concentration of the sample was reduced. Spatial contour maps of the frequency data showed a distinct peak near the location of the sample. These results suggest that MEG is sensitive enough to detect and potentially localize a stationary vial of magnetic nanoparticles in a colloidal suspension.

[2] A version of this section was published. Cheung, T, Kavanagh, K, and Ribary, U. A new technique for magnetic nanoparticle imaging for magnetoencephalography using frequency data. In 17th International Conference on Biomagnetism Advances in Biomagnetism (2010). [8]

5.2.2 Introduction

Nanoparticles are objects of nanometer dimensions. They consist of an inorganic core, such as gold, silicon, cadmium selenium or iron oxide. This core provides the functionality of the particle such as being fluorescent or magnetic. An outer shell often with a coating of bioactive molecules such as peptides or antibodies surrounds this core. These surface molecules can be chemically functionalized to conjugate with specific molecules in cells such as proteins. For example, semiconductor fluorescent nanoparticles have been synthesized to conjugate to neurons and glia [64]. Using fluorescent microscopy, the movement of neuroreceptors can be visualized and tracked [17]. This process, however, has limited application in vivo where the presence of opaque tissue may prevent the ability to perform fluorescent microscopy. Magnetic nanoparticles can be detected in opaque tissue. Coupled with the highly sensitive magnetic field detectors called SQUIDs (superconducting quantum interference device), there exists exciting research and clinical possibilities to create a new technique for internal medical imaging.

MEG is a device consisting of multiple SQUID channels for the purpose of noninvasively detecting biological magnetic signals. MEG has been used mainly to detect natural biological signals such as the magnetic fields produced by intracellular currents of depolarizing neurons in the brain [85]. There is no restriction technologically to expand its usage to other sources of magnetic field generators such as the movement of magnetic nanoparticles. Used in this way, the technique would be akin to PET for magnetic rather than radioactive particles.

There have been a small number of studies involving nanoparticles and MEG. Romanus [68] and Jia [40],[41] have demonstrated that SQUID sensors can detect magnetic nanoparticles subjected to premagnetization or in motion. Saligram [69] showed that these particles could be detected in the MCG (magnetic cardiogram) of rats when the particles were introduced into the bloodstream or heart. These studies showed changes in magnetic field signals over time. There have been no studies examining the frequency and thereby noise characteristics of magnetic nanoparticles.

Ferrofluids are colloidal suspensions of magnetic nanoparticles in a liquid carrier. The particles are coated with a shell that keeps the particles from agglomerating. Magnetic nanoparticles with core sizes between 10 nm and 100 nm are predominantly single domain

in their magnetic structure [72]. A single particle can be described as a magnetic dipole and the magnetic field equations are derived using Maxwell's equations. These particles can be made to be either superparamagnetic or ferromagnetic. Particles in a colloidal liquid have moments that change randomly according to two processes. Brownian rotation refers to the random rotation of the whole particle itself, which causes a change in moment. Néel rotation refers to the random rotation of the moment within the particle [72]. There is also Brownian translational movement of the particle. The two rotations contribute to the net moment change for each particle and together with translational movement give the measured magnetic field at any point in space and time. When bounded to the target molecule, the magnetic nanoparticle movement and whole particle rotation will be affected by the properties of the target molecule. However, Néel rotation is hypothesized to remain unchanged. By looking in the frequency domain, it may be possible to observe these random rotations if the moments are large enough to be detected. Our study examines the potential for utilizing frequency data to detect and localize a colloidal sample of magnetic nanoparticles.

5.2.3 Methods

Sample Preparation

A sample of ferrofluid manufactured by Ferrofluidics Corporation (Burlington, Massachusetts) was used for our data collections. The sample was a water based colloidal suspension of Fe_3O_4. A 0.5 ml volume of the ferrofluid was placed in a nonmagnetic cylindrical glass vial. The empty container was checked for magnetic contamination before usage. A second diluted sample was prepared using 5 parts deionized water to 1 part ferrofluid.

TEM Measurements

To measure the particle size and confirm the particle's chemical composition, the diluted sample was imaged using a transmission electron microscopy (TEM) operating at 200 keV (point to point resolution 0.23 nm). A carbon grid was used to hold a dried sample of the diluted ferrofluid. Bright field images (with objective aperture), high magnification images (no objective aperture) and selected area diffraction patterns were collected for the sample (Figure 5.3).

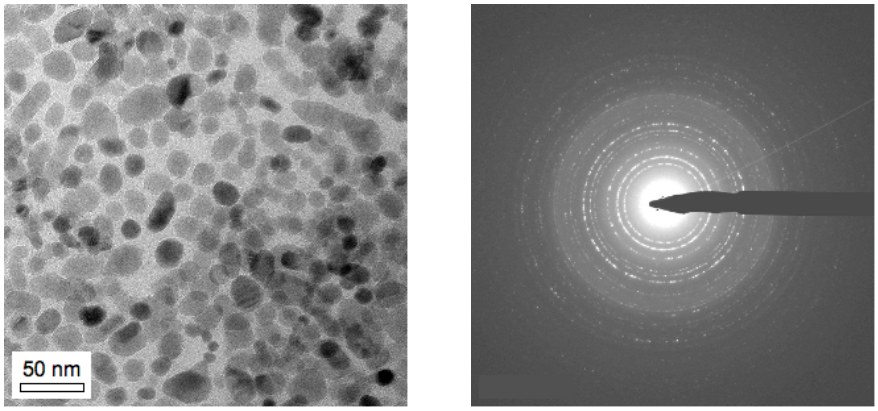

(a) Bright field TEM image (b) Diffraction pattern

Figure 5.3: TEM Image with corresponding rings selected over diffraction pattern

MEG Measurements

The sample was placed on a nonmagnetic phantom stand. The stand has calibrated locations for placement of fiducial markers to track the sample's location during MEG measurement relative to the sensor coordinates. Polhemus was used to digitize the sample's location relative to these calibrated fiducials. We estimate the sample's measured location error was between 1 to 3 mm. A 151-channel CTF MEG device within a 4-layer Vacuumschmelze magnetically shielded room (MSR) was used for the measurements.

Noise data was collected for the empty room, empty container, a sample of liquid water and the empty phantom stand to confirm that the equipment without the sample did not change the empty room noise floor.

Each colloidal sample mounted on the phantom stand was measured at stationary locations within the MEG helmet region. To minimize magnetization effects, head localizations, which involve the generation of magnetic fields within the helmet, were done only when necessary and only at the end of a data collection. The data was collected at 300, 1200 and 12000 Hz. There was a permanent anti-aliasing filter set at 1/4 sample rate during all collections. The data was collected with synthetic third gradient cancellation enabled. Between 10 and 50 ten-second trials were collected. To check the stability of the sample, data was collected over a period of hours without disturbing the sample.

Data Processing

The particle sizes were manually measured from the bright field TEM images. Spatial Fourier transforms were performed on the fringe patterns observed in the high magnification images. The diffraction rings were measured by generating intensities along a line that intersected the ring centre as a function of distance. Peak pairs were marked to identify ring boundaries. The diffraction ring diameters were defined to be the distance between these peak pairs. The ratios between radii pairs were computed. These were matched to known patterns to identify the chemical composition.

There were no offline filters applied to the MEG data. The bandwidth was therefore 0 to 1/4 sample rate. Fast Fourier transforms for each MEG channel was generated and averaged (stacked) across the trials. Topological maps were also generated in the frequency domain. Selected frequencies were examined in the alpha, beta, and gamma bands. An amplitude was generated for each sensor by integrating across approximately a 1 Hz frequency range at the selected frequency.

5.2.4 Results

TEM Results

TEM revealed the particle core sizes were between 10 - 50 nm. Diffraction pattern analysis confirmed the core was made of crystalline iron oxide, Fe_3O_4. Some particles seemed to have aligned to form lines. There was no evidence of a shell surrounding the ferrofluid droplets.

MEG Results

The sensor noise floor is unique to each channel and does not generally change over time while the MEG system is cold and operational. Data from noise taken at the beginning and end of collections confirmed this stability. Noise data of empty container, a sample of liquid water and the empty phantom stand showed no significant difference from the empty room noise (right plot in Figure 5.5).

In the time domain, differences between the data with and without the sample were difficult to detect. Although some channels were noisier, the information was difficult

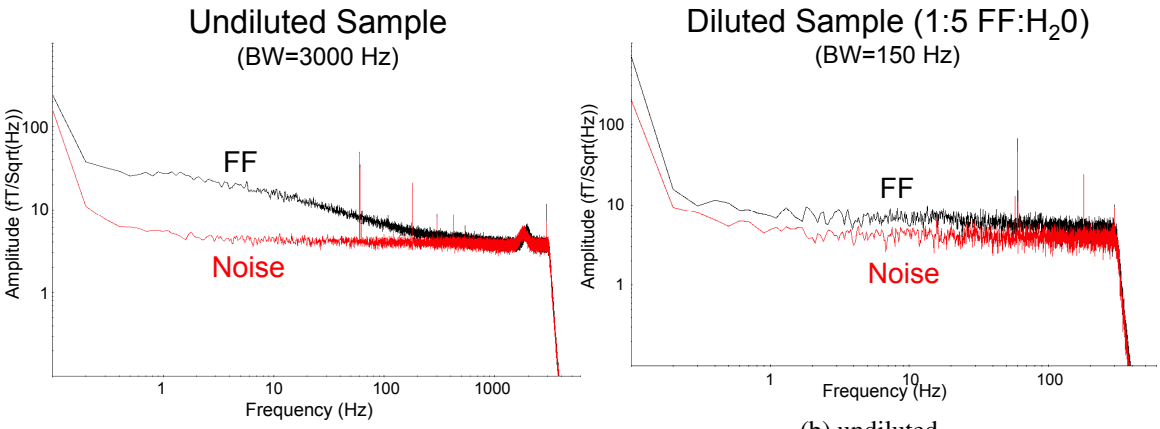

(a) diluted

(b) undiluted

Figure 5.4: Sensor noise compared to ferrofluid noise for a single channel. The undiluted sample compared to empty room noise is shown in (a) while the diluted sample compared to empty room noise is shown in (b).

to quantify in the time domain. However, in the frequency domain, these fluctuations appeared as an increase in the noise floor. Figure 5.4 (left) shows a log-log plot of one of the sensor channels closest to the ferrofluid sample. The slope of the noise has a $1/f^n$ characteristic where n is between 0 and 1. Figure 2 (right) shows a diluted sample placed at the same location for the same sensor channel. The slope of the noise is nearly white (n=0) but the data with the sample still shows an increase in the noise floor.

Figure 5.5 shows spatial contour maps of the frequency data in the bandwidth 1.98 to 2.94 Hz. In the left map, the sample was placed at the back of the helmet (occipital). In the right map, no sample was present. Comparison between the two maps shows a distinct increase in frequency power at the location of the sample. The same results were observed for different bandwidths until the noise floors of the two datasets merge at higher frequencies.

5.2.5 Discussion

The MEG frequency data analysis suggests that a liquid colloidal suspension of magnetic particles with sufficiently large moments can be detected. The diluted sample showed a nearly white noise profile with an increase in noise floor when the sample was present. We

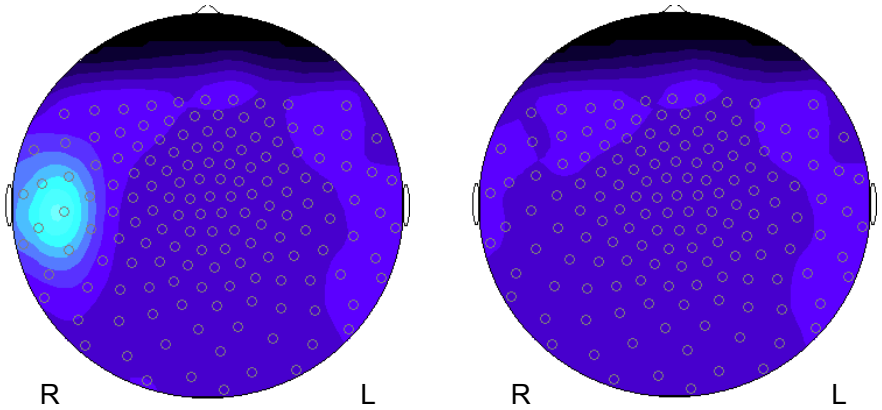

(a) with sample (b) without sample

Figure 5.5: Fourier transform spatial contour maps. Bandwidth = 1.98-2.94 Hz. The sample can be seen to rise above the background power in (a) compared to (b).

do not understand yet what causes the increase in signal. It is not clear if the undiluted sample included interactions beyond random rotations although the noise profile would suggest this is probable.

There was a spatial correlation between location of the sample and increase in sensor power. These results support the possibility the MEG can be used to localize the sample spatially. A technique such as synthetic aperture magnetometry beamformers may be adaptable for such a purpose. We have used a specific ferrofluid for these collections. Further tests to examine other magnetic nanoparticles are needed to determine which are suitable for this technique. Whether the particles are superparamagnetic or ferromagnetic also plays a role in detectability. The nonzero magnetic field within the MSR allows superparamagnetic particles to be magnetized. The susceptibility of the particle will dictate the size of moments detected. In addition it is possible that introducing an external magnetic field may enhance the delectability of these particles. For example, the magnetic fields generated by a magnetic dipole such as those used for head localization could be used to introduce a field small enough not to unlock the sensors but perhaps large enough to affect the particles.

5.2.6 Conclusions

MEG can detect a colloidal suspension of magnetic nanoparticles particularly in the frequency spectrum. The spectrum approaches white when the concentration is lowered. The MEG topological maps clearly indicate a spatial correlation between sample location and sensor response. These results support the possibility of utilizing MEG to develop a tool to image magnetic nanoparticles within living organisms.

5.3 Localization of magnetic nanoparticles using magnetoencephalography

[3]

5.3.1 Abstract

Ferrofluids are colloidal suspensions of magnetic nanoparticles in a liquid carrier. In our previous work, magnetoencephalography (MEG) was shown to detect these particles in a liquid suspension at fixed locations by focusing on the magnetic noise generated from random movements of the particles ([7], [8]). In this current study, we demonstrate that particles in a small glass vial situated within an MEG helmet can be spatially localized using a vector beamformer. In addition, by applying a driving frequency using an oscillating magnetic field within the dynamic range of the MEG sensors, the particles can also be seen to oscillate, thus potentially enhancing their signals above the level of brain noise. There is potential to utilize these enhanced signals for better spatial and temporal detection.

5.3.2 Introduction

Ferrofluids are single domain magnetite particles of nanometer dimensions. They are made of an inorganic core of Fe_3O_4 surrounded by a coating of bioactive molecules that can be combined with biological tissue. The particles are also coated with a dispersing agent

[3] A version of this section is being prepared for publication. Cheung, T, Kavanagh, K. L. Localization of Magnetic Nanoparticles using Magnetoecephalography.

that keeps the particles from agglomeration. Our previous work has shown that liquid suspensions of these particles in a vial can be observed in the frequency domain above the frequency profile of the empty room noise ([7], [8]). On a topological map of the frequency, these particles can be observed spatially. The detection of these particles in a dried state have been demonstrated by Jia ([41], [40]) and in living tissue after being exposed to a large magnetic field by Romanus ([68]).

There have also been a some attempts to localize these particles using MEG ([41]). Dipole fits have been used to model and locate these particles after exposure to magnetic field. With the techniques we have developed a different method will be needed to perform particle localization. Since the particles do not show any appreciable change in the time domain, we need a method that is sensitive to frequency domain activity. We turn therefore to beamformers for our localization method. Beamformers are scanning techniques used in MEG to describe neuronal activity. Beamformers are spatial filters that build weights for the measured data that suppresses activity outside the location of interest. Beamformers are often performed within specific bandwidths as they are sensitive to both induced and evoked signals. Since the signal from our nanoparticles rises above the background room noise, the frequency band of highest activity compared to the background room noise can be fed through a beamformer to generate a three dimensional image of the nanoparticle activity. Our current study demonstrates this method using a vector beamformer from the software package called BESA (Brain Electrical Source Analysis).

We have demonstrated that the particles could be detected in the frequency domain, but their overall signal amplitudes, even at full concentration did not rise above background brain noise levels. Magnetization would enhance the particle magnetic fields but previous techniques have required the use of very large magnetic field swell above the threshold for MEG detection and in principle could even damage the MEG device and magnetic shielded room in which it is housed. Magnetic fields within the range of MEG detectability have not been attempted before and it is along these lines that we continued our study of these particles. The MEG measures magnetic field activity in the range of fT to nT. In the upper range are artificially generated sources such as the magnetic dipoles that are used to locate the head during a standard scan. These coils are driven by oscillating currents with specific frequencies and the coil signals are determined through magnetic dipole localization. These coils are sometimes collected only at the beginning and end of the collection but they

are also sometimes collected throughout the data collection period. The frequencies are selected to be above the bandwidth of brain activity and are low pass and notched filtered out of the data during preprocessing. The magnetic fields generated by one of these oscillating coils could help enhance the signal of our nanoparticles to above brain noise.

5.3.3 Methods

Sample Preparation

A sample of ferrofluid manufactured by Ferrofluidics Corporation (Burlington, Massachusetts) was used for our data collections. The sample was a water based colloidal suspension of Fe_3O_4. Core size ranged between 10 and 50 nm and the sample was diluted to a concentration of 0.065 g/ml. A 0.4 ml volume of the ferrofluid was placed in a nonmagnetic cylindrical glass vial with a 12 mm diameter base. The liquid reached a height of 35 mm in the cylinder. The empty container was checked for magnetic contamination before usage.

MEG Measurements

The measurements were carried out using a 151-channel axial gradiometer CTF MEG device located at the Down Syndrome Research Foundation, Burnaby Canada. This MEG is housed in a 4-layer magnetically shielded room. The data was collected at 600 and 1200 samples per second with trial lengths of 10 seconds. Between 10 and 50 trials were collected. Synthetic 3rd order gradient correction was employed to reduce environmental noise. The sample was placed on a nonmagnetic phantom stand affixed with three coordinate positioning coils. These magnetic coils were only energized at the end of collection to avoid potential magnetization of the sample. Polhemus was used to digitize the sample's location relative to these coordinate position coils thus forming a rigid coordinate system for analysis and localization. The cylinder base was digitized on the outside. The sample height was not accounted for. The Polhemus digitization errors ranges from between and 1 and 3 mm. The stand was placed within the helmet region as illustrated in Figure 5.6 and data was collected with the sample alone and with the sample while one of the head localization coils was simultaneously generating magnetic fields. The coil closest the sample was energized. The coil field strength did not exceed the dynamic range of the nearest sensor.

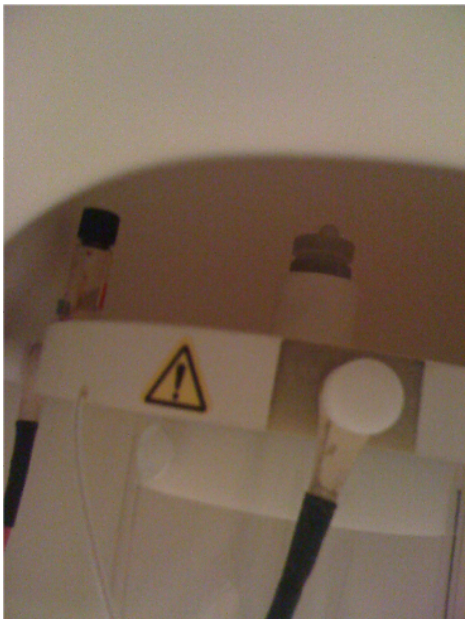

Figure 5.6: Ferrofluid on phantom stand in MEG. The sample is in the glass vial at the left of the photo.

Data Analysis

A vector beamformer from the software BESA was used to localize the ferrofluid. BESA's vector beamformer was used because the radial component of the magnetic field is not invisible for magnetic dipoles. The sensor noise data without the ferrofluid was used for the 'compare condition'. A bandwidth of 5 - 20 Hz was selected for the analysis because based on previous results, the ferrorfluid frequency profile was greatest in this bandwidth. To determine the location of the cylinder base in the corresponding polhemus data, coorrdinates were plotted and the centre of the cylinder base computed by fitting the data to a circle. For the data where the ferrofluid was under the influence of a driving magnetic field, the data was plotted in the time and frequency domains.

5.3.4 Results

The vector beamformer showed a volume of activation with a spread of 7.4 mm in the x direction, 19.9 in the y direction and 21.3 in z direction. It is interesting to note that

the x and y spread is elongated in the y direction and does not fully reproduce the shape of the circular 12 mm cylinder diameter. The 21.3 mm spread in z of the height does not fully reproduce the height of 35 mm cylinder volume. The beamformed peak was located at (67.8, 2.1, 26.4) mm, shown by the intersection of the vertical and horizontal lines in Figure 5.7. The polhemus located the centre of the cylinder at coordinates (69.3, -0.3, 9.7) mm as shown by the diamond shaped marker on the same figure. Since the polhemus located only the base and did not account for height, assuming a height of 35 mm for the sample, the centre of the cylinder from the polhemus coordinates is (69.3, -0.3, 27.2) mm. Hence, the beamformed peak location agreed within 3 mm of the polhemus results in the x-y plane and if we take the height of the liquid volume into account, the beamformed results agree to within 1 mm of the digitized results. These errors fall within the expected error of the Polhemus digitization accuracy.

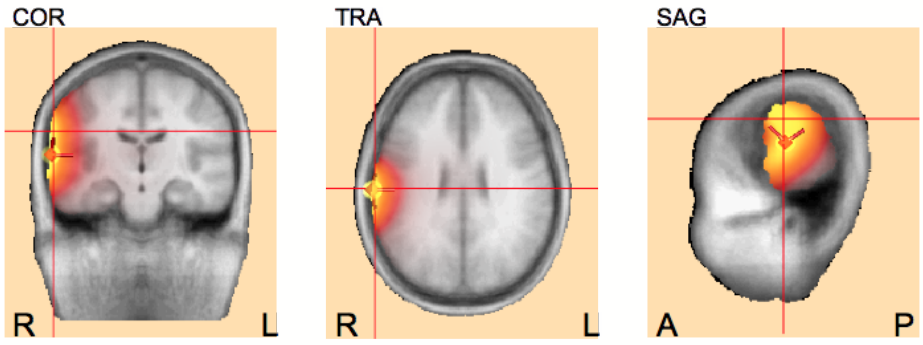

Figure 5.7: Beamformer peak from magnetic nano particle measurements

When driven by an external oscillating magnetic field, the particles were observed to oscillate also at the same frequency. Figure 5.8 shows an overlay of a driving oscillating magnetic field generated by one of the head localization coils with and without the presence of the nanoparticle sample. In the time domain, there is an increase in the amplitude of the signal when the nanoparticles were present. This behaviour can also be seen in the frequency domain. In Figure 5.9, a magnified image of the peak amplitude at the driving frequency is shown. The grey peak, which includes the ferrofluid is 180 ft rms/sqrt(hz) larger than the black peak, which does not include the ferrofluid. Hence, in the frequency domain, the ferrofluid's amplitude rises by 180 ft rms/sqrt(hz) which is well above brain noise.

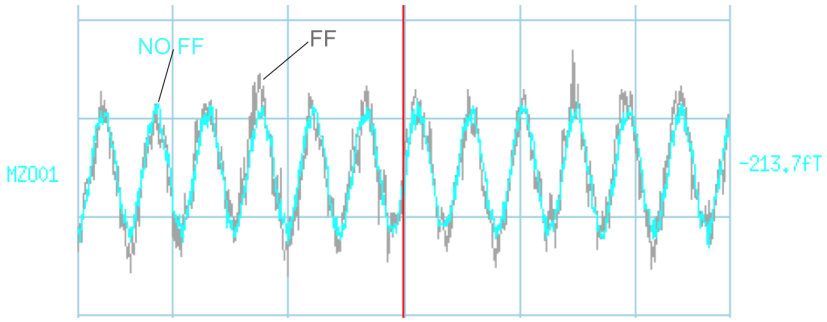

Figure 5.8: An oscillating magnetic field with and without the ferrofluid sample. The blue shows the response at one MEG sensor MZO01 with only the head coil being driven by an oscillating current. The grey shows the head coil in the presence of a ferrofluid sample. The ferrofluid appears to increase the signal amplitude in this channel.

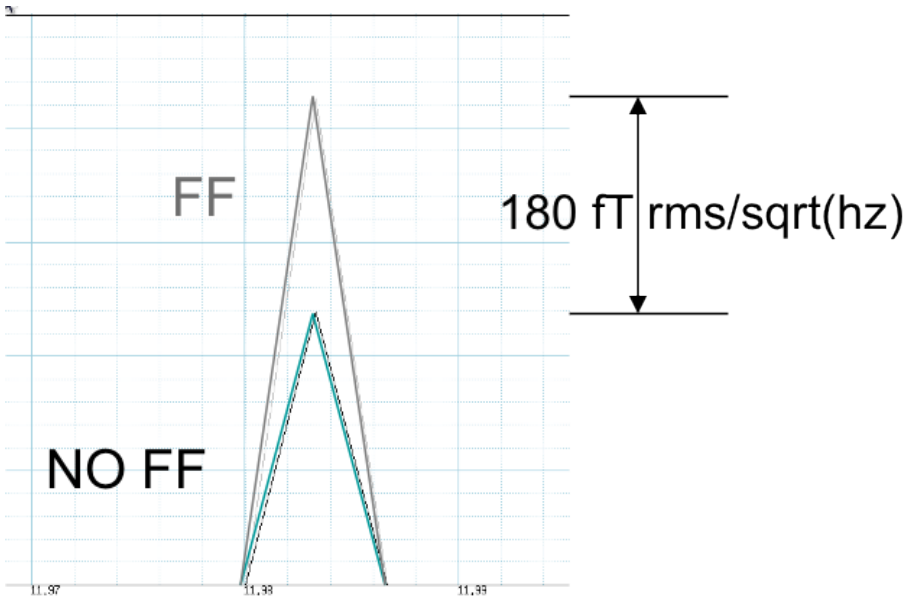

Figure 5.9: Magnified FFT of magnetic particles under a driving magnetic field. Only the peak of the driving frequency is being shown. The peak of the driving frequency is smaller without the ferrofluid present. A difference of 180 fT rms/sqrt(hz) was observed.

5.3.5 Discussion

A novel method was designed to image a vial of magnetic nanoparticles within the MEG helmet. Using the particle's natural movement alone and choosing a frequency band of high activity, the nanoparticles could be localized using a vector beamformer. While the forward model of a point current dipole was not ideal, the results nevertheless agreed well with the Polhemus digitized results. Given that MEG head localization may also have contributed a 1 to 2 mm error, the results of this beamformer method showed promise. It is also possible that the choice of forward model also played a role in the shape of the beamformer spread as well as the peak location. With this in mind, the logical next step was to employ a magnetic dipole model to the problem.

In the second part of the experiment, the question of whether the particles could be observed under the influence of a driving magnetic field was examined. Evidence from other experiments [68] have shown that the particles when bound to a biological marker can be temporarily magnetized after exposure to a large magnetic field. These large fields would not be tolerated near an MEG device nor the MSR that houses the machine and therefore could not be used as a practical basis for magnetization. However, oscillating magnetic fields are being generated already in the MEG during head localization. Magnetic dipole head localization coils are energized either at the beginning and end of the collections or are continuously generating signals throughout a brain measurement. The coil frequencies are removed from the measurement by low pass and notch filtering. Using one of the head localization coils to generate a magnetic field could be a practical means to introduce an oscillating magnetic field to enhance the particle's magnetic signature. The second part of the our experiment aimed to examine the effects of such a field on the ferrofluid sample. The results suggest the particles do indeed oscillate at the driving frequency and can be seen in the time data as deviations from the time data without the particles. In the frequency domain the particles' amplitude variation exceeded the background brain noise threshold. This technique, therefore holds promise to enhance the particle's natural magnetic fields above brain noise for in vivo applications. The challenge in this technique is to find a robust method to separate the fields from the oscillating source and from that of the nanoparticle's response. Since they are separated spatially and the field strength and orientation of the magnetic dipole can be predetermined, a variation of a vector beamformer

technique could be adapted for such an endeavour.

5.3.6 Conclusions

We have demonstrated that a vial of magnetic nanoparticles in an MEG system can be localized using a vector beamformer approach. While the naturally occurring movements of the nanoparticles in the presence of empty room noise can be localized in the MEG, the brain's background activity is above the signal power of the nanoparticles. By using the existing magnetic fields found during routine MEG scanning, the particles signals have been shown to be enhanced above the brain noise threshold. This technique combined with a method to locate these driven particles could offer a tool for MEG imaging using a magnetic contrast agent in living organisms.

5.4 Future Work and Conclusions

This chapter demonstrated new techniques that successfully image nanoparticles in standard commercial MEG devices. The experiments were carried out using a liquid vial of magnetic particles in a colloidal suspension. The novel approach of using the frequency signature of the particles rather than the time signature provided a method to observe the presence of the particles when the time series alone showed little to no changes. By using a bandwidth of high activity, beamforming was used to locate the position of the particles in the MEG. This technique has never been used before to localize magnetic nanoparticles. While these methods were successful in the presence of only empty room noise, the amplitude of the nanoparticles observed in the frequency domain were below the threshold of brain noise. To address this issue, another new technique was developed that utilized the already present oscillating magnetic fields from the head localization coils. The final data collected demonstrated that this driving coil does enhance the magnetic particle's fields to above brain noise and offers a potential solution to the signal to noise issue plaguing the earlier parts of the study. We continue to develop software to localize these particles with a magnetic dipole forward equation and to develop a viable technique to separate the signal of the particles from that of the driving coil. Once these methods are completed testing with tissue samples and then with animals could potentially be the next steps. It is also possible

that Saligram's rat MCG data could be re-analyzed using these new techniques [69].

Chapter 6

Conclusions

This thesis examined three themes that add to the development and applications of MEG. Construction of phantoms provided a framework to explore how to generate and model magnetic fields. Using this knowledge, a single dipole phantom was developed as a tool for comparing MEG devices from different laboratories and different manufacturers. This device ground truth has and will add important knowledge on the differences between MEG data collected from different laboratories. A multiple dipole phantom was used to demonstrate the utility of a hardware ground truth for source modelling verification.

In the second theme, source modelling strategies were developed to examine the neural generators of the face selective M170 neural response. Studies that examine the localization of the M170 have yielded inconclusive results. Through the analysis of a series of data collected from different studies, the M170 was examined in source and sensor space in both children and adults. Localization of the sources of the M170 response revealed the same network of core facial areas as observed in fMRI, namely the FFA, OFA and STS. These locations were all observed to be face selective though individual differences between subjects were also observed. This study supported the hypothesis that the M170 originates from multiple co-activated sources. This work may be the first to show this integrated network of the core facial areas in an MEG source space analysis.

In the final theme of this thesis, the future of MEG imaging was imagined. The idea of using magnetic particles for MEG imaging was introduced through a series of studies, which developed a framework for the characterization, and localization of magnetic nanoparticles. Using frequency rather then time data, the magnetic nanoparticles was

shown to be detectable and by using beamformer techniques a small container of nanoparticles could be localized from while being scanned in an MEG. In addition, adding a small oscillating magnetic field, within the limits of MEG detectability, the nanoparticles could be detected above brain noise. These studies set the stage for potential future applications for magnetic nano particles imaging in living tissue.

Bibliography

[1] BAILLET, S., MOSHER, J. C., AND LEAHY, R. M. Electromagnetic Brain Mapping. *IEEE Signal Processing Magazine 18*, 6, 14–30.

[2] BAILLET, S., RIERA, J. J., MARIN, G., MANGIN, J. F., AUBERT, J., AND GARNERO, L. Evaluation of inverse methods and head models for EEG source localization using a human skull phantom. *Physics in medicine and biology 46*, 1 (Jan. 2001), 77–96.

[3] BARTH, D. S., SUTHERLING, W., BROFFMAN, J., AND BEATTY, J. Magnetic localization of a dipolar current source implanted in a sphere and a human cranium. *Electroencephalography and clinical neurophysiology 63*, 3 (Mar. 1986), 260–73.

[4] BATTY, M., AND TAYLOR, M. J. The development of emotional face processing during childhood. *Developmental science 9*, 2 (Mar. 2006), 207–20.

[5] BUDKER, D., AND ROMALIS, M. Optical magnetometry. *Nature 3* (2007), 227–234.

[6] CARON, A. J., CARON, R. F., AND MACLEAN, D. J. Infant discrimination of naturalistic emotional expressions: the role of face and voice. *Child Development 59*, 3 (1988), 604–616.

[7] CHEUNG, T., KAVANAGH, K., MOISEEV, A., AND MAJUMDER, S. Detection of Magnetic Nanoparticles using Sensor Noise for Magnetoencephalography. In *Human Brain Mapping 2009 Proceedings* (2009).

[8] CHEUNG, T., KAVANAGH, K. L., AND RIBARY, U. A new technique for magnetic nanoparticle imaging for magnetoencephalography using frequency data. In *17th International Conference on Biomagnetism Advances in Biomagnetism* (2010).

[9] CHEUNG, T., AND VIRJI-BABUL, N. MEG correlates of static and dynamic facial expressions in typically developing children. In *Society for Neuroscience Conference San Diego* (2007).

[10] CHEUNG, T., AND VIRJI-BABUL, N. Magnetoencephalographic analysis of emotional face processing in Magnetoencephalographic analysis of emotional face processing in children with Down syndrome : A Pilot Study. *Down Syndrome Quarterly 10*, 2 (2008), 18–21.

[11] CHEUNG, T., WONG, J., PARAMESWARAN, A., BABUL, A., MF, B., KL, K., JIRASEK, A., RIBARY, U., BURNABY, V. A., SYNDROME, D., AND BURNABY, V. B. A Scanner Independent Approach to Modeling Neural Activity with a Hardware Phantom. In *Biomagnetism - Transdisiplinary Research and Exploration* (2008), pp. 5–7.

[12] CHEYNE, D., BOSTAN, A. C., GAETZ, W., AND PANG, E. W. Event-related beamforming: a robust method for presurgical functional mapping using MEG. *Clinical neurophysiology : official journal of the International Federation of Clinical Neurophysiology 118*, 8 (Aug. 2007), 1691–704.

[13] CHOPP, M., CHEN, Q., MORAN, J., AND TEPLEY, N. Biomagnetic Measurments Utilizing Ferrofluids. In *Proceedings of the 8th International Conference on Biomagnetism*.

[14] COHEN, D. Magnetoencephalography: Evidence of magnetic fields produced by alpha-rhythm currents. *Science, 161*, 3843 (1968), 784–786.

[15] COHEN, D. Magnetoencephalography: Detection of the brain's electrical activity with a superconducting magnetometer. *Science 175*, 4022 (1972), 664–666.

[16] COHEN, D., CUFFIN, B. N., YUNOKUCHI, K., MANIEWSKI, R., PURCELL, C., COSGROVE, G. R., IVES, J., KENNEDY, J. G., AND SCHOMER, D. L. MEG versus EEG localization test using implanted sources in the human brain. *Annals of neurology 28*, 6 (Dec. 1990), 811–7.

[17] DAHAN, M., LÉVI, S., LUCCARDINI, C., ROSTAING, P., RIVEAU, B., AND TRILLER, A. Diffusion dynamics of glycine receptors revealed by single-quantum dot tracking. *Science (New York, N.Y.) 302*, 5644 (Oct. 2003), 442–5.

[18] DASSIOS, G., AND HADJILOIZI, D. On the non-uniqueness of the inverse problem associated with electroencephalography. *Inverse Problems 25*, 11 (Nov. 2009), 115012.

[19] DASSIOS, G., AND KARIOTOU, F. Magnetoencephalography in ellipsoidal geometry. *Journal of Mathematical Physics 44*, 220-241 (2003).

[20] DEFFKE, I., SANDER, T., HEIDENREICH, J., SOMMER, W., CURIO, G., TRAHMS, L., AND LUESCHOW, A. MEG/EEG sources of the 170-ms response to faces are co-localized in the fusiform gyrus. *NeuroImage 35*, 4 (May 2007), 1495–501.

[21] ELEKTA. Source Modelling Software User's Guide. Tech. Rep. October, 2008.

[22] ELEKTA. MaxFilter User Guide.

[23] FIFE, A. A., VRBA, J., ROBINSON, S. E., ANDERSON, G., BETTS, K., BURBANK, M. B., CHEYNE, D., CHEUNG, T., GOVORKOV, S., HAID, G., HUNTER, C., KUBIK, P. R., LEE, S., MCKAY, J., REICHL, E., SCHROYEN, C., SEKACHEV, I., SPEAR, P., TAYLOR, B., TILLOTSON, M., AND SUTHERLING, W. Synthetic Gradiometer Systems for MEG. *IEEE Transactions on Appiled Superconductivity 9*, 2 (1999), 4063–4068.

[24] FOKAS, A. S., KURYLEV, Y., AND MARINAKIS, V. The unique determination of neuronal currents in the brain via magnetoencephalography. *Inverse Problems 20*, 4 (Aug. 2004), 1067–1082.

[25] GAUTHIER, I., TARR, M. J., MOYLAN, J., SKUDLARSKI, P., GORE, J. C., AND ANDERSON, A. W. The fusiform "face area" is part of a network that processes faces at the individual level. *Journal of cognitive neuroscience 12*, 3 (May 2000), 495–504.

[26] GESELOWITZ, D. B. On bioelectric potentials in an inhomogeneous volume conductor. *Biophysical Journal 7*, 1 (Jan. 1967), 1–11.

[27] GRAMFORT, A. Mapping, timing and tracking cortical activations with MEG and EEG : Methods and application to human vision. *Methods*.

[28] GRYNSZPAN, F., AND GESELOWITZ, D. B. Model studies of the magnetocardiogram. *Biophysical journal 13*, 9 (Sept. 1973), 911–25.

[29] HALGREN, E., RAIJ, T., MARINKOVIC, K., JOUSMÄKI, V., AND HARI, R. Cognitive response profile of the human fusiform face area as determined by MEG. *Cerebral cortex (New York, N.Y. : 1991) 10*, 1 (Jan. 2000), 69–81.

[30] HALIT, H., DE HAAN, M., AND JOHNSON, M. H. Cortical specialisation for face processing: face-sensitive event-related potential components in 3- and 12-month-old infants. *NeuroImage 19*, 3 (2003), 1180–1193.

[31] HÄMÄLÄINEN, M., HARI, R., ILMONIEMI, R., KNUUTILA, J., AND LOUNASMAA, O. Magnetoencephalography-theory, instrumentation, and applications to noninvasive studies of the working human brain. *Reviews of modern Physics 65*, 2 (1993), 413–497.

[32] HARRIS, A. M., DUCHAINE, B. C., AND NAKAYAMA, K. Normal and abnormal face selectivity of the M170 response in developmental prosopagnosics. *Neuropsychologia 43*, 14 (Jan. 2005), 2125–36.

[33] HAXBY, J., HOFFMAN, E., AND GOBBINI, M. The distributed human neural system for face perception. *Trends in cognitive sciences 4*, 6 (June 2000), 223–233.

[34] HAXBY, J. V., HOFFMAN, E. A., AND GOBBINI, M. I. Human neural systems for face recognition and social communication. *Biological psychiatry 51*, 1 (Jan. 2002), 59–67.

[35] HELMHOLTZ, H. Ueber einige Gesetze der Vertheilung elektrischer Ströme in körperlichen Leitern mit Anwendung auf die thierisch-elektrischen Versuche. *Ann. Phys. Chem. 89* (1853), 211–233, 353–377.

[36] HENDERSON, R. M., MCCULLOCH, D. L., AND HERBERT, A. M. Event-related potentials (ERPs) to schematic faces in adults and children. *International Journal of Psychophysiology 51*, 1 (Dec. 2003), 59–67.

[37] HOVORKA, R., VIRJI-BABUL, N., KERNS, K., AND TANAKA, J. Development and Validation of the H-DEED: Hovorka Dynamic Emotional Expression Database. *NowCAM* (2006).

[38] ILMONIEMI, R. J., HAMALAINEN, M. S., AND KNUUTILA, J. The Forward and Inverse Problems. In *Biomagnetism: Applications and Theory* (1985), W. H, S. G, and K. T, Eds., pp. 278–282.

[39] ITIER, R. J., AND TAYLOR, M. J. Source analysis of the N170 to faces and objects. *Analysis 15*, 8 (2004), 1–5.

[40] JIA, W., XU, G., SCLABASSI, R. J., ZHU, J.-G., BAGIC, A., AND SUN, M. Detection of magnetic nanoparticles with magnetoencephalography. *Journal of Magnetism and Magnetic Materials 320*, 8 (Apr. 2008), 1472–1478.

[41] JIA, W., XUYUAN, Z., XU, G., SCLABASSI, R., A, B., AND SUN, M. Nanoparticle-Enhanced MEG Detection for in vivo Imaging. In *Biomagnetism - Transdisiplinary Research and Exploration* (2008), pp. 89–91.

[42] KANWISHER, N., MCDERMOTT, J., AND CHUN, M. M. The fusiform face area: a module in human extrastriate cortex specialized for face perception. *The Journal of neuroscience : the official journal of the Society for Neuroscience 17*, 11 (June 1997), 4302–11.

[43] KASARI, C., FREEMAN, S. F., AND HUGHES, M. A. Emotion recognition by children with Down syndrome. *American journal of mental retardation : AJMR 106*, 1 (Jan. 2001), 59–72.

[44] KISHIMOTO, Y., LIU, J., CHEUNG, T., PARAMESWARAN, A. M., AND AMAYA, K. Magnetic dipole localization studies for magnetoencephalography using multiple phase inverse analysis and the experimental verification. In *Canadian Medical and Biological Engineering Conference* (2009).

[45] KOMINIS, I. K., KORNACK, T. W., ALLRED, J. C., AND ROMALIS, M. V. A subfemtotesla multichannel atomic magnetometer. *Nature 422*, April (2003), 596–599.

[46] KYLLIAINEN, A., BRAEUTIGAM, S., HIETANEN, J. K., SWITHENBY, S. J., AND BAILEY, A. J. Face and gaze processing in normally developing children: a magnetoencephalographic study. *The European journal of neuroscience 23*, 3 (Feb. 2006), 801–10.

[47] LEAHY, R. M., MOSHER, J. C., SPENCER, M. E., HUANG, M. X., AND LEWINE, J. D. A study of dipole localization accuracy for MEG and EEG using a human skull phantom. *Electroencephalography and clinical neurophysiology 107*, 2 (Aug. 1998), 159–73.

[48] LINKENKAER-HANSEN, K., PALVA, J. M., SAMS, M., HIETANEN, J. K., ARONEN, H. J., AND ILMONIEMI, R. J. Face-selective processing in human extrastriate cortex around 120 ms after stimulus onset revealed by magneto- and electroencephalography. *Neuroscience letters 253*, 3 (Sept. 1998), 147–50.

[49] LIU, F.-Y. *DESIGN AND CONSTRUCTION OF A BRAIN MAGNETIC SIGNAL GENERATION PHANTOM FOR SOURCE RECONSTRUCTION STUDY*. PhD thesis, Simon Fraser University, 2011.

[50] LIU, J., KISHIMOTO, Y., CHEUNG, T., PARAMESWARAN, A. M., AND AMAYA, K. Development of human brainwave simulating device for magnetoencephalography and the corresponding dipole localization study. In *17th International Conference on Biomagnetism Advances in Biomagnetism* (2010).

[51] LLINAS, R., AND NICHOLSON, C. Analysis of field potential in the central nervous system. *Handbook Electroenceph Clin Neurophysio 2B* (1974), 6–83.

[52] LLINÁS, R. R. The intrinsic electrophysiological properties of mammalian neurons: insights into central nervous system function. *Science (New York, N.Y.) 242*, 4886 (Dec. 1988), 1654–64.

[53] MARSHALL, S. Vehicle detection using a magnetic field sensor. *Vehicular Technology, IEEE Transactions on V*, 2 (1978), 65–68.

[54] MCVEIGH, P., BOSTAN, A., AND CHEYNE, D. Study of conducting volume boundary influence on source localization using a realistic MEG phantom. *International Congress Series 1300* (June 2007), 153–156.

[55] MEIJS, J. W. H., AND PETERS, M. The EEG and MEG using a model of eccentric spheres to describe the head. *IEEE Transactions on Biomedical Engineering 34*, 913-920 (1987).

[56] MOISEEV, A., GASPAR, J. M., SCHNEIDER, J. A., AND HERDMAN, A. T. Application of multi-source minimum variance beamformers for reconstruction of correlated neural activity. *NeuroImage 58*, 2 (Sept. 2011), 481–96.

[57] MOSHER, J., LEWIS, P., AND LEAHY, R. Multiple dipole modeling and localization from spatio-temporal meg data. *IEEE Transactions on Biomedical Engineering 39*, 6 (1992), 541–553.

[58] MURAKAMI, S., ZHANG, T., HIROSE, A., AND OKADA, Y. C. Physiological origins of evoked magnetic fields and extracellular field potentials produced by guinea-pig CA3 hippocampal slices. *The Journal of Physiology 544*, 1 (Aug. 2002), 237–251.

[59] NELDER, J. A., AND MEAD, R. A simplex method for function minimization. *Comput. J. 7* (1965), 308–313.

[60] NEWBOWER, AND RONALD, S. Magnetic Fluids in the Blood. *IEEE Transactions on Magnetics MAG-9*, 3 (1973), 447–450.

[61] NOLTE, G. The magnetic lead field theorem in the quasi-static approximation and its use for magnetoencephalography forward calculation in realistic volume conductors. *Physics in medicine and biology 48*, 22 (Nov. 2003), 3637–52.

[62] OKADA, Y. C. Neurogenesis of evoked magnetic fields. In *Biomagnetism an Interdisciplinary Approach* (1982), S. J. Wiiliamson, G. L. Romani, L. Kaufman, and L. Modena, Eds., Plenum Press, New York and London, pp. 399–408.

[63] ORUC, I., CHEUNG, T., DALRYMPLE, K., FOX, C., IARIA, G., HANDY, T., AND BARTON, J. Residual face-selectivity of the N170 and M170 is related to the status

of the occipital and fusiform face areas in acquired prosopagnosia. *Journal of Vision 10*, 7 (Aug. 2010), 585–585.

[64] PATHAK, S., CAO, E., DAVIDSON, M. C., JIN, S., AND SILVA, G. A. Quantum dot applications to neuroscience: new tools for probing neurons and glia. *The Journal of neuroscience : the official journal of the Society for Neuroscience 26*, 7 (Feb. 2006), 1893–5.

[65] PLONSEY, R., AND HEPPNER, D. B. Considerations of quasi-stationarity in electrophysiological systems. *Bulletin of Mathematical Biology 29*, 4 (1944), 657–664.

[66] ROBINSON, S. E. Localization of event-related activity by SAM(erf). *Neurology & clinical neurophysiology : NCN 2004* (Jan. 2004), 109.

[67] ROBINSON, S. E., AND VRBA, J. SAM Tutorial. Tech. Rep. December, 2004.

[68] ROMANUS, E. Magnetic nanoparticle relaxation measurement as a novel tool for in vivo diagnostics. *Journal of Magnetism and Magnetic Materials 252* (Nov. 2002), 387–389.

[69] SALIGRAM, U., MORAN, J. E., AND TEPLEY, N. MCG Studies in Rats Using Ferrofluids. In *Biomag 96: proceedings of the Tenth International Conference on Biomagnetism* (1996), C. Aine, Y. Okada, G. Stroink, S. Swithenby, and C. C. Wood, Eds., pp. 675–678.

[70] SARVAS, J. Basic mathematical and electromagnetic concepts of the biomagnetic inverse problem. *Physics in medicine and biology 32*, 1 (Jan. 1987), 11–22.

[71] SATO, W., KOCHIYAMA, T., YOSHIKAWA, S., NAITO, E., AND MATSUMURA, M. Enhanced neural activity in response to dynamic facial expressions of emotion: an fMRI study. *Brain research. Cognitive brain research 20*, 1 (June 2004), 81–91.

[72] SCHERER, C., AND FIGUEIREDO NETO, A. M. Ferrofluids: properties and applications. *Brazilian Journal of Physics 35*, 3a (Sept. 2005), 718–727.

[73] SELTZER, S. J., AND ROMALIS, M. V. Unshielded three-axis vector operation of a spin-exchange-relaxation-free atomic magnetometer. *Applied Physics Letters 85*, 20 (2004), 4804–4806.

[74] SERRANO, J. M., IGLESIAS, J., AND LOECHES, A. Visual discrimination and recognition of facial expressions of anger, fear, and surprise in 4- to 6-month-old infants. *Developmental psychobiology 25*, 6 (Sept. 1992), 411–25.

[75] SPENCER, M. E., LEAHY, R. M., AND MOSHER, J. C. A Skull-Based Multiple Dipole Phantom. In *Proceedings of the 10th International Conference on Biomagnetism, Santa Fe, New Mexico* (1996), A. CJ, O. J, S. G, S. SJ, and W. CC, Eds.

[76] STOK, C. J., AND MEIJST, J. W. H. Inverse solutions based on MEG and EEG applied to volume conductor analysis. *Phys. Med. Biol. 32*, 1 (1987), 99–104.

[77] TAUE, S., ICHIHARA, S., SUGIHARA, Y., ISHIKAWA, K., SUGIOKA, H., MIZUTANI, N., LIU, S., HIRAI, Y., TABATA, O., AND KOBAYASHI, T. Measurement of Biomagnetic Fields in Small Animals by use of an Optical Pumping Atomic Magnetometer. *Biomagnetism - Transdisiplinary Research and Exploration* (2008), 3–5.

[78] TAYLOR, M. J., EDMONDS, G. E., MCCARTHY, G., AND ALLISON, T. Eyes first! Eye processing develops before face processing in children. *Neuroreport 12*, 8 (June 2001), 1671–6.

[79] TAYLOR, M. J., MCCARTHY, G., SALIBA, E., AND DEGIOVANNI, E. ERP evidence of developmental changes in processing of faces. *Clinical neurophysiology : official journal of the International Federation of Clinical Neurophysiology 110*, 5 (May 1999), 910–5.

[80] UEHARA, G., HIGUCHI, M., ADACHI, Y., KAWAI, J., TANAKA, H., HARUTA, Y., MIYAMOTO, M., SHIMOZU, T., AND KAWABATA, M. An error in magnetic field of isosceles-triangle coil as a representation of equivalent current dipole. *International Congress Series 1300* (June 2007), 607–610.

[81] VAN VEEN, B. D., VAN DRONGELEN, W., YUCHTMAN, M., AND SUZUKI, A. Localization of brain electrical activity via linearly constrained minimum variance

spatial filtering. *IEEE transactions on bio-medical engineering 44*, 9 (Sept. 1997), 867–80.

[82] VIRJI-BABUL, N., KERNS, K., ZHOU, E., KAPUR, A., AND SHIFFRAR, M. Perceptual-motor deficits in children with Down syndrome: implications for intervention. *Down's syndrome, research and practice : the journal of the Sarah Duffen Centre / University of Portsmouth 10*, 2 (July 2006), 74–82.

[83] VRBA, J. PowerPoint Image, 1997.

[84] VRBA, J. Magnetoencephalography: the art of finding a needle in a haystack. *Physica C: Superconductivity 368*, 1-4 (Mar. 2002), 1–9.

[85] VRBA, J., ANDERSON, G., BETTS, K., BURBANK, M., CHEUNG, T., CHEYNE, D., AND AL., E. 151-Channel whole-cortex MEG system for seated or supine positions. In *Recent Advances in Biomagnetism* (1999), T. Yoshimoto and E. Al., Eds., pp. 93–96.

[86] VRBA, J., ANGUS, V., BELTS, K., BURBANK, M., CHEUNG, T., AND FIFE, A. 143 Channel Whole-Cortex MEG System. In *Biomag96: Advances in Biomagnetism Research*, C. A. et Al, Ed. Springer-Verlag, 2000.

[87] VRBA, J., BETTS, K., BURBANK, M., CHEUNG, T., A.A. FIFE, HAID, G., KUBIK, P., LEE, S., MCCUBBIN, J., MCKAY, J., MCKENZIE, D., SPEAR, P., TAYLOR, B., TILLOTSON, M., CHEYNE, D., AND WEINBERG, H. Whole cortex, 64 channel SQUID biomagnetometer system. *IEEE Transactions on Appiled Superconductivity 3*, 1 (Mar. 1993), 1878–1882.

[88] VRBA, J., CHEUNG, T., CHEYNE, D., AND ROBINSON, S. Errors in ECD localization with partial sensor coverage. In *Proceedings from Biomag98, The 11th International Conference on Biomagnetism, Sendai, Japan* (1998), pp. 1–4.

[89] VRBA, J., AND ROBINSON, S. Linearly constrained minimum variance beamformers, synthetic aperture magnetometry, and MUSIC in MEG applications. *Conference Record of the Thirty-Fourth Asilomar Conference on Signals, Systems and Computers (Cat. No.00CH37154) 1*, 313–317.

[90] VRBA, J., AND ROBINSON, S. Signal processing in magnetoencephalography. *Methods 25*, 2 (2001), 249–271.

[91] VRBA, J., TAYLOR, B., CHEUNG, T., A.A. FIFE, HAID, G., KUBIK, P., LEE, S., MCCUBBIN, J., AND BURBANK, M. Noise cancellation by a whole-cortex SQUID MEG system. *IEEE Transactions on Appiled Superconductivity 5*, 2 (June 1995), 2118–2123.

[92] WIKIPEDIA. http://en.wikipedia.org/wiki/Orders_of_magnitude_(magnetic_field).

[93] WILSON, H. S. Continuous head-localization and data correction in a whole-cortex MEG sensor. *Neurology & clinical neurophysiology : NCN 2004* (Jan. 2004), 56.

[94] WISHART, J. G. Children with Down's syndrome. In *Special Teaching for Special Childre: Padagogies for Inclusion*, A. Lewis and B. Norwich, Eds. Open University Press, Maidenhead, UK, 2005, pp. 81–95.

[95] WISHART, J. G., AND PITCAIRN, T. K. Recognition of identity and expression in faces by children with Down syndrome. *American journal of mental retardation : AJMR 105*, 6 (Nov. 2000), 466–79.

[96] XU, Y., LIU, J., AND KANWISHER, N. The M170 is selective for faces, not for expertise. *Neuropsychologia 43*, 4 (Jan. 2005), 588–97.